

---

# Current and Noise in Driven Heterostructures

---

## Dissertation

zur Erlangung des akademischen Grades eines  
Doktors der Naturwissenschaften,  
der Mathematisch-Naturwissenschaftlichen Fakultät  
der Universität Augsburg vorgelegt



von

**Franz Kaiser**

Lehrstuhl für Theoretische Physik I  
Universität Augsburg

Augsburg, im Januar 2009

Betreuer:

Priv.-Doz. Dr. Sigmund Kohler  
Lehrstuhl für Theoretische Physik I  
Universität Augsburg

Prof. Dr. Alexander Holleitner  
Walter-Schottky-Institut  
Technische Universität München

Erstgutachter: Priv.-Doz. Dr. Sigmund Kohler  
Zweitgutachter: Prof. Dr. Ulrich Eckern

Tag der mündlichen Prüfung: 18. Februar 2009

*Für meine Mutter*



# Contents

<b>1</b>	<b>Introduction</b>	<b>1</b>
<b>2</b>	<b>The model Hamiltonian</b>	<b>5</b>
<b>3</b>	<b>Charge, current and noise</b>	<b>9</b>
3.1	Current-current correlator . . . . .	9
3.2	Full Counting Statistics . . . . .	11
<b>4</b>	<b>Master equation approach for current and noise</b>	<b>15</b>
4.1	Perturbation theory and reduced density operator . . . . .	15
4.2	Computation of moments and cumulants . . . . .	17
4.3	Explicit form of current and noise . . . . .	19
<b>5</b>	<b>Pump current and noise in non-adiabatically driven nanosystems</b>	<b>23</b>
<b>6</b>	<b>Electron transport in junctions with energy disorder</b>	<b>29</b>
6.1	Electron transport with slowly fluctuating energies . . . . .	30
6.2	AC-driven disordered junctions . . . . .	31
<b>7</b>	<b>Pump currents induced by propagating waves</b>	<b>35</b>
7.1	Degenerate two-level system . . . . .	37
7.2	Current reversals in an open transport channel with three sites . . . . .	38
<b>8</b>	<b>Photo induced ballistic electron transport</b>	<b>43</b>
8.1	Modelling . . . . .	44
8.2	Circle-shaped constriction . . . . .	46
8.3	Channel geometry . . . . .	53
<b>9</b>	<b>Summary and outlook</b>	<b>59</b>
<b>A</b>	<b>Floquet theory</b>	<b>61</b>
A.1	Overview of general properties . . . . .	61
A.2	Analytical solution for a two-level system . . . . .	63
A.3	Floquet theory for second quantisation . . . . .	64
<b>B</b>	<b>Extracting model parameters from experimental data</b>	<b>67</b>
B.1	Experimental realisation . . . . .	67
B.2	Comparison with experimental data . . . . .	70

## *Contents*

# 1 Introduction

The history of integrated circuits (IC) started with an idea by Geoffrey Dummer in 1952, and its realisations by Jack Kilby and Robert Noyce in the late fifties. Although the first working IC by Kilby was made of germanium, today's devices are based on the concept of Noyce, who used silicon. Kilby's prototype IC was 20 mm<sup>2</sup> in size, and contained only a few transistors. By contrast, nowadays modern manufacturing techniques enable the fabrication of 1.72 billion transistors on 596 mm<sup>2</sup> (Intel Itanium 2). Intel's founder Gordon Moore predicted this tremendous progress in process technology in his famous publication [1] claiming that every 24 months the number of transistors per area doubles.

The age of Moore's Law notwithstanding, the development follows his forecast until today. This impressive progress, creating a market worth 270 billion dollars in 2008, relies mostly on the improvement of lithographic methods: Today's state-of-the-art semiconductor devices have a gate size of approximately 45 nm, achieved by using ultraviolet radiation of an excimer laser with a wavelength of 193 nm. Further miniaturisation of the gate size to 22 nm might still be possible with standard lithography, but the limitations are already apparent: The wavelength of the light source is much larger than the desired structures.

Extreme ultraviolet radiation (EUV) with a wavelength of 13.5 nm has been chosen to be the next generation light source, but such high energy sources suffer from certain drawbacks. In the soft x-ray regime all materials are completely opaque and the classical setup with a mask between wafer and light source cannot be used anymore. Hence, new mirrors containing the mask must be developed in order to work in reflection and not in transmission anymore. Furthermore these new mirrors must outperform today's devices in stiffness and stability by at least an order of magnitude, for example they must not bend more than several nm under the gravitational force.

This short outlook on the challenges concerning only a single component of the upcoming manufacturing technique gives already an insight into the difficulties industry faces at the moment.

Nevertheless, the established and affordable lithography-based technique remains the method of choice of many experimental groups. Although being invented as a classical technique, that is for creating structures of standard circuitry, it may be used to fabricate a new kind of devices based on quantum effects. Ultra small entrapments for electrons bring out the quantum nature of the electrons by exhibiting a discrete electronic level structure and suitable electric potentials tune reliably the energy level of this so-called quantum dot. Thus, in the last two decades, experiments on single electrons became feasible and have been studied

## 1 Introduction

extensively [2–6], and recent advances demonstrate that these model systems still bear interesting and new effects [7, 8]

While the current is the quantity easiest accessible in a transport experiment, the study of the noise properties in a nano sized object shines more light on the physics at work. The famous saying of Landauer, "The noise is the signal" subsumes this fact concisely. Of course, one must distinguish clearly between the different noise sources present in the experimental setup. External sources, for example unstable power supplies, jamming fields, etc., can deteriorate the results; hence the experimentalists face the challenge to reduce this unwanted environmental noise sources.

In contrast to the unwanted noise named above, there are intrinsic fluctuations in the signal. In the 1920s Schottky was the first to discuss the noise characteristics of vacuum tubes [9]. The discreteness of the charge carriers and the stochastic nature of the emission process lead to fluctuations in the electric current. Beyond classical physics, quantum effects may play a dominant role in mesoscopic conduction. Thus, a deviation from shot noise can be expected. In this way, the noise serves as a valuable and enlightening source of information for the origin of ongoing processes in the conductor.

For future industrial usage of devices based on quantum effects it is not sufficient to understand and control the current properly, but moreover to have a clear signal and a small noise level. A prominent example exhibiting good signal-to-noise ratios [10] is an electron pump, where without any bias voltage a current can be induced by a suitable ac field.

The evaluation of fluctuations mostly built up on direct and tedious computation of the current and noise [11, 12]. A more systematic and elegant way, the so-called Full Counting Statistics (FCS), has been adopted to the description of electron transport. The FCS were developed in the field of quantum optics, where it served as a tool to analyse how the quantum nature of the bosonic photon field manifests itself in the photon detection process [13]. Levitov and Lesovik [14] adopted this method to static fermionic systems, and by now there are numerous publications dealing with many different aspects of the FCS in quantum transport [15–18]. While the usability of master equations in this context was restricted due to lengthy algebra, we develop in this work a systematic approach to numerically compute the noise characteristics of a driven nano system within a master equation based on the ideas of FCS.

A further requirement for a serial production of nanoscale devices is their stability against inevitable production imperfections. These small deviations from the ideal electronic structure might reduce significantly the functionality of the devices. Therefore an analysis of the sample-to-sample fluctuations in a large number of realisations can give an insight into the minimal requirements on the stability of the manufacturing process. Within this thesis we present a numerical study of the impact of these deviations from an ideal setup in both static and driven systems and deduce general recommendations. Our results also apply to recent ensemble measurements of molecules arranged in mono-layers between



conducting leads [19].

Apart from the precise control of single electrons in nano structures, an external energy source can also be used to create bunches of hot electrons in a two dimensional electron gas. In such systems, the spatially separation of the optically created electron hole pairs may have a pronounced effect on the photoresponse leading to a photoconductive gain effect [20, 21], revealing the time scales at which the recombination and the separation take place [22].

In a similar experimental setup with two distinct structures [23], a laser spot supplies sufficient energy to excite charge carriers to the conduction band, and a subsequent current measurement was performed. By scanning the probe, they obtained a position-dependent current map. An interesting question in this context deals with a suitable theoretical description capable of explaining the effects of the geometry in the experimental results.

This thesis is organised as follows. In the second chapter we introduce a tight-binding model for quantum dot systems with very strong Coulomb interaction. Chapter 3 relates the physical observables current and noise with the cumulants of the probability distribution of the electron number in one lead. A master equation formalism for the computation of the reduced density operator is derived in chapter 4. Additionally, we derive a time-dependent generalised master equation for the full counting statistics.

With all necessary tools at hand we compare in chapter 5 the results of a Green's function approach for non-interacting electrons with our master equation results. Furthermore, we prove that the influence of the interaction is rather weak for the particular system of a electron pump. Moreover, we study in chapter 6 how sample-to-sample fluctuations affect transport and the resulting probability distribution of the current for two systems, an open transport channel and a symmetric system that might show pump effects. Time-dependent systems in which the phase lag between neighbouring sites varies are considered in chapter 7. It turns out that an electron-electron interaction in the system, together with the symmetry-breaking propagating wave are sufficient to induce directed pump currents. In chapter 8, we drop the tight-binding description used before to model the influence of geometrical constraints on the electron movement in a two dimensional electron gas. We analyse the current for different scattering probabilities; assuming various depletion lengths in the structure. Comparing our simulation with measurements, we can prove the validity of our simplified model. Appendix A introduces the reader to the Floquet theory and its basic implications. By comparing experimental results of strongly coupled quantum dots with a tight-binding model in appendix B, we are able to determine the precise values of the theoretical parameters.

## *1 Introduction*

## 2 The model Hamiltonian

In order to avoid inconsistencies in the theoretical description with fundamental physical principles, e.g., the Pauli principle for fermions, we will employ a tight-binding Hamiltonian written in the second quantisation.

Furthermore, we are interested in the influence of a periodic driving force onto the system. To include it correctly in our model, we will take advantage of a Floquet approach which additionally eases the numerical treatment.

The standard setup we investigate consists of three separated parts, a central system, its surrounding and an interconnect between them, see fig. 2.1. Physically, the central system consists of an array of quantum dots and is characterised by a discrete energy spectrum. The environment is made up of two independent electron reservoirs (or leads). The leads are in general metallic contacts, which allow both very good electrical contact to the measurement devices and good shielding against (unwanted) effects of the driving. The coupling of the central system to the leads allows an exchange of charge carriers and by this means a current can flow.

Hence, we can write the Hamiltonian of our setup in a very general form as

$$H(t) = H_{\text{wire}}(t) + H_{\text{leads}} + H_{\text{coupling}}, \quad (2.1)$$

where the different terms correspond to the central conductor (“wire”), the electron reservoirs (“leads”), and the wire-lead couplings, respectively. We focus on the regime of coherent quantum transport where the main physics at work occur on the system itself. So we neglect possible effects stemming from the environment, like hot electrons from the leads or dissipation on the wire, which never can be eliminated in a real experiment.

In second quantisation using a tight-binding approximation with  $N$  orbitals  $|n\rangle$ , the wire Hamiltonian reads

$$H_{\text{wire}}(t) = \sum_{n=1}^N E_n(t) c_n^\dagger c_n - \Delta \sum_{n=1}^{N-1} (c_{n+1}^\dagger c_n + c_n^\dagger c_{n+1}) + H_{\text{interaction}}, \quad (2.2)$$

where  $E_n(t)$  denotes the generally time-dependent onsite energies and  $\Delta$  is the tunnel matrix element between neighbouring sites. This also describes a Hückel model for a molecular wire where each site corresponds to one orbital. The fermion operator  $c_n^\dagger$  ( $c_n$ ) creates (annihilates) an electron at site  $n$ . These operators obey the anti-commutation relations  $[c_n^\dagger, c_n]_+ = \delta_{nn'}$  and  $[c_n^\dagger, c_n^\dagger]_+ = [c_n, c_n]_+ = 0$  which implies a mutual orthogonality between them.

## 2 The model Hamiltonian

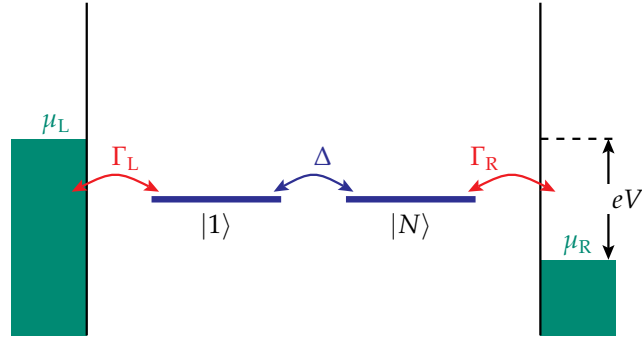


Figure 2.1: Level structure of a double quantum dot with two orbitals. The terminating sites are coupled to leads with chemical potential  $\mu_L$  and  $\mu_R = \mu_L + eV$ , respectively.

The influence of an external driving with frequency  $\Omega = 2\pi/\mathcal{T}$  results in a time dependence solely of the wire Hamiltonian. In general, quantum systems can be driven in several ways, the setup we consider deals with propagating waves passing through the system. Thereby, they induce a modulation of the onsite energies with the periodicity and the amplitude of the wave. In the upcoming numerical studies, we adopt the simplification that the phase shift between all dots stays the same.

Such driven systems can be realised, e.g., if a surface acoustic wave serves as external driving force. The distance between two sites translates into a phase lag of the oscillating onsite energies.

Then, the corresponding time-dependent part of the onsite energies reads

$$E_n(t) = A \cos(\Omega t + x_n \Theta), \quad (2.3)$$

with the scaled position  $x_n = \frac{1}{2}(N + 1 - 2n)$  that shifts the phase between neighbouring sites by  $\Theta$ .

Moreover, there are currently strong attempts to build systems of serially coupled triple quantum dots, where the phase lag between the onsite energies can be modulated individually. A properly controlled phase lag can mimic a propagating wave.

Note that we only consider periodic driving and neglect transient effects, for example the settlement after switching on or off the driving. This simplification will allow us to develop a Floquet theory which is based on the strict time periodicity of the external fields. Even though transients cannot be avoided in real life experiments, a measurement over a long time will suppress these effects and is therefore desirable.

There are various different expressions for the interaction Hamiltonian: we will restrict ourselves to a capacitor-like model, such that

$$H_{\text{interaction}} = \frac{U}{2} \mathcal{N}_{\text{wire}} (\mathcal{N}_{\text{wire}} - 1), \quad (2.4)$$

where  $\mathcal{N}_{\text{wire}} = \sum_n c_n^\dagger c_n$  describes the number of electrons on the wire. Below we shall focus on two limits, namely the interaction-free case  $U = 0$  and strong interaction,  $U \rightarrow \infty$ . Physically, the latter means that the Coulomb repulsion is so strong that only states with zero or one excess electron play a role. This results for the case of  $U = \infty$  in an effective reduction of the dimensionality of the Hilbert space to  $N + 1$  and, thus, in more manageable numerical effort, which we will discuss later in more detail. In the experiment, the regime of strongly-interacting dots can be reached, if the energy splitting of the levels is the dominant energy scale, so that one can restrict the population of the dot to a single extra charge in the energy range under consideration.

The two independent leads, attached to the left and the right of the central system, are modelled by ideal gases of non-interacting electrons,

$$H_{\text{leads}} = \sum_q \epsilon_q (c_{Lq}^\dagger c_{Lq} + c_{Rq}^\dagger c_{Rq}), \quad (2.5)$$

where  $c_{Lq}^\dagger$  ( $c_{Rq}^\dagger$ ) creates an electron in the state  $|Lq\rangle$  ( $|Rq\rangle$ ) in the left (right) lead which is orthogonal to all wire states. As pointed out before, the leads are not affected by the external fields. Again, the fermionic operators fulfil the anti-commutation relations,  $[c_{\ell q}^\dagger, c_{\ell' q'}]_+ = \delta_{\ell\ell'} \delta_{qq'}$  and  $[c_{\ell q}^\dagger, c_{\ell' q'}]_+ = [c_{\ell q}, c_{\ell' q'}]_+ = 0$ , and are mutually orthogonal. We assume the electron bath to be initially at thermal equilibrium at temperature  $T$  and with the electro-chemical potentials  $\mu_L, \mu_R$ . The distributions of the uncorrelated electrons are then described by Fermi functions,  $f_\ell(\epsilon_q) = (1 + \exp(\epsilon_q - \mu_\ell / k_B T))^{-1}$  and, thus, the density operator of the leads can be written as

$$\rho_{\text{leads,eq}} \propto \exp[-(H_{\text{leads}} - \mu_L N_L - \mu_R N_R) / k_B T], \quad (2.6)$$

where  $N_\ell = \sum_q c_{q\ell}^\dagger c_{q\ell}$  denotes the electron number in lead  $\ell = L, R$ . Then, all lead properties can be expressed in terms of the expectation value

$$\langle c_{\ell q}^\dagger c_{\ell' q'} \rangle = \delta_{\ell\ell'} \delta_{qq'} f_\ell(\epsilon_q). \quad (2.7)$$

An applied source-drain voltage  $V$  is assumed to influence the electro-chemical potentials symmetrically and, thus, will be mapped directly, via  $eV = \mu_R - \mu_L$  with the electron charge  $e$ , to the respective electro-chemical potentials. Note also that our approach includes the case of an oscillating source-drain voltage. It was shown that a gauge transformation can devolve the time dependence of the leads to the wire part of the Hamiltonian [24].

The interconnect between the parts is described by the coupling Hamiltonian which models the transfer of electrons from the first and the last dot,  $|1\rangle$  and  $|N\rangle$ , to the respective leads

## 2 The model Hamiltonian

$$H_{\text{coupling}} = \sum_q (V_{Lq} c_{Lq}^\dagger c_1 + V_{Rq} c_{Rq}^\dagger c_N) + \text{H.c.} \quad (2.8)$$

We restrict ourselves to a rate equation-like description by introducing the tunnel rate

$$\Gamma_\ell(\epsilon) = 2\pi \sum_q |V_{\ell q}|^2 \delta(\epsilon - \epsilon_q), \quad (2.9)$$

which equals in the weak-coupling limit the tunnel rates obtained with Fermi's golden rule. For the case of dense lead states,  $\Gamma_\ell$  becomes a continuous function of the energy  $\epsilon$ . If all relevant lead states are located in the centre of the conduction band, the energy dependence of the spectral densities is not relevant so that they can be replaced by a constant,  $\Gamma_\ell(\epsilon) = \Gamma_\ell$ . This defines the so-called wide-band limit, in accordance with our focus on the description of the dynamics of the system, not of the junction itself.

## 3 Charge, current and noise

In most experiments with a lead–wire–lead structure, the current being the number of transported electrons per time is the central quantity of interest. The current measured in a real experiment is not a perfectly smooth curve but fluctuates. Such a noisy signal might origin from external fluctuations acting on the system, a source that never can be eliminated completely. If this fluctuations are an intrinsic feature of the transport process, i.e., stemming from processes inside the conductor, it raises the question for the underlying physical reasons: The discreteness of charge carriers gives rise to detectable statistical fluctuations in the current that obey Poissonian statistics if the charges are supposed to arrive randomly. If correlations among the electrons are taken into account, it turns out that deviations from Poissonian behaviour (can) occur.

### 3.1 Current-current correlator

As starting point to our evaluation of the physical quantities current and noise, we choose the operator

$$Q_\ell(t) = eN_\ell(t) - eN_\ell(t_0) \quad (3.1)$$

which describes the charge accumulated in lead  $\ell$  with respect to the initial state. Due to total charge conservation,  $Q_\ell$  equals for two-terminal devices the net charge transmitted across the contact  $\ell$ ; its time derivative defines the corresponding current

$$I_\ell(t) = \frac{d}{dt}Q_\ell(t). \quad (3.2)$$

The reason for this definition lies in its good applicability to our, later presented, Floquet approach. Of course, one could equivalently define the current as  $c_n^\dagger c_{n+1} - c_{n+1}^\dagger c_n$  between sites  $n$  and  $n + 1$  inside the system. But this definition would cause difficulties in the upcoming calculations when we want to evaluate the current and its moments in the energy-eigenbasis, so we will from now on use (3.2).

To measure the current fluctuations, we will employ the current noise, described by the symmetrised correlation function

$$S_\ell(t, t') = \frac{1}{2} \langle [\Delta I_\ell(t), \Delta I_\ell(t')]_+ \rangle \quad (3.3)$$

### 3 Charge, current and noise

of the current fluctuation operator  $\Delta I_\ell(t) = I_\ell(t) - \langle I_\ell(t) \rangle$ , where the anticommutator  $[A, B]_+ = AB + BA$  ensures hermiticity. If  $S$  is very small compared to the current, the transport is highly regular, vice versa a large current noise indicates that electrons are transported in bunches. At long times,  $S_\ell(t, t') = S_\ell(t + \mathcal{T}, t' + \mathcal{T})$  shares the time-periodicity of the driving [24], which turns out to be crucial in the numerical treatment. Therefore, it is possible to characterise the noise level by the zero-frequency component of  $S_\ell(t, t - \tau)$  averaged over one driving period,

$$\bar{S}_\ell = \frac{1}{\mathcal{T}} \int_0^{\mathcal{T}} dt \int_{-\infty}^{\infty} d\tau S_\ell(t, t - \tau). \quad (3.4)$$

The fact that we drive our systems with microwaves justifies this restriction since the requirements for the time resolution in an experiment would be extremely high. Moreover, for lead-wire-lead devices which we consider throughout this work, it can be shown that  $\bar{S}_\ell$  is independent of the contact  $\ell$ , i.e.,  $\bar{S}_L = \bar{S}_R \equiv \bar{S}$ .

The evaluation of the zero-frequency noise  $\bar{S}$  directly from its definition (3.4) can be tedious due to the explicit appearance of both times,  $t$  and  $t - \tau$ . This inconvenience can be circumvented by employing the relation

$$\frac{d}{dt} \left( \langle Q_\ell^2(t) \rangle - \langle Q_\ell(t) \rangle^2 \right) = 2 \int_0^{\infty} d\tau S_\ell(t, t - \tau), \quad (3.5)$$

which follows from the integral representation of eqs. (3.1) and (3.2), and

$$Q_\ell(t) = \int_{t_0}^t dt' I_\ell(t'), \quad (3.6)$$

in the limit  $t_0 \rightarrow -\infty$ . By averaging eq. (3.5) over one driving period and using  $S(t, t - \tau) = S(t - \tau, t)$ , we obtain

$$\bar{S} = \left\langle \frac{d}{dt} \langle \Delta Q_\ell^2(t) \rangle \right\rangle_t, \quad (3.7)$$

where  $\Delta Q_\ell = Q_\ell - \langle Q_\ell \rangle$  denotes the charge fluctuation operator and  $\langle \dots \rangle_t$  the time average. The fact that the time average can be evaluated from the limit

$$\bar{S} = \lim_{t_0 \rightarrow -\infty} \frac{\langle \Delta Q_\ell^2(t) \rangle}{t - t_0} > 0 \quad (3.8)$$

allows one to interpret the zero-frequency noise as the ‘‘charge diffusion coefficient’’.

A widely used dimensionless measure to describe the relative noise strength is the so-called Fano-factor [25–27],

$$F = \frac{\bar{S}}{e|\bar{I}|}, \quad (3.9)$$

which provides insight to the physical nature of the transport mechanisms. Historically, the zero-frequency noise (3.4) contains a factor 2, i.e.,  $\bar{S}' = 2\bar{S}$ , resulting



from a different definition of the Fourier transform. Then, the Fano factor is defined as  $F = \bar{S}'/2e|\bar{I}|$ . If the Fano factor is exactly one, the transport statistic is Poissonian, meaning that all single events are uncorrelated, while a Fano factor smaller than one indicates that the transport is sub-Poissonian, i.e., more regular. Analogous, a Fano factor larger than one occurs in very noisy transport and one refers to super-Poissonian statistics.

## 3.2 Full Counting Statistics

A recently developed picture of noise in quantum transport is the so-called Full Counting Statistics [14], which is based on the complete knowledge of the moments of a probability distribution by counting all single tunnel events. Generally, moments are expectation values calculated using the probability distribution, in our case the probability distribution of the number of electrons in one of the leads. The l.h.s. of eq. (3.5) already hints to a possible way to compute the noise characteristics. Since it depends solely on expectation values or moments of the type  $\langle Q_\ell^k \rangle = e^k \langle N_\ell^k \rangle$ , we want to find a scheme to compute such moments systematically.

The method of choice are the Full Counting Statistics, adopted recently to quantum transport [14], while it has a rather long tradition in quantum optics [13]. It bases on the idea that by counting every single process one obtains ultimately the complete probability distribution of the considered variable. As pointed out before, all moments depend on the number of electrons in one lead (3.1) viz. (3.5), so we have to work with the probability distribution  $P(N_L, t)$  to find  $N_L$  electrons in, e.g., the left lead at time  $t$ .

Assume we measure the current in time steps larger than any intrinsic time scale of the system and make a histogram of the number of electrons transported in every interval. We obtain a probability distribution which can be fully described by the moments or its cumulants. Both contain the same information, but for simplicity we start with the definition of the moments. We define the  $k$ -th moment  $M_k$  of a probability distribution  $P(x)$  as

$$\langle M_k \rangle_t = \int_{-\infty}^{\infty} x^k P(x, t) dx, \quad (3.10)$$

where  $x$  denotes the number of transported electrons. Note that we drop often the time-dependence for the sake of readability. The integration over a probability function yields an expectation value at time  $t$ , indicated by  $\langle \dots \rangle_t$  and obviously the first moment  $\langle M_1 \rangle$  equals the average value measured. The second moment is generally not stated solely but used to calculate the variance

$$\text{Var}(x) = M_2 - M_1^2, \quad (3.11)$$

which indicates the width of the probability distribution. Instead of the variance, very often the standard deviation  $\sigma = \sqrt{\text{Var}(x)}$  is given.

### 3 Charge, current and noise

The probability distribution  $P(N_L, t)$  can be computed as follows. The quantity of interest here is the number of electrons in the left lead  $N_L$ . Its time derivative is the current, since the total charge is conserved. For the same reason it is feasible to substitute  $x$  by  $N_L$ , which results only in a constant shift of the probability distribution. A more systematic way to access the moments is the use of the so-called moment generating function, which we obtain after a Fourier transform of eq. (3.10)

$$\begin{aligned}\phi(\chi, t) &= \int_{-\infty}^{\infty} \exp^{i\chi N_L} P(N_L, t) dN_L \\ &= \langle \exp^{i\chi N_L} \rangle_t\end{aligned}\quad (3.12)$$

and allows the direct computation of the  $k$ -th moment of the charge in the left lead via the relation

$$\langle Q_L^k(t) \rangle = e^k \frac{\partial^k}{\partial (i\chi)^k} \phi(\chi, t) \Big|_{\chi=0}. \quad (3.13)$$

By subtracting from the moments all the trivial contributions depending on a shift of the initial values, one obtains the cumulants. They are defined and generated via the cumulant generating function  $\ln \phi(\chi, t)$  which replaces  $\phi$  in eq. (3.13) [28], so that the  $k$ -th cumulant is defined as

$$C_k = e^k \frac{\partial^k}{\partial (i\chi)^k} \ln \phi(\chi, t) \Big|_{\chi=0}. \quad (3.14)$$

It is straightforward to compute the first and second moments and cumulants which we relate to each other and obey

$$\begin{aligned}C_1 &= \langle N_L \rangle = M_1, \\ C_2 &= \langle N_L^2 \rangle - \langle N_L \rangle^2 = M_2 - M_1^2.\end{aligned}\quad (3.15)$$

Note that all higher moments than the first are not affected by changing the average. i.e., the first cumulant. We see that the first moment and the first cumulant coincide, while the second cumulant is exactly the afore-defined variance (3.11) that measures the width of the probability distribution.

Still, one can analyse higher cumulants that are very often renormalised by dividing with  $\sigma^n$  for the  $n$ -th cumulant. The third cumulant, measures the wryness of the distribution, i.e., it indicates if the weight of the tail is higher on the right side (positive) or on the left side (negative). For a symmetric distribution, the third cumulant is obviously zero. After the normalisation, one refers to the third cumulant as skewness. The kurtosis is defined as the normalised fourth cumulant and gauges the sharpness of the distribution compared to a normal distribution with the same variance. A very broad distribution with a distinct peak shows a large kurtosis, while for a bounded distribution the kurtosis is rather small. All higher cumulants are unnamed, but specify with higher and higher precision the probability distribution  $P(N_L, t)$ , see fig. 3.1.

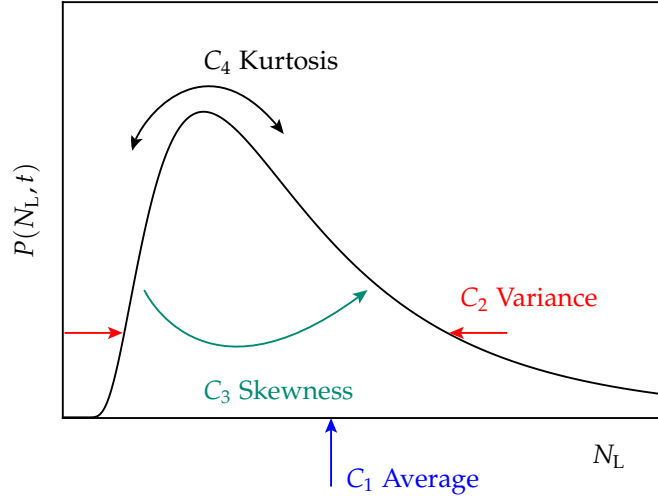


Figure 3.1: Probability distribution  $P(N_L, t)$  and its respective cumulants.

Turning back to the physical interpretation of the cumulants, we note that in a continuum limit for the leads, both the moments and the cumulants diverge as a function of time and one focusses on the rates at which these quantities change in the long-time limit. This establishes between the first two cumulants and  $I(t)$  and  $S(t)$  the relations

$$I(t) = -ie \frac{\partial}{\partial \chi} \frac{d}{dt} C(\chi, t) \Big|_{\chi=0} \quad (3.16)$$

$$S(t) = -e^2 \frac{\partial^2}{\partial \chi^2} \frac{d}{dt} C(\chi, t) \Big|_{\chi=0}. \quad (3.17)$$

As we have seen already before, for driven systems, these quantities are time-dependent even in the asymptotic limit and, thus, we characterise the transport by the corresponding averages over one driving period. Then expressions (3.16) and (3.17) become identical to the previously defined time averages  $\bar{I}$  and  $\bar{S}$ , respectively.

Herein we restrict ourselves to the computation of the first and the second cumulant, despite the fact that also higher-order cumulants have been studied for static conductors [29, 30].

### *3 Charge, current and noise*

## 4 Master equation approach for current and noise

Quantum transport in mesoscopic systems is mainly observed via the dc current passing through the system. A very intuitive approach to this transport processes bases on the Landauer scattering formula [31, 32] and its various extensions. The assumption that the current [33] and its fluctuations [26, 34] can be described with quantum mechanical transition probabilities raises some questions, for example if this model complies with the Pauli principle or if it contains electron-electron interactions. Moreover, when external driving fields deliver energy to the system, allowing inelastic scattering processes where an electron can absorb or emit an energy quantum of the field [35–37] the scattering approach is at least questionable.

In the presence of electron-electron interactions, an exact treatment of the electron transport within a scattering theory is no longer possible and a master equation formalism can be an appropriate tool for the computation of currents [38–45]. Recently, master equations have been established for the computation of current noise of various static conductors as well [12, 17, 46–51]. In the following, we develop such an approach for the case of periodically time-dependent conductors.

### 4.1 Perturbation theory and reduced density operator

We start our derivation of a master equation formalism from the Liouville-von Neumann equation  $i\hbar\dot{\mathcal{R}}(t) = [H(t), \mathcal{R}(t)]$  for the total density operator  $\mathcal{R}(t)$  of the complete system. We will focus on the central region by tracing out the leads and treating their influence on the system within a perturbational approach in the weak coupling limit. An obvious downside of this perturbation theory is the neglect of physical effects based on a strong coupling. The most famous effect for which a master equation approach is not useful, is the Kondo effect. Furthermore coherence and entanglement effects stemming from the bath are not treatable within this approach. However, we can evaluate in our approximation the complete quantum mechanics taking place on the central system exactly and are not strictly limited with the system size. Applying perturbation theory with respect to the coupling between leads and system, the final master equation can be found in several text books [52, 53]. However, we will give a short introduction for the reader.

From standard quantum mechanics follows that the total density operator  $\mathcal{R}(t)$  obeys

#### 4 Master equation approach for current and noise

$$\tilde{\mathcal{R}}(t) = e^{i(H_{\text{leads}}+H_{\text{wire}})t/\hbar}\mathcal{R}(t)e^{-i(H_{\text{leads}}+H_{\text{wire}})t/\hbar}, \quad (4.1)$$

where the tilde denotes the interaction picture with respect to the coupling Hamiltonian. The Liouville-von Neumann equation governs the time evolution of the complete density operator  $\tilde{\mathcal{R}}$

$$i\frac{d}{dt}\tilde{\mathcal{R}}(t) = [\tilde{H}_{\text{wire-leads}}(t), \tilde{\mathcal{R}}(t)], \quad (4.2)$$

which reads after a formal time integration

$$\tilde{\mathcal{R}}(t) = \mathcal{R}(0) - i\int_0^t dt' [\tilde{H}_{\text{wire-leads}}(t'), \tilde{\mathcal{R}}(t')]. \quad (4.3)$$

This expression for the density operator in the interaction picture is still exact and we reinsert it into eq. (4.2) to obtain

$$\begin{aligned} \frac{d}{dt}\tilde{\mathcal{R}}(t) = & -\frac{i}{\hbar}[\tilde{H}_{\text{wire-leads}}(t), \mathcal{R}(0)] \\ & -\frac{1}{\hbar^2}\int_0^\infty dt' [\tilde{H}_{\text{wire-leads}}(t), [\tilde{H}_{\text{wire-leads}}(t'), \tilde{\mathcal{R}}(t')]]. \end{aligned} \quad (4.4)$$

We truncate our self-consistent solution of the integro-differential equation for  $\tilde{\mathcal{R}}(t)$  after the second order, to which is often referred as Born approximation. Since we are interested in the dynamics of the reduced system ("wire") we trace out the influence of the surrounding bath and denote

$$\rho_{\text{wire}}(t) = \text{tr}_{\text{leads}} \tilde{\mathcal{R}}(t), \quad (4.5)$$

as the reduced density matrix  $\rho_{\text{wire}}(t)$ . The index "wire" is only used if there is the danger of misunderstanding, otherwise it is dropped. We perform the same operation on eq. (4.4) and use as initial condition a factorisation for our complete density matrix

$$\mathcal{R}(0) = \rho_{\text{leads}} \otimes \rho_{\text{wire}}(0). \quad (4.6)$$

Note that we already employed this when discussing the Hamiltonian of the reservoirs, see eq. (2.6). Furthermore we implicitly used another approximation namely that the state of our complete system remains for all times a product state of bath states and wire states and thus reads

$$\tilde{\mathcal{R}}(t) \approx \rho_{\text{leads}} \otimes \tilde{\rho}_{\text{wire}}(t). \quad (4.7)$$

This approximation is valid, if the influence of the bath onto the system and a possible back action can be neglected which is the case if (i) the coupling between the two systems is rather weak, so their mutual influence is small, and (ii) the leads are very large compared to the wire, which renders the effect of the limited wire

## 4.2 Computation of moments and cumulants

states onto each of the large number of bath states negligible. The Markov approximation,  $t' \rightarrow t$  in the double commutator (4.4), results in a time-local differential equation without memory that eases the numerical calculations [54, 55].

Finally, we obtain the master equation in a closed form after the back transformation to the Schrödinger picture

$$\begin{aligned} \frac{d}{dt}\rho(t) = & -\frac{i}{\hbar}[H_{\text{wire}}(t) + H_{\text{leads}}, \rho(t)] \\ & -\frac{1}{\hbar^2} \int_0^\infty d\tau [H_{\text{wire-leads}}, [\tilde{H}_{\text{wire-leads}}(t-\tau, t), \rho(t)]] . \end{aligned} \quad (4.8)$$

## 4.2 Computation of moments and cumulants

In this section we develop a formalism to obtain systematically higher moments of the charge distribution, but especially the current (3.2) and the noise (3.5) [56]. The fact that they are expectation values in combination with our quantum mechanical treatment requires that we use the density operator instead of a classical probability distribution.

Consequently, we employ the moment generating function  $\phi(\chi) = \langle \exp(i\chi N_L) \rangle$ . It contains all information of the full counting statistics and in order to compute it explicitly, we define in the Hilbert space of the wire the operator

$$\mathcal{F}(\chi, t) = \text{tr}_{\text{leads}} \{ e^{i\chi N_L} \mathcal{R}(t) \} . \quad (4.9)$$

Comparing the case of  $\chi \rightarrow 0$  with eq. (4.5), one easily realizes that  $\mathcal{F}(0, t) = \rho(t)$ . Tracing out the leads degrees of freedom, the operator  $\mathcal{F}$  transforms to the moment generating function  $\phi(\chi, t) = \text{tr}_{\text{wire}} \mathcal{F}(\chi, t)$ . For the later evaluation of the full counting statistics, we expand  $\mathcal{F}$  into a Taylor series,

$$\mathcal{F} = \rho + \sum_{k=1}^{\infty} \frac{(i\chi)^k}{k!} \mathcal{F}_k , \quad (4.10)$$

where the coefficients  $\mathcal{F}_k = \text{tr}_{\text{leads}}(N_L^k \mathcal{R})$  provide direct access to the moments  $\langle N_L^k \rangle = \text{tr}_{\text{wire}} \mathcal{F}_k$ .

The structure of the Fourier coefficients  $\mathcal{F}_k$  and the identity  $\mathcal{F}_0 = \rho$  motivates a step-by-step evaluation of the coefficients for  $k > 1$ . Starting from the master equation for the full density operator in the interaction picture  $\tilde{\mathcal{R}}$ , eq. (4.4), we perform a transformation back into the Schrödinger picture. Then, we multiply from the left by the operator  $\exp(i\chi N_L)$ , which already has a similar structure as eq. (4.9). After tracing out the leads, we obtain

$$\frac{d}{dt} \mathcal{F}(\chi, t) = \{ \mathcal{L} + (e^{i\chi} - 1) \mathcal{J}_+ + (e^{-i\chi} - 1) \mathcal{J}_- \} \mathcal{F}(\chi, t) , \quad (4.11)$$

where we used the commutation relations  $[N_L, V] = V$  and  $[N_L, V^*] = -V^*$  with

#### 4 Master equation approach for current and noise

$$\begin{aligned}
V &= \sum_q V_{Lq} c_{Lq}^\dagger c_1, \\
V^* &= \sum_q V_{Lq}^* c_1^\dagger c_{Lq},
\end{aligned} \tag{4.12}$$

stemming from the coupling Hamiltonian. To save the reader from cumbersome and lengthy formulas, we introduce the super-operators  $\mathcal{J}_\pm$  and the time-dependent Liouville operator

$$\begin{aligned}
\mathcal{L}(t) X &= -\frac{i}{\hbar} [H_{\text{wire}}(t), X] \\
&+ \frac{\Gamma_L}{2\pi} \int_0^\infty d\tau \int d\epsilon \left[ e^{i\epsilon\tau/\hbar} (\tilde{c}_1^\dagger X c_1 f_L(\epsilon) - c_1 \tilde{c}_1^\dagger X f_L(\epsilon) - X \tilde{c}_1^\dagger c_1 \bar{f}_L(\epsilon) + c_1 X \tilde{c}_1^\dagger \bar{f}_L(\epsilon)) \right. \\
&\quad \left. + e^{-i\epsilon\tau/\hbar} (c_1^\dagger X \tilde{c}_1 f_L(\epsilon) - X \tilde{c}_1 c_1^\dagger f_L(\epsilon) - c_1^\dagger \tilde{c}_1 X \bar{f}_L(\epsilon) + \tilde{c}_1 X c_1^\dagger \bar{f}_L(\epsilon)) \right] \\
&+ \text{same terms with the replacement } 1, L \rightarrow N, R,
\end{aligned} \tag{4.13}$$

which also determines the time-evolution of the reduced density operator,  $\dot{\rho} = \mathcal{L}(t) \rho$ . Again, interaction picture operators are denoted by a tilde, e.g.,  $\tilde{c}_1 = \tilde{c}_1(t, t - \tau)$  and  $f_\ell$  is the Fermi function of lead  $\ell$ , while  $\bar{f}_\ell = 1 - f_\ell$ . We will refer to the super-operators

$$\mathcal{J}_+(t) X = \frac{\Gamma_L}{2\pi} \int_0^\infty d\tau \int d\epsilon (e^{i\epsilon\tau/\hbar} \tilde{c}_1^\dagger X c_1 + e^{-i\epsilon\tau} c_1^\dagger X \tilde{c}_1) f_L(\epsilon) \tag{4.14}$$

$$\mathcal{J}_-(t) X = \frac{\Gamma_L}{2\pi} \int_0^\infty d\tau \int d\epsilon (e^{i\epsilon\tau/\hbar} c_1 X \tilde{c}_1^\dagger + e^{-i\epsilon\tau} \tilde{c}_1 X c_1^\dagger) \bar{f}_L(\epsilon) \tag{4.15}$$

as current operators, which reflects their physical interpretation. The operator  $\mathcal{J}_+$  describes the tunnelling of an electron from a state occupied with probability  $f$  in the left lead to the empty wire, while  $\mathcal{J}_-$  denotes the tunnelling out of an electron to a free lead state, which is proportional to  $\bar{f}$ . Please note that these super-operators inherit a non-trivial time dependence from the interaction picture representation of the creation and annihilation operators they contain.

Following the calculations presented in Ref. [47], we are able to evaluate the current and the zero-frequency noise for a time-dependent situation. The time derivative of the operator  $\mathcal{F}$  up to second order in  $\chi$  fully describes the long-time behaviour of the first and the second moment of the charge distribution in the left lead and is sufficient to compute the zero-frequency noise and so the Fano factor. By Taylor expansion of the equation of motion (4.11) we arrive at the coupled set of equations

$$\dot{\rho} = \mathcal{L}(t) \rho \tag{4.16}$$

$$\dot{\mathcal{F}}_1 = \mathcal{L}(t) \mathcal{F}_1 + (\mathcal{J}_+(t) - \mathcal{J}_-(t)) \rho \tag{4.17}$$

$$\dot{\mathcal{F}}_2 = \mathcal{L}(t) \mathcal{F}_2 + 2(\mathcal{J}_+(t) - \mathcal{J}_-(t)) \mathcal{F}_1 + (\mathcal{J}_+(t) + \mathcal{J}_-(t)) \rho. \tag{4.18}$$



The first equation determines the time-evolution of the reduced density operator, which in the long-time limit becomes the stationary solution  $\rho_0(t)$ . For driven systems, also the stationary solution is still time-dependent. Substituting in Eq. (4.17)  $\rho$  by  $\rho_0$  and employing that  $\text{tr}_{\text{wire}} \mathcal{L}X = 0$  for any operator  $X$ , the stationary current reads

$$I(t) = -e \text{tr}_{\text{wire}} \dot{\mathcal{F}}(t)_1 = -e \text{tr}_{\text{wire}} (\mathcal{J}_+ - \mathcal{J}_-) \rho_0(t). \quad (4.19)$$

Performing an average over one driving period reproduces the current formula of Ref. [57]. In the numerical evaluation of  $\mathcal{F}_1$  one encounters a difficulty, since in general the inverse of a Liouvillian does not exist. This is trivial for static systems: The stationary solution is defined as  $\mathcal{L}\rho_0 = 0$ , which classifies  $\mathcal{L}$  as a singular matrix. To overcome this issue in the computation of the second cumulant, we circumvent it as follows. Eq. (3.5) links the charge fluctuations in the leads with the zero-frequency noise. Further, we can express the time derivative of the first and the second moment of the electron number in the left lead using the operators  $\dot{\mathcal{F}}_{1,2}$ . Combining the equations of motion (4.17) and (4.18) and the fact that  $\text{tr}_{\text{wire}} \mathcal{L}X = 0$ , the zero-frequency noise reads

$$S = e^2 \text{tr}_{\text{wire}} \{2(\mathcal{J}_+ - \mathcal{J}_ - I)\mathcal{F}_1 + (\mathcal{J}_+ + \mathcal{J}_-)\rho\}. \quad (4.20)$$

Note that if  $\mathcal{F}_1 \propto \rho_0$ , the first part of  $S$  vanishes exactly, which is easily verified by inserting the current expectation value (4.19). Using the projection properties of the outer product  $\rho_0 \text{tr}_{\text{wire}}$ , we can split  $\mathcal{F}_1$  into two parts

$$\mathcal{F}_{1\perp} = \mathcal{F}_1 - \rho_0 \text{tr}_{\text{wire}} \mathcal{F}_1, \quad (4.21)$$

for which  $\text{tr}_{\text{wire}} \mathcal{F}_{1\perp} = 0$  holds true and its equation of motion reads

$$\dot{\mathcal{F}}_{1\perp} = \mathcal{L}(t) \mathcal{F}_{1\perp} + (\mathcal{J}_+(t) - \mathcal{J}_-(t) - I(t))\rho_0(t). \quad (4.22)$$

By projecting out the diverging parts of  $\mathcal{F}_1$ , the direct computation of the long-time limit of the traceless  $\mathcal{F}_{1\perp}$  is feasible. Using Eq. (4.21) together with the equation of motion (4.18), we obtain for the still time-dependent ‘‘charge diffusion coefficient’’

$$S(t) = e^2 \text{tr}_{\text{wire}} \{2(\mathcal{J}_+ - \mathcal{J}_-)\mathcal{F}_{1\perp} + (\mathcal{J}_+ + \mathcal{J}_-)\rho_0\}, \quad (4.23)$$

whose time average finally provides the Fano factor  $F = \bar{S}/e\bar{I}$ .

### 4.3 Explicit form of current and noise

Now, we focus on the evaluation of the master equation and the current formula within an Floquet approach. Most convenient, one decomposes both, the master equation and the current formula into the Floquet basis.

#### 4 Master equation approach for current and noise

An introduction to Floquet theory in general can be found in Appendix A, here we state only the most important facts. We exploit the time-periodicity, i.e., that time shifts by multiples of the driving period  $\mathcal{T}$  leave the system unchanged, by rewriting our Hamiltonian into a rotating frame. The eigenstates of this new basis are the time-periodic Floquet-states

$$|\varphi_\alpha(t)\rangle = |\varphi_\alpha(t + \mathcal{T})\rangle \quad (4.24)$$

and the corresponding eigenenergies, often called quasi-energies,  $\epsilon_\alpha$ . The time-periodicity reflects in the fact that eigenenergies differing by the driving energy  $\hbar\Omega$  describe the same physical situation, similar to Bloch-electrons in different Brillouin zones.

The creation/annihilation operators in the onsite-basis transform via

$$c_\alpha(t) = \sum_n \langle \varphi_\alpha(t) | n \rangle c_n. \quad (4.25)$$

to the Floquet-basis and thus can be substituted in the current super-operators (4.14) and the Liouvillian (4.13). It can be shown, see Appendix A eq. (A.23), that the interaction representation of the Floquet operators reads

$$\begin{aligned} \tilde{c}_\alpha(t, t') &= U_0^\dagger(t, t') c_\alpha(t) U_0(t, t') \\ &= e^{-i(\epsilon_\alpha + U\mathcal{N}_{\text{wire}})(t-t')/\hbar} c_\alpha(t'). \end{aligned} \quad (4.26)$$

Since we work in the limit of very strong Coulomb repulsion  $U$  on the central system, one particle states are already sufficient to describe the physical situation correctly. The infinite Coulomb repulsion renders a second excess charge in the central region impossible. This has the consequence that only wire states with at most one excess electron play a role, so that the reduced density operator  $\rho_{\text{wire}}$  can be decomposed into the  $N + 1$  dimensional basis  $\{|0\rangle, c_\alpha^\dagger(t)|0\rangle\}$ , where  $|0\rangle$  denotes the wire state in the absence of an excess electron. Moreover, we are only interested in the case of asymptotically long times and it has been shown that the density operator  $\rho_{\text{wire}}$  becomes diagonal in the electron number  $\mathcal{N}_{\text{wire}}$ . So, a proper ansatz for the density operator of the reduced systems reads

$$\rho_{\text{wire}}(t) = |0\rangle\rho_{00}(t)\langle 0| + \sum_{\alpha, \beta} c_\alpha^\dagger |0\rangle \rho_{\alpha\beta}(t) \langle 0| c_\beta. \quad (4.27)$$

The fact that we keep terms in which  $\alpha \neq \beta$  means that we work beyond a rotating wave approximation. This approximation bears the risk of obtaining artifacts in a non-equilibrium situation [45, 58] stemming from non-vanishing off-diagonal elements  $\rho_{\alpha\beta}$ .

Inserting the decomposed density operator (4.27) into the master equation (4.16), we obtain an equation of motion for every matrix element  $\rho_{\alpha\beta} = \langle 0| c_\alpha \rho_{\text{wire}} c_\beta^\dagger |0\rangle$ . Now we can compute the trace over the leads and evaluate the matrix element  $\langle 0| c_\alpha \dots c_\beta^\dagger |0\rangle$ . In agreement to our physical reasoning before all matrix elements

### 4.3 Explicit form of current and noise

which contain two-particle states of the type  $c_\alpha^\dagger c_\beta^\dagger |0\rangle\langle 0| c_\beta c_\alpha$  drop. Formally, these terms vanish in the limit of strong Coulomb repulsion because they are accompanied by a rapidly oscillating phase factor  $\exp(-iU\mathcal{N}_{\text{wire}}\tau/\hbar)$ . By performing the  $\tau$ -integration, this phase results in a factor  $f_L(\epsilon_{\alpha,k} + U)$  which disappears in the limit of large  $U$ .

At this point, we can capitalise again on the time periodicity of the Hamiltonian, and therefore write the density operator  $\rho_{\text{wire}}$ , and so every single of its elements, as a Fourier series

$$\rho_{\alpha\beta}(t) = \sum_k e^{-ik\Omega t} \rho_{\alpha\beta,k} \quad (4.28)$$

and  $\rho_{00}(t)$  accordingly. Note that we now can derive the Liouvillian  $\mathcal{L}$  as well as the current super-operators  $\mathcal{J}_\pm$  in Floquet representation. As an example we evaluate only the Liouvillian and after some lengthy and tedious algebra we obtain a set of  $N^2$  coupled equations of motion for the  $\rho_{\alpha\beta}$ . Then the master equation for a single entry of the density operator reads

$$\begin{aligned} & i(\epsilon_\alpha - \epsilon_\beta - k\hbar\Omega)\rho_{\alpha\beta,k} \\ &= \frac{\Gamma_L}{2} \sum_{k',k''} \langle \varphi_{\alpha,k'+k''} | 1 \rangle \langle 1 | \varphi_{\beta,k+k''} \rangle \rho_{00,k'} (f_L(\epsilon_{\alpha,k'+k''}) + f_L(\epsilon_{\beta,k+k''})) \\ & - \frac{\Gamma_L}{2} \sum_{\alpha',k',k''} \langle \varphi_{\alpha,k'+k''} | 1 \rangle \langle 1 | \varphi_{\alpha',k+k''} \rangle \rho_{\alpha'\beta,k'} \bar{f}_L(\epsilon_{\alpha',k+k''}) \\ & - \frac{\Gamma_L}{2} \sum_{\beta',k',k''} \langle \varphi_{\beta',k'+k''} | 1 \rangle \langle 1 | \varphi_{\beta,k+k''} \rangle \rho_{\alpha\beta',k'} \bar{f}_L(\epsilon_{\beta',k'+k''}) \\ & + \text{same terms with the replacement } 1, L \rightarrow N, R. \end{aligned} \quad (4.29)$$

A convenient way to solve this set of equations is the substitution of  $\rho_{00,k'}$  by the Fourier representation of the normalisation condition

$$\text{tr } \rho_{\text{wire}}(t) = \rho_{00}(t) + \sum_\alpha \rho_{\alpha\alpha}(t) = 1. \quad (4.30)$$

To obtain for the current an expression that is consistent with the restriction to one excess electron, we compute the expectation values for the current formula (4.19) with the reduced density operator (4.27) and insert the Floquet representation (A.22) of the wire operators. Performing an average over one driving period, the dc current reads

$$\begin{aligned} I = \frac{2e\Gamma_L}{\hbar} \text{Re} \sum_{\alpha,k} \left( \sum_{\beta,k'} \langle \varphi_{\beta,k'+k} | 1 \rangle \langle 1 | \varphi_{\alpha,k} \rangle \rho_{\alpha\beta,k'} \bar{f}_L(\epsilon_{\alpha,k}) \right. \\ \left. - \sum_{k'} \langle \varphi_{\alpha,k'+k} | 1 \rangle \langle 1 | \varphi_{\alpha,k} \rangle \rho_{00,k'} f_L(\epsilon_{\alpha,k}) \right). \end{aligned} \quad (4.31)$$

#### 4 Master equation approach for current and noise

Physically, the second contribution of the current formula (4.31) describes the tunnelling of an electron from the left lead to the wire and, thus, is proportional to  $\rho_{00}f_L$  which denotes the probability that a lead state is occupied while the wire is empty. The first term corresponds to the reversed process namely the tunnelling of an electron from site  $|1\rangle$  to the left lead. In this manner the current formula can be interpreted as a rate equation. Note that in the undriven case, all non-vanishing contributions have sideband index  $k = 0$ , such that the index  $k$  can be dropped.

The decomposition of the equation of motion (4.22) for the long-time limit of  $\mathcal{F}_{1\perp}$  and the subsequent computation of  $\bar{S}$  from eq. (4.23) proceeds along the same lines with the only difference that the current operators  $\mathcal{J}_{\pm}$  yield an inhomogeneity and that the r.h.s. of the trace condition (4.30) is

$$\mathrm{tr}_{\mathrm{wire}} \mathcal{F}_{1\perp} = (\mathcal{F}_{1\perp})_{00} + \sum_{\alpha} (\mathcal{F}_{1\perp})_{\alpha\alpha} = 0. \quad (4.32)$$

The results of this section allow us the numerical computation of the dc current through a driven conductor in the following way: First, we solve the quasienergy equation (A.9) which provides the coefficients  $\langle \varphi_{\alpha,k} | n \rangle$ . Next, we solve the master equation (4.29) and insert the solution into the current formula (4.31) and the noise formula.

## 5 Pump current and noise in non-adiabatically driven nanosystems

A phenomenon, well studied both theoretically and experimentally, is non-adiabatic electron pumping in a double quantum dot. A spatial asymmetry in combination with ac driving can create pump currents, i.e., a current flowing in the absence of any net bias voltage [59–66]. The decisive symmetry that must be broken is the so-called generalised parity defined as the invariance under spatial reflection in combination with a time shift of half a driving period [45]. Experimentally it is possible to break such internal symmetries by applying suitable gate voltages.

It has been shown that for adiabatically slow driving, the transported charge per cycle is proportional to the area enclosed in parameter space during the cycle [67]. A direct consequence of this theorem is that for an adiabatically driven pump, the resulting current is proportional to the frequency. This indicates that pumping might be more efficient in the non-adiabatic case. Studies by several groups [3, 40, 61] have shown that the pump current induced by a non-adiabatic driving force can reach rather high values. In our theoretical study, the pump is modelled by a two level system with differing onsite energies for each dot (depicted in fig. 5.1). Then, an electron from the lower lying left state can be excited to the energetically higher state and leave the system to the right thus leading to a net current.

To model the time-dependent variation induced by the microwave, we set the interdot phase difference  $\Theta = \pi/2$ . Then, the resulting oscillations are identical to those obtained in a semiclassical treatment of the incident light and permit a comparison with results for non-interacting electrons [10].

For the case of non-interacting electrons, a treatment within a Floquet scattering approach has been demonstrated [10]. Surprisingly, the noise at frequencies that match the energy gap between the levels is clearly sub-Poissonian and so the corresponding Fano factor has pronounced minima at these frequencies.

Figure 5.2(a) shows the current characteristics for different driving frequencies  $\Omega$  and amplitudes  $A$  in the limit of strong Coulomb repulsion. The distinct horizontal blue spots on the left side demonstrate that whenever the energy gap can be bridged by the external field, a significant current emerges. The highest blue spot corresponds to a one-photon resonance, i.e., one energy quantum from the driving field is sufficient to overcome the internal energy barrier. The lower lying spots correspond to two or more photon processes. For a small frequency, the maximal pump current shows a clearly non-monotonic behaviour and the shimmery red

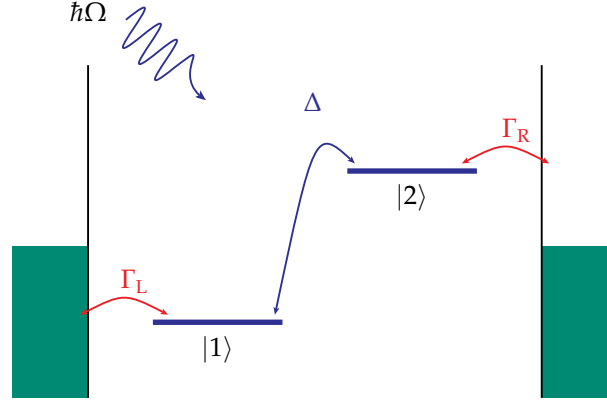


Figure 5.1: Level structure of a double quantum dot with  $N = 2$  orbitals. The terminating sites are coupled to leads with chemical potential  $\mu_L$  and  $\mu_R = \mu_L + eV$ , respectively.

areas between the resonance peaks indicate that the current even changes its sign, depending on the ratio between frequency and amplitude. For the non-interacting case, calculations were performed analytically [68]. They show that the matrix elements are dominated by Bessel functions  $J_\nu(A/\hbar\Omega)$ , where  $\nu$  reflects the order of the resonance. Our numerical results suggest a similar reason. Keeping in mind that if the amplitude is the dominating energy scale in the problem, it can be shown (Appendix A) that then the system can be described with an effective Hamiltonian, containing the zeroth order Bessel function. Note that for large driving amplitudes  $A$  and non-resonant frequencies  $\Omega$ , the current decays to zero and even exhibits very small negative values.

In Figure 5.2(b) the corresponding Fano factor is depicted. The blue areas represent regions with sub-Poissonian noise, i.e., a Fano factor smaller than one. As in the non-interacting case [10], they coincide with the resonances in the current, meaning that the maximum current is transported at minimum noise. Focusing on the high noise values for large driving amplitudes, we mentioned before that the current changes its sign, meaning that the absolute value is close to zero at certain values. If we interpret the current as the net difference of electrons in-going minus out-coming, and the noise as the sum, it becomes obvious that for vanishing current the fraction of this two number can assume extremely high values. This is observed in fig. 5.2(b) in the lower right corner, where the amplitude is large compared to the hopping matrix element and furthermore the highest values of the Fano factor occur at fixed ratios between  $\Omega$  and  $A$ , i.e., lie on a straight line.

We also performed a more detailed analysis of the situation for the driving amplitude  $A = 3.7\Delta$  for which the noise minima are very pronounced. In fig. 5.3 (a) the current for the Coulomb repulsion case is compared with the non-interacting situation of ref. [10]. Remarkably, the difference between the two cases is only in the order of 10%. We also find that the resonance peaks are slightly narrower in

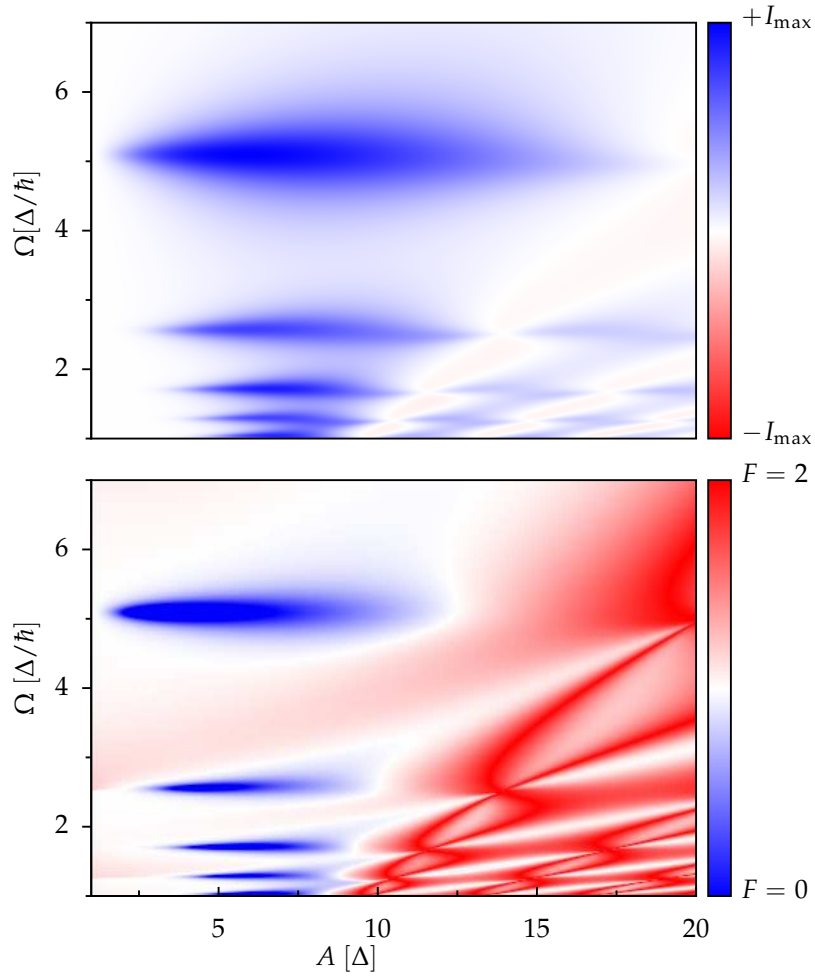


Figure 5.2: (a) Average current through the double quantum dot setup sketched in Fig. 5.1 as a function the driving frequency and amplitude. The dark area for  $\Omega \approx 3\Delta/\hbar$  marks the first-order resonance, while the other current maxima correspond to the nonlinear response. (b) Corresponding Fano factor. The white regions mark Poissonian noise ( $F \approx 1$ ), while at the resonances, the Fano factor is significantly smaller.

the case of large Coulomb interaction  $U = \infty$ . A similar behaviour has also been observed for photon-assisted transport in molecular wires [57].

The zero-frequency noise of the left contact depicted in fig. 5.3 (b) exhibits a double-peak structure with a local minimum at the centre. This leads to a pronounced minimum in the corresponding Fano factor (fig. 5.3 (c)). Its minimal value is  $F \approx 0.25$ , which is clearly sub-Poissonian. So the transport is highly regular at the resonances, whereas in the region between the resonances, it obeys Poissonian statistics.

### Conclusion

In this chapter we used our time-dependent generalised master equation to compute the Full Counting Statistics of a non-adiabatic electron pump. In doing so, we calculated the current and its noise characteristics for a driven system in the presence of very strong Coulomb repulsion. Comparing our results with the non-interacting case [10], we observed only differences in the order of 10% owing to the interaction. So, the remarkable results of a very low Fano factor at the resonance frequencies holds true even if the electrons interact inside the pump. Concluding this chapter, we can state that for both limits of the electron-electron interaction the conclusions from ref. [10] remain unaltered: The observation of low noise in a non-adiabatic electron pump requires a large internal bias in combination with a strong inter-dot coupling and resonant driving. By suitable tuning of the driving amplitude one achieves a relatively large pump current with clearly sub-Poissonian noise.



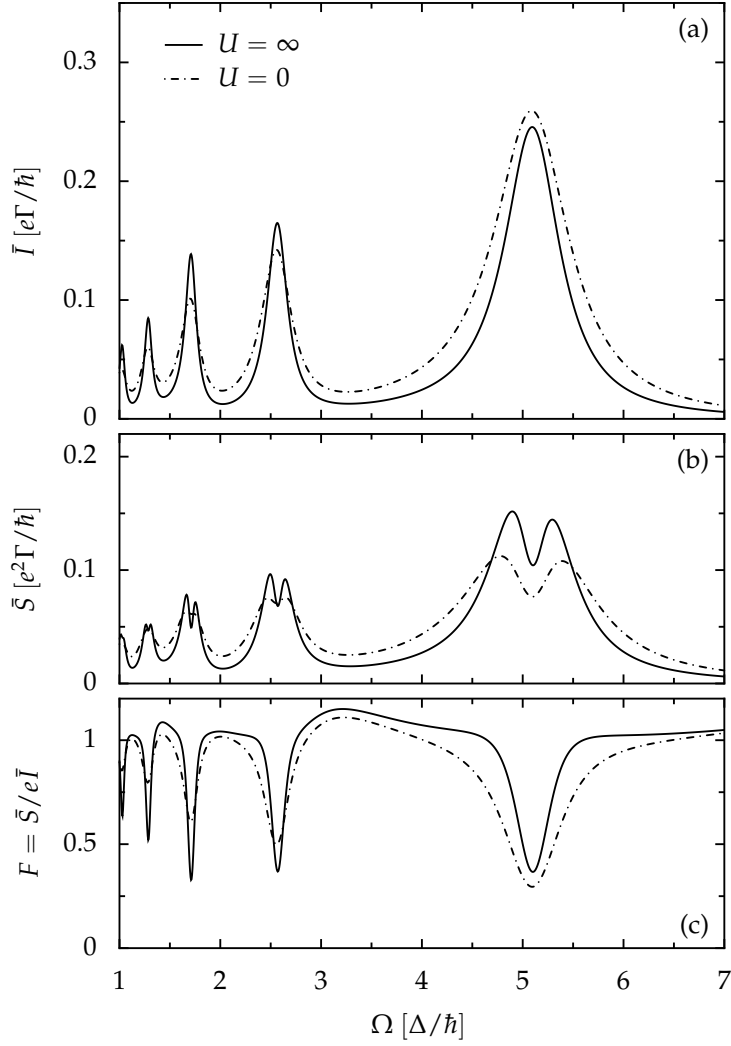


Figure 5.3: DC current (a), zero-frequency noise (b), and Fano factor (c) for the non-adiabatically driven electron pump sketched in Fig. 5.2 as a function of the driving frequency. The dot levels possess the energies  $\epsilon_{1,2} = \pm 2.5\Delta$  and are coupled to the leads with the strength  $\Gamma_{L/R} = 0.3\Delta$ . The driving amplitude  $A = 3.7\Delta$  and the temperature  $k_B T = 0.005\Delta$ . The peak at  $\Omega \approx 5\Delta/\hbar$  corresponds to the first-order resonance, while the peaks at lower frequencies are higher-order resonances.

## *5 Pump current and noise in non-adiabatically driven nanosystems*

## 6 Electron transport in junctions with energy disorder

Most quantum dot setups work at low temperatures and a common observation is a slight difference in the results after each cooling process during which possible impurities in the semiconductor freeze out near one of the dots. Then, the impurity might form an unintentional quantum dot which affects the system parameters. Moreover, the fabrication process is not perfect, one expects sample-to-sample variations in the energy levels of the dot due to slightly different quantum wells. So if all systems differ, what is the influence on the transport properties of such an ensemble? Have these fluctuations a decisive impact on the experimental accessible parameters?

Since the mentioned fluctuations are very slow, we treat them as a static disorder in the energy levels, which defines an ensemble of Hamiltonians. As a consequence, the overlap between the dot orbitals changes, leading to noticeable change in the measured current. Again, the wire is modelled by  $N$  tight-binding orbitals  $|n\rangle$ ,  $n = 1, \dots, N$ , such that

$$H_{\text{wire}} = \sum_{n=1}^N (E_n(t) + \xi_n) c_n^\dagger c_n - \Delta \sum_{n=1}^{N-1} (c_{n+1}^\dagger c_n + c_n^\dagger c_{n+1}) + \frac{U}{2} \mathcal{N}_{\text{wire}} (\mathcal{N}_{\text{wire}} - 1), \quad (6.1)$$

with the tunnel matrix element  $\Delta$  and the interaction strength  $U$ . Every onsite energy  $E_n(t)$  comprises an additional random fluctuation  $\xi_n$  that models the effects of environmental fluctuations. We assume these fluctuations to be Gaussian distributed and that they occur at large time scales, such that we can treat them as a static disorder. Thus, an interval of size  $d\xi$  around  $E_n(t) + \xi_n$  contains the onsite energy  $n$  with probability

$$w(\xi_n) = \frac{1}{\sqrt{2\pi\sigma^2}} \exp\left(-\frac{\xi_n^2}{2\sigma^2}\right). \quad (6.2)$$

Throughout this study we use a position-independent variance  $\sigma^2$ . Thus, the energy fluctuations are spatially uncorrelated, such that  $\langle \xi_n \xi_{n'} \rangle = \sigma^2 \delta_{nn'}$ . In the following analysis, the current distribution  $P(I)$  is evaluated by calculating the dc current in many realisations of the system.

## 6.1 Electron transport with slowly fluctuating energies

The first system we study is depicted in fig. 2.1 where the distribution of all wire levels is centred at energy  $E_n = 0$ . For vanishing fluctuations, an analytical solution of the current as a function of the system length has been found within a rotating-wave approximation and reads  $I_{\max} = e\Gamma/\hbar(N + 1)$ , i.e., it decays with increasing wire length [69]. A sufficiently large bias voltage is applied to the system to assure that all eigenenergies reside in the voltage window and the index “max” relates to the fact that in any case a detuning of the aligned onsite energies can only reduce the current.

The physical reason is that for equal onsite energies, solely the kinetic energy determines the eigenstates which, consequently, are delocalised. Different onsite energies, by contrast, tend to “localise” the eigenstates. This indicates that in the limit of small disorder, the current distribution  $P(I)$  possesses a clear peak at  $I = I_{\max}$  and a fast decaying tail for lower values of  $I$ .

A wire with  $N = 2$  sites represents an analytically solvable model which can serve as test case for numerical implementations. Here, we consider a two-level system with on-site energies  $\xi_{1,2}$ , i.e., with a bias  $2\eta = \xi_1 - \xi_2$ . Since the random energy shifts  $\xi_n$  are Gaussian distributed with variance  $\sigma^2$ , the bias  $2\eta$  is also Gaussian distributed but with variance  $2\sigma^2$ , i.e., its distribution function reads  $w(\eta) = \exp(-\eta^2/\sigma^2)/\sqrt{\pi\sigma^2}$ .

For the computation of the current, we restrict ourselves to the limit of a large transport voltage such that both eigenenergies of the two-level system lie within the voltage window. Then, the Fermi functions of the left and the right lead effectively become  $f_L = 1$  and  $f_R = 0$ . In this case, transport can be described within a rotating-wave approximation (RWA) which practically means that the reduced density operator of the wire is diagonal in energy representation [69]. Within RWA thus follows from the master equation (4.29) the occupation probability  $\rho_{\alpha\alpha} = w_\alpha^1/w_\alpha^2$  and, thus,  $\rho_{00} = 1 - \sum_\alpha w_\alpha^1/w_\alpha^2$ . The coefficients  $w_\alpha^n = |\langle \phi_\alpha | n \rangle|^2$  denote the overlap between the eigenstate  $|\phi_\alpha\rangle$  and the localised state  $|n\rangle$ . Inserting this solution into the current formula (4.31), we obtain  $I = e\Gamma/\hbar(1 + \sum_\alpha w_\alpha^1/w_\alpha^2)$ .

The remaining task is now to diagonalise the single-particle Hamiltonian which provides the coefficients  $w_\alpha^n$ . For bias  $2\eta$  and tunnelling matrix element  $\Delta$ , the Hamiltonian in pseudo-spin notation reads  $H = \eta\sigma_z + \Delta\sigma_x$  and possesses the eigenenergies  $\pm\delta = \pm(\eta^2 + \Delta^2)^{1/2}$ . The corresponding eigenvectors  $\phi_\alpha$  are proportional to  $(\delta + \eta, \Delta)$  and  $(\delta - \eta, \Delta)$ , respectively, such that  $w_\alpha^1/w_\alpha^2 = (\delta \pm \eta)^2/\Delta^2$ . Then we obtain for the current the expression

$$I(\eta) = \frac{e\Gamma}{\hbar} \frac{1}{3 + 4\eta^2/\Delta^2} = \frac{I_{\max}}{1 + 4\eta^2/3\Delta^2}, \quad (6.3)$$

which assumes its maximum  $I_{\max} = e\Gamma/3\hbar$  in the unbiased limit  $\eta = 0$ .

The probability distribution for the current relates to  $w(\eta)$  via

$$P(I) = \sum_i w(\eta_i) \left| \frac{d\eta_i}{dI} \right|, \quad (6.4)$$

where the summation considers all values of  $\eta$  that fulfil the condition  $I = I(\eta)$ . After some straightforward algebra, we obtain by evaluating expression (6.4) the current distribution

$$P(I) = \sqrt{\frac{3\Delta^2}{4\pi\sigma^2}} \frac{I_{\max}/I^2}{\sqrt{I_{\max}/I - 1}} \exp\left(-\frac{3\Delta^2}{4\sigma^2}(I_{\max}/I - 1)\right), \quad (6.5)$$

which is defined and normalised on the interval  $[0, I_{\max}]$ .

Figure 6.1 depicts the numerical current distribution for two different variances as well as our analytical solution for the two level system. For a small variance (a) the simulation confirms our expectation possessing the peak at  $I_{\max}$ . This strong peak vanishes for increasing wire length and a seemingly parabolic distribution emerges. A simple reasoning explains the observed behaviour: if the wire is very short, the probability that one level is detuned, i.e., out of resonance, is small; hence the overlap of orbitals is large, and so the observable current is near the maximum value. With an increasing number of sites the probability to find at least one level strongly misaligned rises and so does the number of realizations with currents considerably smaller than  $I_{\max}$ . The precise measurable value depends on the details of the system, and so we expect the probability distribution  $P(I)$  to be rather broad. Concluding this analysis, we can state that whenever the number of sites involved in transport is large, the current is extremely sensitive to even small fluctuations of the environment.

The larger the variance, the more likely becomes the scenario of detuned levels, see fig. 6.1(b). Only for short systems,  $N = 2, 3$  the peak at  $I_{\max}$  is clearly visible, while situations with highly disordered levels and consequently low conductance emerge oftener. Already for relative short systems,  $N > 3$ , the current distribution possess a clear peak at  $I = 0$ , meaning that the disorder suppresses effectively the transport. The numerical results indicate that the crossover between the isolating and conducting setting crops up if the effective disorder  $\sqrt{N}\sigma$  exceeds the tunnel matrix element  $\Delta$ .

The non-monotonic behaviour of the distribution for  $N = 2, 3$  is worth noting. It means that in real experiments two results are rather likely: either a current that is near the theoretical maximum  $I_{\max}$  and or a significantly smaller current. Our numerical simulations agree very well with the analytical solution and so we conclude that a simulation with approximately  $10^4$  different realisations of the system guarantees good convergence.

## 6.2 AC-driven disordered junctions

After the detailed study of intentionally built electron pumps in the previous chapter, we investigate the emergence of such system due to level fluctuations. Since pumping without bias voltage relies on an internal asymmetry of the system, one might ask if fluctuations of the onsite energies can create a setup suitable for pumping. We employ the model of a channel with only two sites, both

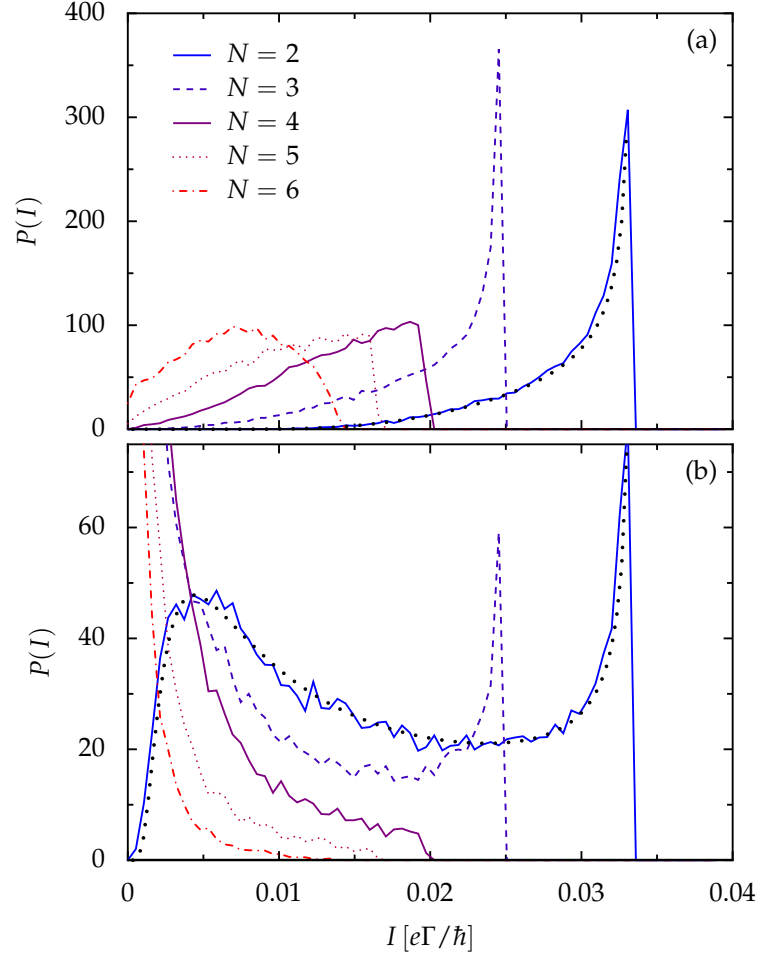


Figure 6.1: Current distribution for a channel with  $N$  sites in the limit of a large bias voltage. The standard deviation of the onsite energies is  $\sigma = 0.5\Delta$  (a) and  $\sigma = 2\Delta$  (b), while the wire-lead coupling is  $\Gamma = 0.1\Delta$ . The distributions have been obtained by computing the current for  $1.5 \times 10^4$  realizations of the wire Hamiltonian. The black dotted lines mark the analytical results for  $N = 2$  sites.

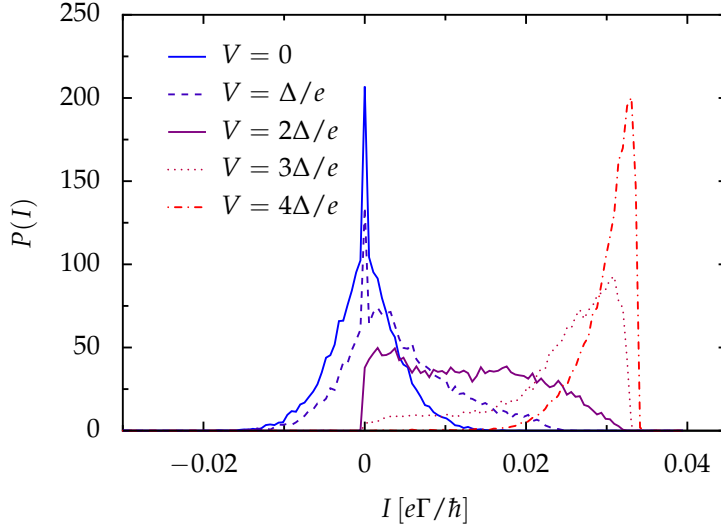


Figure 6.2: Current distribution for an AC driven wire with  $N = 2$  sites for various bias voltages. The fluctuations of the onsite energies are characterised by the standard deviation  $\sigma = 0.5 \Delta$ , the driving frequency and amplitude are  $A = \Delta$  and  $\Omega = 2 \Delta / \hbar$ , respectively. All the other parameters are as in fig. 6.1.

aligned at the Fermi levels of the leads, and add a dipole driving modelled by time-dependent onsite energies  $E_n(t) = A \cos(\Omega t - x_n \Theta)$ , again with  $\Theta = \pi/2$ . Since we want to investigate possible pumping effects, we tune the driving frequency  $\Omega = 2\Delta/\hbar$  such that it matches the average splitting of the eigenenergies, and set the amplitude  $A = \Delta$  to an intermediate strength. In order to characterise the influence of the fluctuations on the pump current, an extra bias voltage will be applied.

The solid line in fig. 6.2 shows the current distribution in the absence of a bias voltage,  $V = 0$ . The symmetry of the system is reflected in the symmetric current distribution around  $I = 0$  and so its ensemble average vanishes, as expected for a completely symmetric setup. Note that a single realization of the wire does not possess this reflection symmetry due to the spatially uncorrelated fluctuations and thus pump currents in one or the other direction can occur. Quantitatively, the pump current observed for intermediate amplitude and nearly resonant driving is in the order of 10–20 % of the maximal current in the high bias limit [57]. The strong peak at  $I = 0$  stems from numerous realizations where the driving is well out of resonance and thus cannot induce pump currents.

When a bias voltage  $V > 0$  is applied to the system the spatial symmetry is effectively broken and the current distribution is displaced towards positive values, see fig. 6.2. For small bias voltages  $V \lesssim \Delta/e$ , non-adiabatic pumping against the

voltage gradient is still possible, but surprisingly the peak at  $I = 0$  remains clearly visible. It corresponds to situations, where first the driving is far out of resonance and therefore cannot induce pump currents, and second the energy splitting of the levels is so large that both levels lie outside the voltage window. By increasing the bias voltage, the second situation becomes less and less likely. For even larger voltages one would expect a current distribution similar to the situation of a two level system in the absence of driving, since the bias dominates the system. Indeed, for  $V \approx 4\Delta/e$  the distribution already assumes a form hardly distinguishable from the results of the undriven two level system shown in fig. 6.1(a).

### Conclusion

We have investigated the current through a coupled quantum dot system with disordered onsite energies. Such a disorder can stem from the interaction with slow fluctuations of background charges in the substrate or randomly formed quantum dots. We studied the resulting current distributions of two typical cases, namely an “open transport channel” and a driven double dot for which random energy shifts break reflection symmetry and, thus, the driving can induce a ratchet current.

The open transport channel is characterised by tight-binding levels with equal onsite energies, such that any misalignment stems from the disorder. As soon as the standard deviation of the onsite energies exceeds the tunnel matrix elements, the current distribution no longer exhibits peaks only at a finite value, but also at zero. For longer wires, the peaks at finite values vanish completely. The emerging isolating behaviour is similar to Anderson localisation in one-dimensional disordered lattices [70]. Note however that we consider relatively small systems that are not in the scaling limit in which Anderson localisation is usually studied.

For the case of the driven double quantum dot, the fluctuations break effectively the reflection symmetry. Consequently, an external driving can induce pump currents in both directions and the resulting current distribution is symmetric. If the random energy shifts render the driving strongly off-resonant, the induced pump current is rather small, which we found in many realisations leading to a distinct spike at zero current in the distribution. From the influence of a bias voltage on the current distribution, we can conclude that pumping becomes impossible, whenever the energy levels lie well within the voltage window.

Our results point at a strong influence of slow fluctuations or a static disorder on the maximal obtainable current. In various situations, already the presence of small deviations from the ideal setup might lead to a significant change in the conductivity of the system. This offers a possible explanation of the huge sample-to-sample fluctuations in currents through molecular wires.



## 7 Pump currents induced by propagating waves

A technique recently adopted to drive quantum dot systems is based on nano-earthquakes propagating in the system. Surface acoustic waves (SAW) can be used to shake quantum dots and caused quite a stir in semiconductor physics [71]. Apart from their applicability as wavelength sensors in today's cell phones and as a tool for lab-on-a-chip devices [72], they are used to stimulate and manipulate electronic processes in nano structures. Recently, SAWs as driving forces for quantum systems have been experimentally implemented [73, 74].

Differently to electromagnetic waves, a SAW is a propagating wave. While the imagination of such a wave is easily possible, the quantum mechanical treatment we want to employ renders the understanding of the physical effects inside the system rather difficult.

SAWs are launched on semiconductor structures using the piezo-electric effect, in combination with an applied oscillating voltage at a structure called inter digital transducer (IDT). The IDTs have a comb-like structure and are etched on the piezo-electric substrate. Since the wavelength depends on the distance of the fingers, there is the drawback that an IDT can only create SAWs of that specific wavelength. By applying an oscillating voltage with a phase shift of  $\pi$  between the IDTs, one induces a contraction of the piezo-electric substrate, which leads to the launch of a SAW in both directions perpendicular to the fingers. The propagating wave is similar to waves observed in earthquakes, since most of its energy is transported at the surface while its velocity is the speed of sound of the bulk material, for example in GaAs  $v_{\text{sound}} \approx 2885 \text{ m/s}$ .

The fundamental difference to quantum dot setups driven by microwaves is that SAWs do not allow one to control the phase relation directly. In a SAW driven system, both wavelength and driving frequency are determined by the transducers and the sound velocity. Since the distance between neighbouring dots is fixed, phase lags between the sites are caused by the setup and cannot be altered.

Recent experiments demonstrate the possibility of creating pump currents induced by surface acoustic waves [73]. The theoretical treatment focusses mainly on the adiabatic situation [75], although there has been recent attempts to study also the non-adiabatic limit [76].

Motivated by recent experiments at the chair of Experimental Physics I here in Augsburg (see ref. [77] and appendix B), we apply our Floquet formalism to SAW-driven quantum dots. As a starting point, we compared measured Coulomb diamonds with the undriven sample to our theoretical study. We extracted the hop-

## 7 Pump currents induced by propagating waves

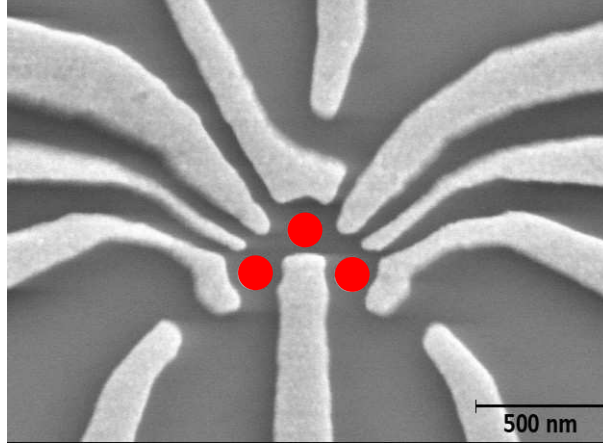


Figure 7.1: STM-picture of a triple quantum dot. The positions of the QDs are indicated by the three red circles [78].

ping matrix element  $\Delta = 0.33$  meV [77] to obtain the corresponding frequency of the SAW  $\Omega \approx 0.005 \Delta/\hbar$ . Since the driving frequency is very small compared to other system energies, it indicates an adiabatic regime in the experiment. However, our Floquet approach is most efficient for non-adiabatic driving fields, and as a consequence of this, the numerical treatment of a SAW-driven system is a challenge. A more suitable candidate to take full advantage of the Floquet approach is a system of microwave-driven quantum dots, which we will address in the upcoming studies.

In recent years, the creation of serial double and triple quantum dots has become more and more a standard technique in semiconductor physics. There are attempts to build systems with the possibility to adjust freely the phase difference between the dots [78], but a big issue remains the non-perfect control of each dot: By applying a gate voltage to one dot, the energy levels inside can be well controlled, but the jamming of the other dots by the induced electric field remains a problem. So, it is not sufficient to shift the gate voltages of each dot, one furthermore has to develop a correction algorithm that cancels out the unwanted effects by the surrounding gates. Progress has been made on this issue, such that the triple quantum dot shown in fig. 7.1 will be fully controllable soon. Hence, our theoretical predictions should be observable in the near future.

To gain a qualitative understanding of the physical processes in such systems, we analyse two simple models, a symmetric two level system without voltage bias and degenerate on-site levels and the respective three site model. Already in these reduced models, we will uncover interesting transport properties.

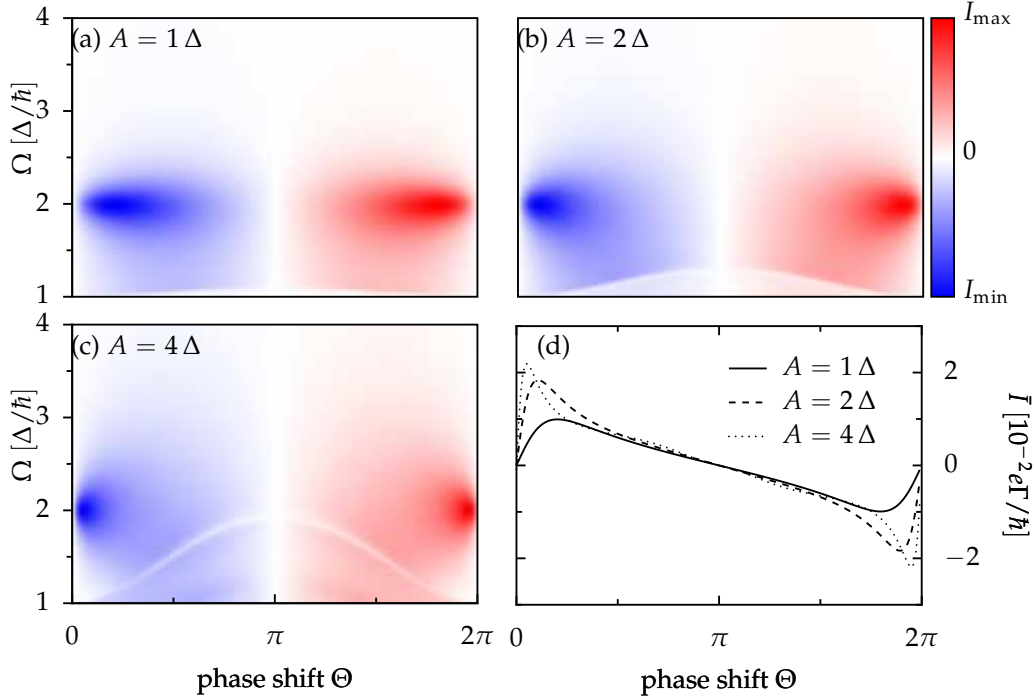


Figure 7.2: Average current through a degenerate two level system as a function of phase shift  $\Theta$  and driving frequency  $\Omega$ . The white regions mark areas where the net current is zero, while red (blue) regions indicate a net transport to the left (right). The corresponding amplitude  $A = 4\Delta$  and the coupling  $\Gamma = 0.3\Delta$ .

## 7.1 Degenerate two-level system

We again employ the model shown in fig. 2.1, but now allow for an arbitrary phase lag  $\Theta$  between the time-dependent energies of the two sites. The lack of any bias voltage, the equal coupling to the respective leads and the degeneracy of the on-site energies lead to a highly symmetric system. A driving force that results in a phase shift between the two levels might induce directed currents in the system for certain values of  $\Theta$ . In the case of non-interacting electrons, the system obeys particle-hole symmetry which has the consequence that the current vanishes. The situation changes dramatically, if an interaction between the electrons comes into play.

The Coulomb interaction breaks effectively the electron-hole symmetry and so the generalised parity. The net current for different driving amplitudes  $A$ , depicted in fig. 7.2(a), (b) and (c) shows a symmetric behaviour around a phase shift  $\Theta = \pi$ , with a maximum for small values of  $\Theta$ . For resonant driving,  $\Omega = 2\Delta/\hbar$ , the current is maximal, while it decreases fast with increasing gap to the resonance. The obvious reason for the  $\Omega$ -dependence lies in the fact that at the resonance the

## 7 Pump currents induced by propagating waves

energy provided by the driving field matches exactly the difference of the eigenenergies and so the necessary transition of an electron from one eigenstate to the other is most likely. Vice versa, a driving force that is off-resonant, results in only a small transition probability between the states. This shows that resonant driving is again most efficient and results in more pronounced current peaks, while off-resonant driving is less effective.

The white seemingly sinusoidal line in the lower parts of fig. 7.2(a)-(c) is monotonically increasing with the driving amplitude  $A$ . The reason for this suppression of the current at certain values of  $\Omega$  and  $\Theta$  might be similar to coherent destruction of tunnelling [79], where the effective overlap between the states is nearly zero and so the current vanishes. One finds a similar Bessel function dominated behaviour of the eigenenergies within a perturbational approach, see appendix A.

If we plot the current as a function of  $\Theta$  for different amplitudes  $A$ , as shown in figure 7.2(d), a clearly non-monotonic behaviour can be observed. Starting from zero phase shift, the current increases strongly and is peaked at  $\Theta \approx 0.03 \pi$ . The explanation of this surprising behaviour relies on two observations. First, the overlap needed for transport among the levels is maximal, if the phase lag is rather small, and so would favour a very small detuning. But if  $\Theta$  is small, only a little current occurs, because the system is still rather symmetric. Note that for  $\Theta = 0$ , the driving corresponds to an ac gating which cannot induce a pump current [45]. The vanishing current at  $\Theta = \pi$  is a direct consequence of the emerging generalised parity that the system obeys in this case, as well as for situations where both levels oscillating in phase  $\Theta = 0, 2\pi$ . The antisymmetry of the induced current,  $I(-\Theta) = -I(\Theta)$ , stems from the total spatial symmetry of the cosine-shaped driving. Remarkably, the current is amplitude-independent over a wide range of phase shifts, centred around  $\Theta = \pi$ , which is reflected by the eigenenergies calculated within a perturbational approach (appendix. A).

### 7.2 Current reversals in an open transport channel with three sites

The second system we discuss in this chapter is the degenerate three level system. Basically, the only difference is an added third level with the same on-site energies as the two others. The average current through the system as a function of frequency and phase is depicted in fig. 7.3. For non-interacting electrons the results are identical to the two level system, the current vanishes for all phase differences and frequencies (not shown). The reason is again the generalised parity together with the electron-hole symmetry.

As before, Coulomb interaction breaks the particle-hole symmetry such that a current emerges. It is symmetric with respect to  $\Theta = \pi$  and, moreover, it exhibits some interesting current reversals, depicted in fig. 7.4(a). We observe several changes in the current direction, not only as a function of  $\Theta$  as before, but also upon changing the frequency  $\Omega$ .

## 7.2 Current reversals in an open transport channel with three sites

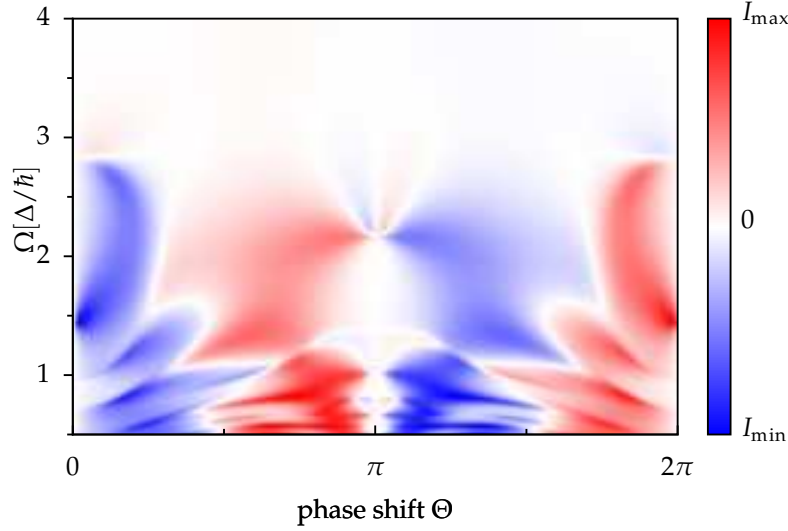


Figure 7.3: Average current through a degenerate three level system as a function of phase shift  $\Theta$  and driving frequency  $\Omega$ . The white regions mark areas where the net current is zero, while red (blue) regions indicate a net transport to the left (right).

The symmetry around the point  $\Theta = \pi$  has been elaborated before, so we concentrate on the non-monotonic behaviour between 0 and  $\pi$ . The results demonstrate that a current switching is possible, solely by changing the phase relation between the levels of the system. Moreover, for weaker driving,  $\Omega = \Delta/\hbar$ , the current shows a plateau-like structure with a sudden change in direction at  $\Theta \approx 0.7\pi$ , while for the more powerful field  $\Omega = 2\Delta/\hbar$ , the current has a smoother shape.

Focussing on the  $\Theta$ -dependence of the current, we note that there are mainly two values  $\Theta = 0.4\pi, 0.9\pi$  for which the current changes its sign several times with increasing frequency  $\Omega$ , shown in detail in fig. 7.4(b). The current for  $\Theta = 0.4\pi$  oscillates and decreases with increasing  $\Omega$ . Already for  $\Omega = 3\Delta/\hbar$ , the current reaches its minimum and remains zero also for higher driving frequencies. The greater phase shift of  $\Theta = 0.9\pi$  creates a significantly different current-frequency dependence, suppressing mostly the current reversal observed before. However, the current approaches zero for roughly the same driving frequency. Further, we observe for slow driving frequencies near the adiabatic regime  $\Omega \ll \Delta/\hbar$  an erratic behaviour of the current, indicating that the physics in this intermediate region may be rather involved.

## Conclusion

For both the degenerate two-level system and the open transport channel, pump currents require an electron-electron interaction. It breaks effectively the electron-

## 7 Pump currents induced by propagating waves

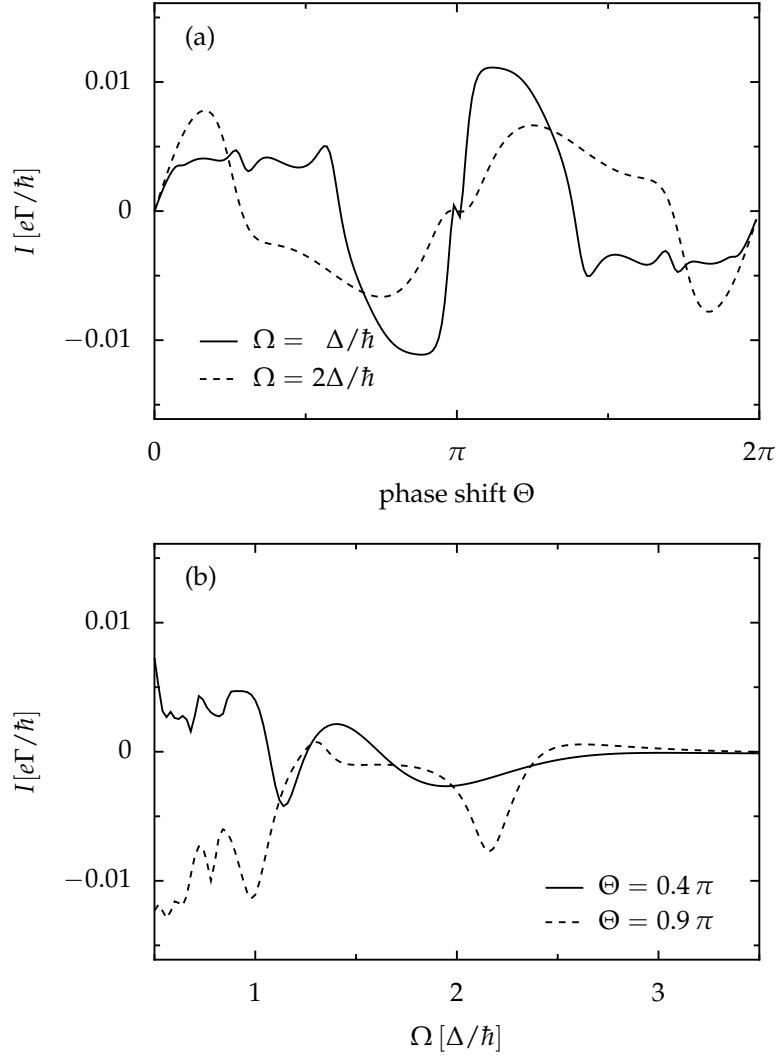


Figure 7.4: Average current through a degenerate three level system as a function of (a) the phase shift  $\Theta$  for two different driving energies  $\Omega$  and (b) the driving frequency  $\Omega$  for two different phase shifts. The amplitude  $A = 4\Delta$  and the symmetric coupling  $\Gamma = 0.3\Delta$ .

## 7.2 Current reversals in an open transport channel with three sites

hole symmetry and thus generalised parity, which renders pumping possible.

This pumping occurs in a perfectly symmetric system in which the symmetry is broken by the propagation direction of the wave. Interestingly enough, the current can nevertheless flow into both directions, and the direction may change upon changing the driving frequency or the phase shift.

As is expected for non-adiabatic pumps, the transport mechanism is most efficient, if the driving is in resonance with the internal level splitting. The direction of the current can be controlled by changing the phase shift between the levels. While an increased phase shift reduces the symmetry, leading to more effective pumping, at the same time, the reduced overlap of the levels favours smaller currents. The combination of these effects leads to the observed non-monotonic behaviour of the current.

Surprisingly, the current in the two-level system is amplitude-independent for a wide range of phase shifts, centred around  $\pi$ . If the delay between the levels is small, the maximum current can be observed, now scaling with the amplitude.

By studying a degenerate three level system, we could show that again a Coulomb repulsion is necessary to induce transport. Moreover, our numerical study demonstrates that a current reversals (for certain fixed phase locks) become possible by changing the frequency.

Although the predicted frequency and amplitude dependence resembles the one observed experimentally [80], we like to emphasise that these results are found in very different frequency regimes. Thus, the experimentally observed current reversals remain unexplained.

## *7 Pump currents induced by propagating waves*



## 8 Photo induced ballistic electron transport

Hu proposed in 1993 [81] that photon-assisted tunnelling [82] should be also observable in quantum point contacts or electron waveguides. Hence, the photoreponse of semiconductor quantum wires has been studied comprehensively in the last decade [83–85].

Inspired by ongoing experiments in the Holleitner group in Munich [20–22], we address the similar situation of photo induced ballistic electron transport. In the experiment, a laser pulse is used to create a bunch of excited electrons in an Al-GaAs/GaAs heterostructure. On the structure, a geometrical constraint is etched which acts as a potential wall for the electrons and confines their movement within a certain region. Due to the large system size in the order of several  $\mu\text{m}$ , the electrons move freely within the potential well and are not restricted to occupy isolated tight-binding levels.

The measurements are performed on a two-dimensional electron gas (2DEG) under the surface of the semiconductor heterostructure. By etching and lithographic techniques one obtains the structure depicted in fig. 8.1. The edges serve as boundaries for the electron trajectories and in order to perform measurements and to control the 2DEG top gate electrodes are installed, shown in gold. We will investigate the cutout marked by the black rectangle in fig. 8.1. For a better insight, fig. 8.2 shows a detailed sketch rotated by 45 degree counter-clockwise, including all relevant dimensions.

A small bias voltage is applied between the source and the quantum point contact (QPC), which serves as a detector for the photocurrent. Effectively, the QPC counts the number of electrons passing through the gap between the two circles on the left. To create excited electrons, a laser with  $\lambda = 800\text{ nm}$  is used and the sample is scanned with a resolution of  $1\ \mu\text{m}$  in the bright gray area between the circles on the right and in the channel on the left side, shown in fig. 8.2. After every pulse – creating approximately  $3 \times 10^4$  electrons in the conduction band [23] – the induced current from source to drain is measured. Consecutively performing this, one obtains a current map, where the brightness indicates the current, depending on the position of the excitation. To simplify our investigation, we split the problem in two independent parts. First, we analyse the current distribution on the right side of the QPC (“circles”) and second for the left side (“channel”), see fig. 8.2.

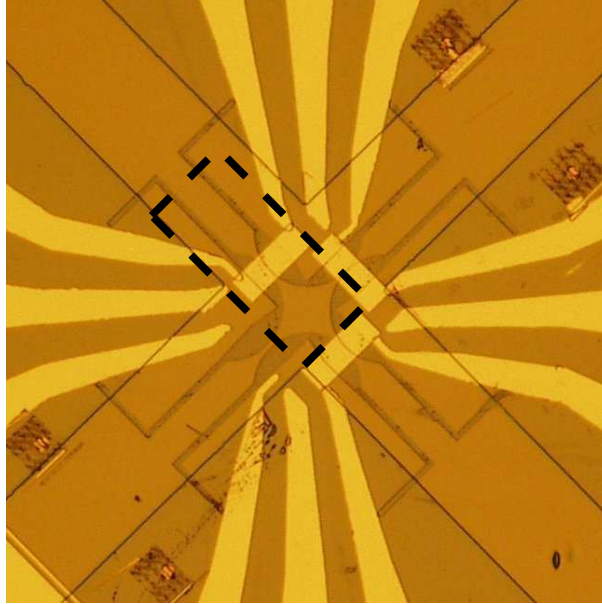


Figure 8.1: Picture of the etched sample geometry [23]. The finger-like structure in gold depicts the top-gates to control the 2DEG below the surface. The measurements were performed scanning with a laser the area inside the black rectangle.

## 8.1 Modelling

The energy of the laser (1.55 eV) is so large that excited electrons can overcome the bandgap of 1.52 eV and reach the conduction band. There the electrons move like free non-interacting particles and are reflected elastically by the potential steps at the circle boundaries [86–90]. For the current measurements a small bias voltage between source and drain is needed and the corresponding voltage drop occurs at the contact sites of source and drain, such that the electric field induced by this potential difference can be neglected and the electrons can move without the influence of the electric field inside the 2DEG. The life time of the excited states is limited by relaxation processes, e.g., phonon scattering that absorbs momentum and energy.

In the experiment, the sample material is specified with a mean free path  $\lambda = 15.1 \mu\text{m}$ , which is half the system size, with the mean free path  $\lambda$  being the distance at which the probability that an electron scatters is  $1/e$ . Since it is not influenced directly by the measurement and etching process, we assume it to be constant throughout our calculations. To take the scattering probability into account, an electron hitting the detector counts with a weight factor, depending on its path length inside the constraints. Since the probability of an interaction depends exponentially on the distance  $x$ , our weight factor reads  $e^{-x/\lambda}$ , with the path length  $x$ .

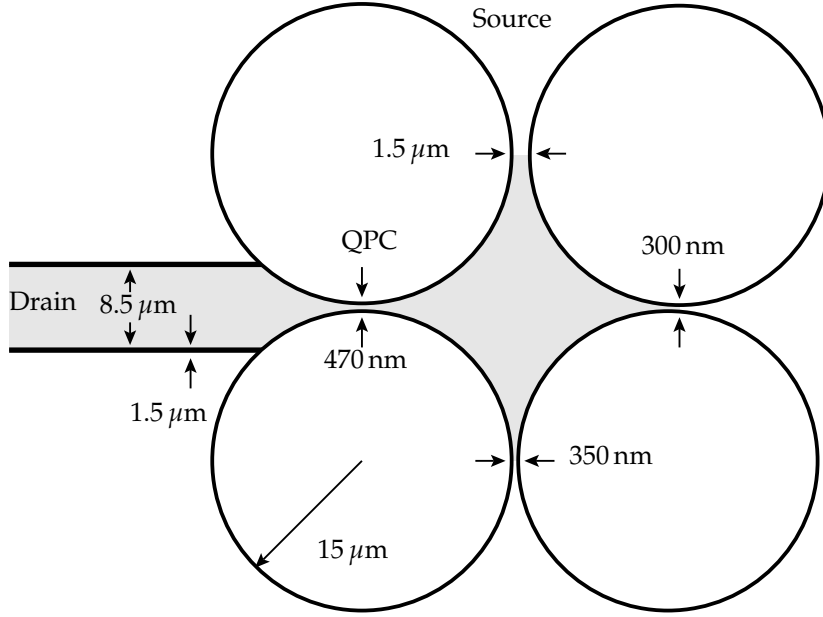


Figure 8.2: Geometry of the sample. All circles have the same radius, and will serve as hard boundaries for the electrons. In the experiment the laser scans the gray area, and at every point the induced photocurrent is measured. The gap between the circles differ from 300 nm up to 1500 nm and a voltage is applied between source and drain.

The approximation of a free electron is in general only justified, if the system size is comparable or smaller than the free mean path [86], which is not assured in our system. But the experimental results can be explained in terms of free electrons, so we restrict ourselves to the most simple model containing the observed effects.

Another possibility for the particles to relax is an interaction with a boundary. To model this, we use the approximation of an energy- and momentum-independent absorption rate, which is reflected in our model by the parameter  $a$ , the absorption probability at every reflection at a boundary: Every time the electron encounters a sudden drop in the potential, i.e., an etched boundary, the probability that it is counted is reduced by  $a$ . For a perfect billiard,  $a$  would be 0, i.e., all reflections are elastic. The other limit  $a = 1$  describes the situation, in which an electron is always absorbed if it scatters at a boundary.

The second parameter in our numerics is the depletion length  $l$ , stemming from the etching process and the depletion around the structure when applying a potential. It is very difficult to determine the above stated parameters in the probe, so we will compare the influence of different values of the parameters on the results. In the numerics, the depletion length is added to the radius of the circles as well as to the thickness of the channel boundaries on the left side of fig. 8.2.

We simulate  $10^4$  electrons at every starting point with arbitrary direction of their

momentum to obtain the profile of the detection probability. Note that we will use the terms arrival probability and detection probability synonymously. In the complete chapter the colour coding will be as follows: The highest arrival probability of an electron at the detector is depicted in dark blue, while white means that at this starting point the probability for an electron to be counted at the detector is zero. The theoretical probability of arrival can be linked to the physical quantity current by multiplying it with the number of total electrons created per laser pulse.

## 8.2 Circle-shaped constriction

### Perfectly absorbing walls

In order to get an intuitive picture of the physics at work, we first investigate the case of an absorption probability  $a = 1$ . So an electron that scatters at one of the boundaries is absorbed and does not contribute anymore to the current. This is of course overestimating the absorption probability way to high, but has the advantage of being analytically solvable. This situation is shown in figure 8.3 for two different depletion lengths. The colour coding is as defined, so the more intensive the blue, the more likely it is for an electron starting from that point to arrive at the detector. Note that the maximum saturation of the colour is set to a point  $5 \mu\text{m}$  away of the detector to model the coverage of the top gate. On the left side of fig. 8.3 the depletion length  $l$  is zero while on the right side  $l = 200 \text{ nm}$ .

First, we analyse the results for vanishing depletion length  $l = 0$ , which means that directly at the etched curbs of the structure the potential drops suddenly. We observe several effects in the false-colour-plot in fig. 8.3(a): first, the very small blue area near the detector and the fast fading of the colour indicates that the probability of an electron to travel through the system and hit the detector decreases rapidly. The reason for this is the exponential decaying weight of an electron, e.g., an electron starting in the middle of all four circles counts at maximum  $1/e$ , if it is not already absorbed by the boundaries before. The second observation is the strict distinction between areas where a photocurrent can be induced by the laser and areas where this is impossible.

To get a better insight, we cut the false colour plot parallel to the  $y$ -axis at  $x = 15.25 \mu\text{m}$ , see fig. 8.3(b), and also parallel to the  $x$ -axis at  $y = 15.25 \mu\text{m}$ , see fig. 8.3(c). The probability distribution in fig. 8.3(b) demonstrates that for starting positions without a straight connection to the detector ( $y < 12 \mu\text{m}$  and  $y > 18 \mu\text{m}$ ), the detection probability is zero. For the other starting points, the arrival probability decreases symmetrically around the centre position of the detector at  $y = 15,235 \mu\text{m}$ , which can be understood in a simple geometric manner: directly at the height of the detector the fraction of electrons that can hit the detector is maximum, while for remote positions, the aperture angle decreases and so does the electron number.

## 8.2 Circle-shaped constriction

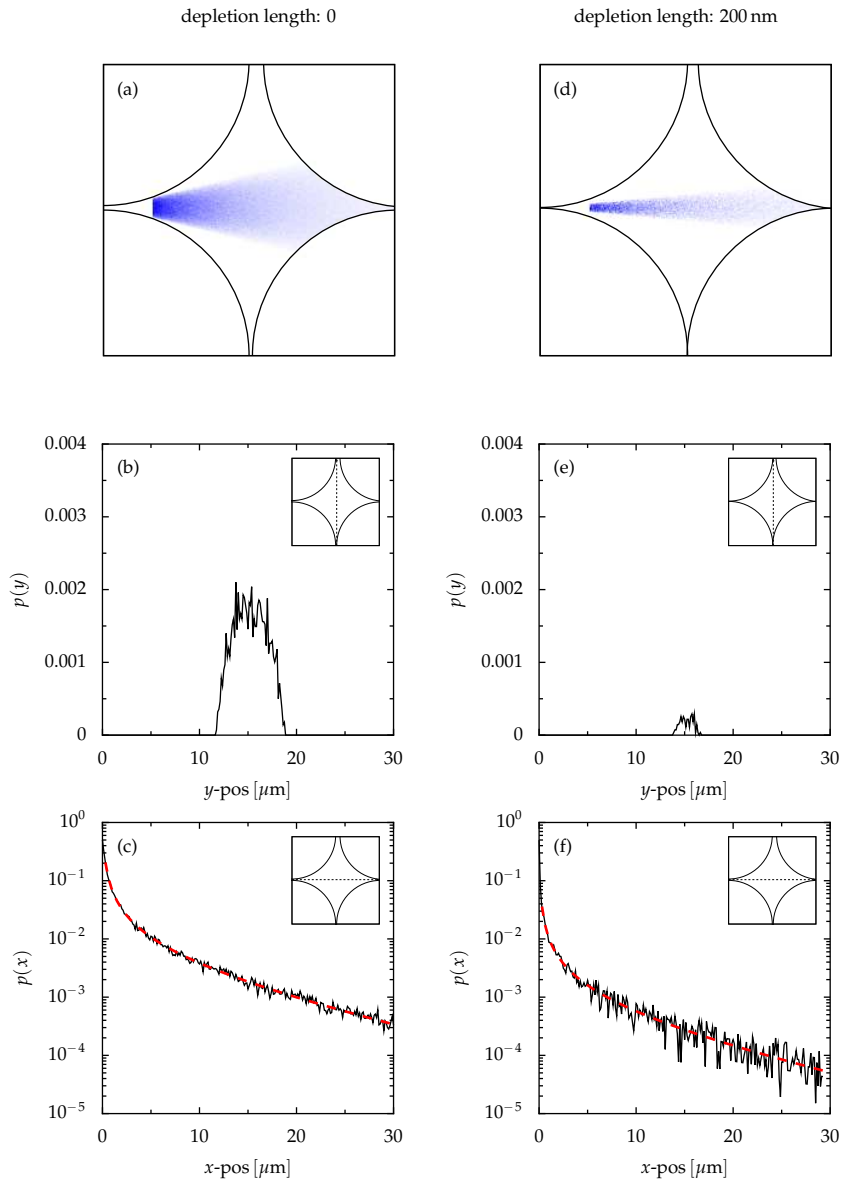


Figure 8.3: In the upper line, the current plots for different depletion lengths  $l$  and perfectly absorbing walls are shown. The centre line shows the probability distribution for fixed  $x = 15.25 \mu\text{m}$ , i.e., parallel to the  $y$ -axis. In the last line the corresponding cut parallel to the  $x$ -axis ( $y = 15.25 \mu\text{m}$ ) is shown.

## 8 Photo induced ballistic electron transport

If we focus on the probability distribution along the  $x$ -axis at the height of the detector, fig. 8.3(c), we observe the expected path-dependent exponential decay stemming from the weight of electrons. Near the detector, we notice a strong deviation from the exponential shape. There are two effects important to explain the observations: on the one hand the increasing distance and so the decreasing weight of the electrons, which should lead to an exponential decay. On the other hand, the decreasing fraction of electrons that can be detected directly. The maximum probability of an electron to be counted is  $1/2$ , since at a point very close to the detector, all electrons whose momentum vector points to the left are counted, and the other half with momentum to the right is lost. An analytical approach would now take into account the way and the percentage of electrons that can be detected. Remember that we investigate the behaviour for a fixed height on the  $y$ -axis. Therefore, we approximate the detection probability  $p(x)$  of an electron with

$$p(x) = \frac{1}{\pi} \frac{\arctan(0.47 \mu\text{m} - l)}{2x} e^{-x/\lambda}. \quad (8.1)$$

The first factor is determined by the geometry: The direction of the momentum of an electron is randomly distributed between  $0$  and  $2\pi$ , thus, the probability to hit the detector is determined by the angle for which the detector can be reached, divided by  $2\pi$ . The second contribution models the path dependent weight of the electron. The small deviation from this simple model stemming from the not perpendicular incoming electrons is negligible, as we see in the very good agreement between the numerical simulation and the analytical solution (dashed line in fig. 8.3(c)).

For the case of a large depletion length  $l$ , see false-colour-plot in fig. 8.3(d), the tail of the probability distribution is much narrower compared to (a), which is a direct result of the increased circle radii and the therefore narrower detector.

If we consider the cut parallel to the  $y$ -axis, depicted in fig. 8.3(e), the maximum is centred at the same position as in (b), but the value is remarkably smaller by a factor of  $5 - 7$ . This is expected since the width of the detector shrinks from before  $470 \text{ nm}$  ( $l = 0$ ) to now  $70 \text{ nm}$  and so does the probability for an electron to arrive directly at the detector.

The decay of the detection probability with increasing distance from the detector is shown in fig. 8.3(f). The argument of the path dependence and the reducing fraction of transmitted electrons outlined above is still valid in this situation and so eq. (8.1) holds true for  $l = 200 \text{ nm}$ , which is shown by the dashed line. The noticeably higher fluctuations around the analytical solution stem from the poorer numerical convergence, a larger number of simulated trajectories would erase this.

### Perfectly reflecting walls

After the case of perfectly absorbing walls, we now address the other extreme, namely perfectly reflecting walls. To ease our numerical treatment, we limit the number of bounces at the edges to 15, since paths with more bounces are already sufficiently suppressed by the path dependent weight, leading only to a small error in the numerics.

Compared to the case discussed above, we expect a more homogeneous distribution without a sharp edge in the probability map, since the curbs reflect the electrons, increasing their probability of detection. As before, we begin our analysis with the case of vanishing depletion length  $l = 0$ . The simulation depicted in fig. 8.4(a) reproduces our expectations: we see a strong influence of directly detected electrons but notice also the lack of sharp edges as well as the increased blue area.

To get a better insight, we will cut again the false colour plot parallel to the  $y$ -axis at  $x = 15.25 \mu\text{m}$ , see fig. 8.4(b), and compare the results to the case of perfectly absorbing wall, cf. fig. 8.3(b). Although the maximum probability is situated at the same position at the centre of the detector, the absolute value is increased by a factor of 4 – 5. Also, the probability declines not to zero, but shows a slowly decaying behaviour. The reflection of electrons from the boundaries permits a large number of new trajectories, leading to an increased arrival probability at the detector starting from any point.

More interesting is the cut along the  $x$ -axis shown in fig. 8.4(c). With increasing distance to the detector, the feasibility decreases again exponentially, but with the possibility of reflection, it saturates to a roughly constant value two order of magnitude larger as for perfectly absorbing walls. An explanation for this saturation might be an effect similar to focussing. An electron that is created at the very right side of the structure, can either leave it to the right or it is reflected by the circles and so approaches the detector. Since this situation of being reflected towards the detector to the left is rather likely in the small gap between the two circles on the right side, this intercepts the decreasing weight of the electrons and leads to the observed saturation.

For the situation of large depletion length  $l$ , the false colour plot and the cut parallel to the  $y$ -axis are shown in fig. 8.4(d) and (e) respectively, the above outlined reasoning applies as well. The contrast between regions with large probability and such with very low one is again reduced compared to absorbing walls, fig. 8.3(a), but narrower as for zero depletion length fig. 8.4(a). The  $y$ -dependent arrival probability is reduced by a factor of 5 – 8 and shows the slowly decaying tails, but this time at a very low niveau.

However, the cut parallel to the  $x$ -axis, fig. 8.4(f), shows a remarkable feature: The detection probability increases for larger distances to the detector! This counter-intuitive effect can be deduced from the explanation of the saturation in fig. 8.4(c). To understand the observations it is convenient to remember the exact geometry of the structure, compare fig. 8.2. If the depletion length exceeds  $l = 150 \text{ nm}$  the

## 8 Photo induced ballistic electron transport

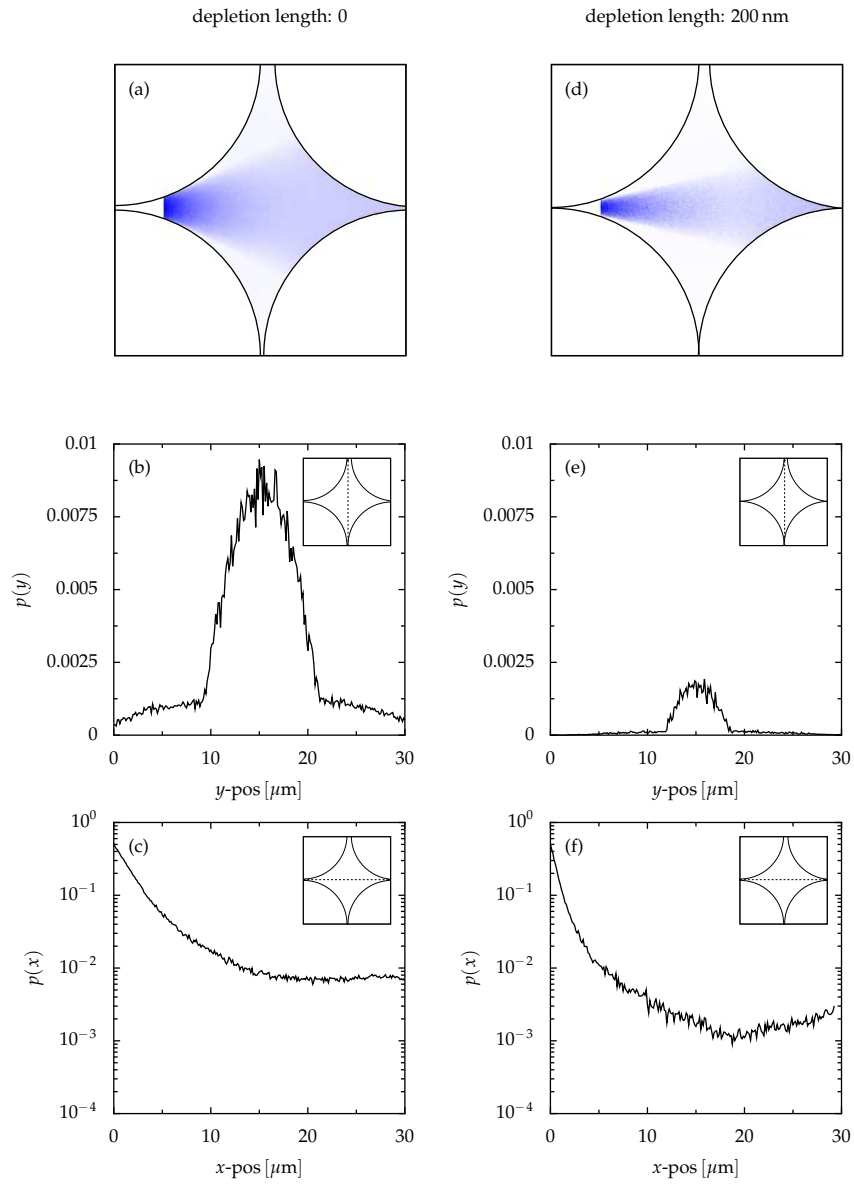


Figure 8.4: In the upper line, the current plots for different depletion lengths  $l$  and perfectly reflecting walls are shown. The centre line shows the probability distribution for fixed  $x = 15.25 \mu\text{m}$ , i.e., parallel to the  $y$ -axis. In the last line the corresponding cut parallel to the  $x$ -axis ( $y = 15.25 \mu\text{m}$ ) is shown.



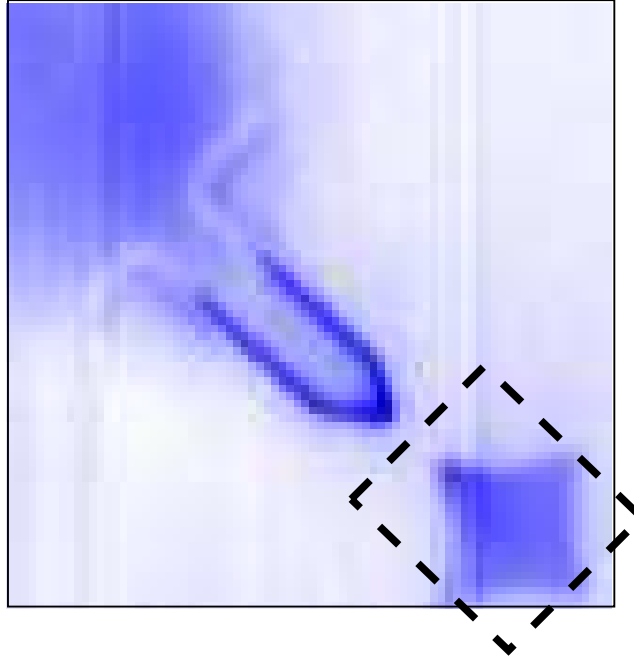


Figure 8.5: Current for every illumination point of the sample in fig. 8.1, scanned area  $80 \times 80 \mu\text{m}$ . Blue areas mark a high current, while white denotes no current. Note that the region investigated is indicated by the black rectangle in the lower right corner. The tuning-fork shaped blue structure in the centre of the image stems from side-effects of the measurement.

gap on the right side of the structure is effectively closed, thus electrons cannot escape anymore. This enclosure of the electrons leads to the observed increase, while at the same time the detector size decreases and therefore the absolute value is smaller. If  $l > 175 \text{ nm}$ , also the gap between the two lower circles is closed. Furthermore, the probability to arrive drops to exactly zero at  $x \approx 30 \mu\text{m}$ , which stems from the increased radius of the circle in the lower right corner.

### Comparison with experimental data

In order to check our numerical model for the excited electrons, we compare the results with real experimental data. In the false-colour-plot, see fig. 8.5 [23], the region of interest is indicated by the black rectangle. Every pixel represents an area of  $1 \mu\text{m}^2$  reflecting the laser step width scanning the probe. For every position, the corresponding current is measured with the QPC.

At first glance, it is obvious that our numerical simulations for both the perfectly absorbing walls as well as the perfectly reflecting walls are not sufficient to describe the trend measured in the experiment along the  $y$ -axis. The numerics

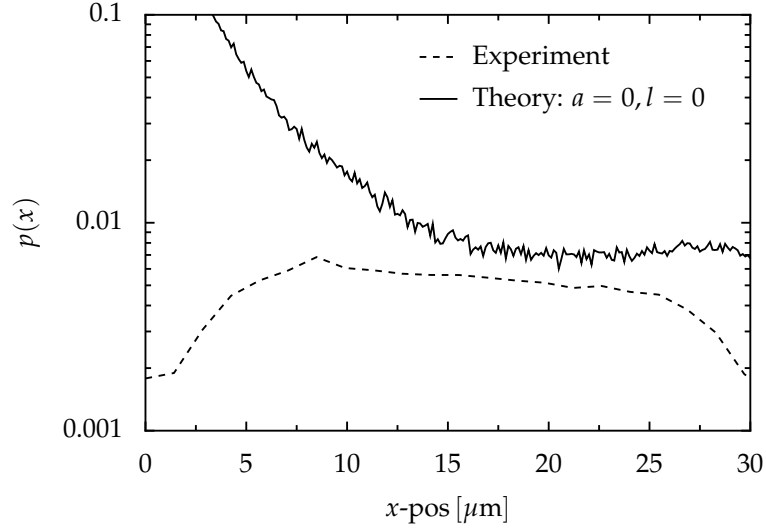


Figure 8.6: Cut along the diagonal from the upper left to the lower right corner of fig. 8.5, starting at the QPC. Within the first  $10 \mu\text{m}$ , the current is heavily affected by the nearby QPC, thus one must not compare both curves. The same holds true for  $x > 27 \mu\text{m}$ , where the close-by circle boundaries can be populated by charge carries [22]. Note the logarithmic scale on the  $y$ -axis.

indicate that a very strong decay of the current should be observable once one moves away from the symmetry axis at  $x = 15.235 \mu\text{m}$ . Already the false-colour plots in fig. 8.3(a) and (d) contradict the measurements. Although we notice that the results for vanishing absorption probability  $a = 0$  model the experimental data better. Nevertheless, the model is not suitable to describe the physics near the QPC or the boundaries.

If we focus on the current decay along the  $x$ -axis, a detailed plot is depicted in fig. 8.6. The increase in the first  $10 \mu\text{m}$  stems from the detector, because the close vicinity of the QPC to the illuminated spot, and the consequent complex dynamics renders our classical treatment inappropriate. The significant drop in the curve for  $x > 27 \mu\text{m}$  has its origin in the nearby etched curbs, where possibly the increased electric fields separate the optically induced electron hole pairs [22].

The comparison of the measured current decay with the simulation for vanishing depletion length  $l$  and perfectly reflecting walls shows a good agreement. The deviation for very small and very large values of  $x$  have been explained before with the special experimental setup. For the inner region, we observe an excellent match of the results, the numerics reproduce well the saturation of the photo current and the arrival probability is in the same order of magnitude.

## 8.3 Channel geometry

### Perfectly absorbing walls

The experiments were performed also with a different geometry, shown on the left side of fig. 8.2. The great advantage of two different geometries in one single probe lies in the quantitative comparability of the results, since the current detectors and the sample properties are exactly the same. The analysis of the previous chapter has shown that both depletion length  $l$  and the absorption  $a$  influence significantly the probability to detect an electron. This rises the question, what influence stems from the precise geometry.

Also for this geometry, we start with perfectly absorbing walls and zero depletion length, see fig. 8.8(a), (b) and (c). The probability map in (a) shows anew that the maximum probability is situated directly at the detector and that it is strongly decaying with increasing distance with a club-like shape as before. This is underlined by the corresponding cut at  $x = 15.15 \mu\text{m}$  parallel to the  $y$ -axis shown in fig. 8.8(b), which mimics the corresponding distribution of the other geometry, fig. 8.3(b).

The cut parallel to the  $x$ -axis, see fig. 8.8(c) shows exactly the same dependence as for the confinement with circles and can therefore be approximated by the same analytical expression (dashed line). The reason is intuitive: Since the electron cannot scatter at the constrictions, the geometry on the right side is irrelevant, while for an electron heading towards the detector, the structure is the same as before: So, a current can only occur, if the detector can be reached from the illumination spot by a straight line. For the case of large depletion length  $l = 200 \text{ nm}$ , the arguments presented of section 8.2 apply here as well.

### Perfectly reflecting walls

The situation changes for reflecting walls. If the depletion length is zero, we observe in fig. 8.8(a) an increased number of starting points from which electrons can be detected. The cut along the  $y$ -axis (fig. 8.8(b)) shows qualitatively the same pattern as before, but we find a significant difference, namely the sudden drops at  $y \approx 11 \mu\text{m}$  and  $y \approx 19 \mu\text{m}$ . They stem from the intersection of the club with the channel borders, meaning that the width of the channel restricts here the possible starting points with a straight path to the detector. An intersection along the  $x$ -axis is shown in fig. 8.8(c), and the main remarks from the geometry before hold true, but the saturation observed before vanished. We obtain an exponentially decaying probability, but for the non-closed fabric here, the saturation after a certain distance from the detector is not observable, because scattered electrons can escape from the enclosure to the right. Not surprisingly, the overall probability decreases in this open geometry much faster than for the mostly closed circle probe.

All arguments discussed widely the sections before apply here as well, so we

## 8 Photo induced ballistic electron transport

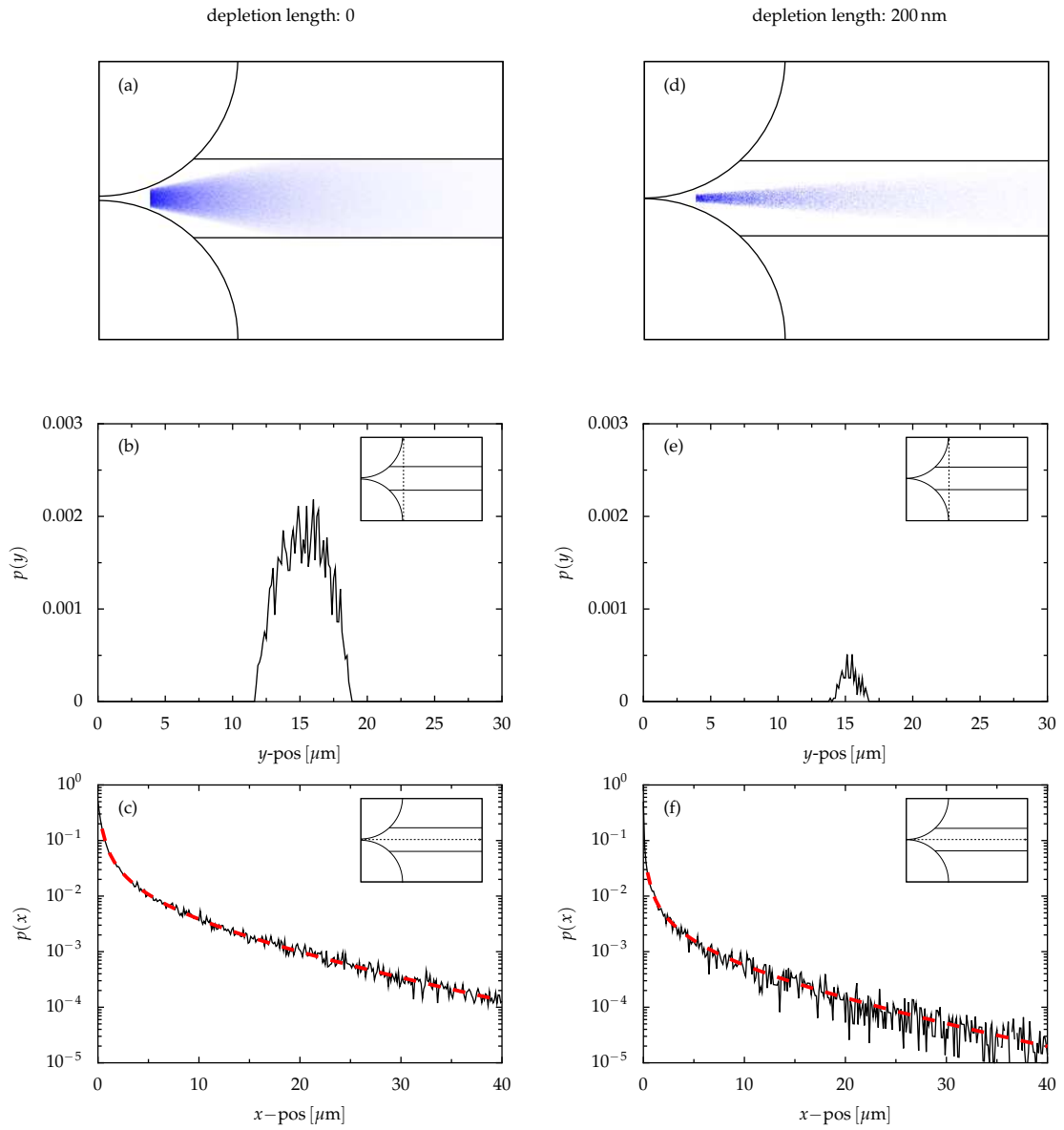


Figure 8.7: In the upper line, the current plots for different depletion lengths  $l$  and perfectly absorbing walls are shown. The centre line shows the probability distribution for fixed  $x = 15.25 \mu\text{m}$ , i.e., parallel to the  $y$ -axis. In the last line the corresponding cut parallel to the  $x$ -axis ( $y = 15.25 \mu\text{m}$ ) is shown.

### 8.3 Channel geometry

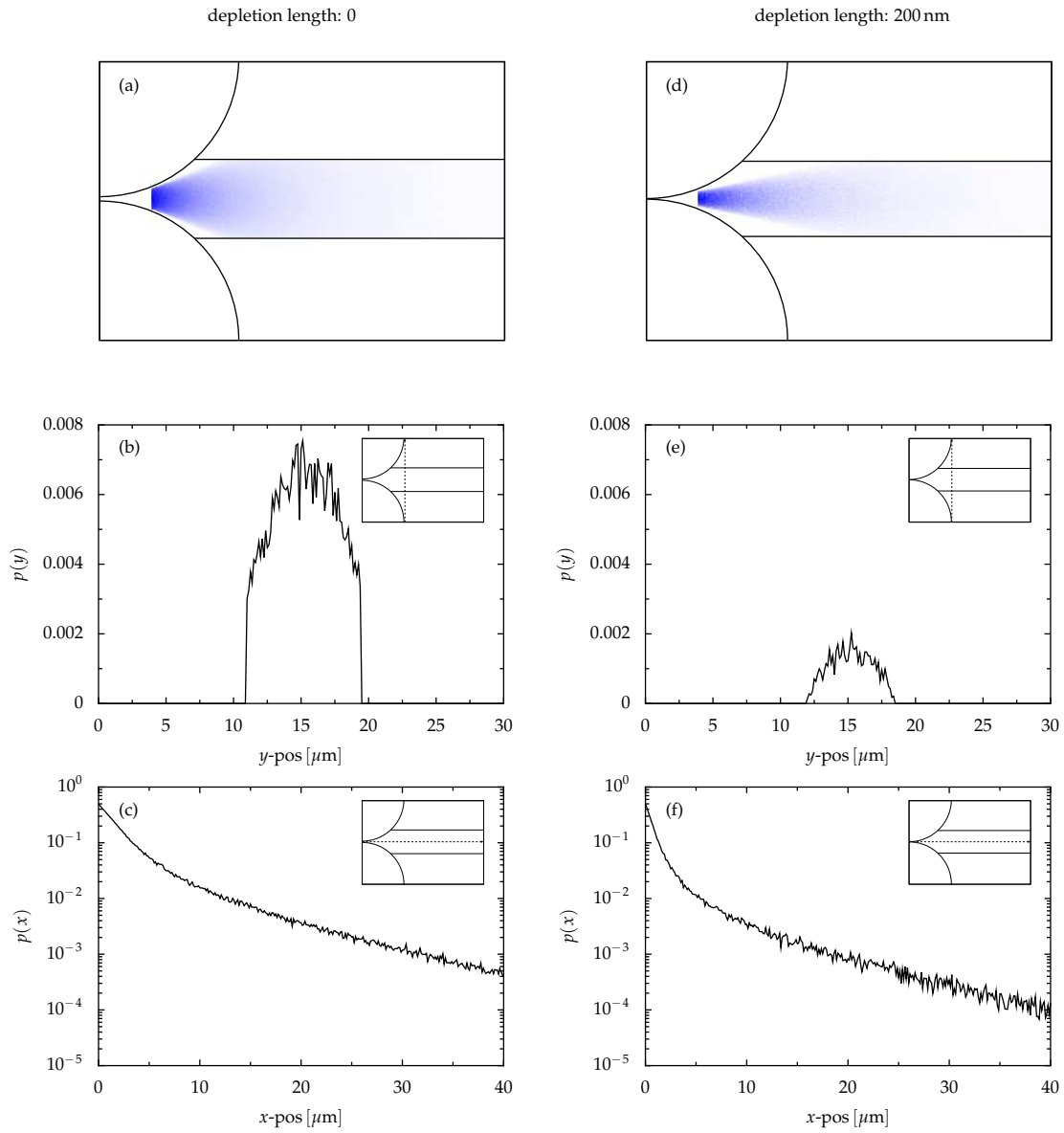


Figure 8.8: In the upper line, the current plots for different depletion lengths  $l$  and perfectly reflecting walls are shown. The centre line shows the probability distribution for fixed  $x = 15.25 \mu\text{m}$ , i.e., parallel to the  $y$ -axis. In the last line the corresponding cut parallel to the  $x$ -axis ( $y = 15.25 \mu\text{m}$ ) is shown.

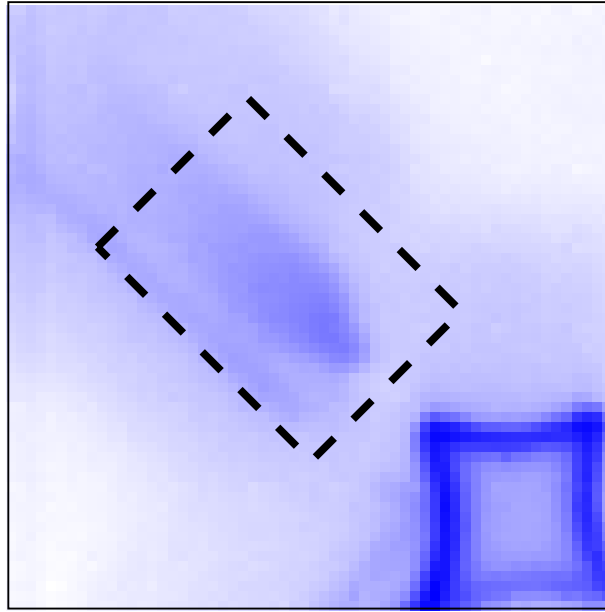


Figure 8.9: Current for every illumination point of the sample in fig. 8.1, scanned area  $60 \times 60 \mu\text{m}$ . Blue areas mark a high current, while white denotes no current. Note that the measurements were performed in the picket shaped white structure in the centre of the image, while the blue rhombus is again a side-effect of the detection process

analyse the results for  $l = 200 \text{ nm}$  fig. 8.8(d),(e) and (f), very briefly. Only the missing sharp drops in the cut parallel to the  $y$ -axis, see fig. 8.8(e), is worth noting: It is not visible for larger  $l$  since due to the large depletion zone the club is so narrow that at  $x = 15.25 \mu\text{m}$  the width of the aperture is still smaller than the channel width.

### Comparison with experimental data

As for the "circles" geometry, we want to compare our numerical results with the measured data, shown in Fig. 8.9 [23]. The region under investigation is located the centre of the image and reaches the way up towards the upper left corner (black rectangle). The bright white rhombus in the lower right corner is again an artifact from the measurement process and will not be discussed further. The homogeneous current map indicates once again that the absorption probability at the boundaries is significantly smaller than one, otherwise we would observe a sharp edge between regions with and without current.

As for the circle-enclosed geometry we concentrate on the current as a function of the distance to the QPC, which is depicted in fig. 8.10. We observe a clear exponential decay of the measured current if we neglect again the region near the

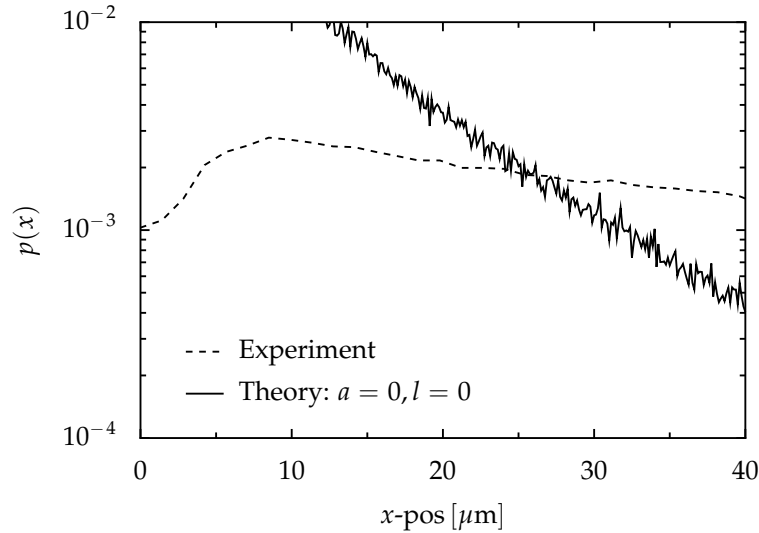


Figure 8.10: Cut along the diagonal from the lower right to the upper left corner, with zero at the QPC. Note the logarithmic scale on the  $y$ -axis.

QPC between  $x = 0 \mu\text{m}$  and  $x = 10 \mu\text{m}$ .

Our numerical simulation with depletion length  $l = 0$  and vanishing absorption rate  $a$  exhibits also an exponential decay, but at a much faster rate. While the order of magnitude matches the experiment again well, the decrease as a function of distance is too strong in the numerical study.

## Conclusion

We have developed a model for the electron movement in a confined structure that is based on a classical ballistic transport, neglecting interaction and quantum effects.

To cover relaxation processes of the electrons on their way through the structure, an exponential suppression for their weight at the detector is employed. Thus, the characteristic length scale is the mean free path. Since in the experiment, the absorption rate at a boundary and the depletion length stemming from the applied potentials cannot be determined precisely, we investigated their influence on the resulting current maps.

For the “circles” structure and high absorption rates, we found very sharp borders between regions with straight access to the QPC and those without. Moreover, we derived an analytical solution based on geometrical considerations for the arrival probability as a function of the distance, which our numerics reproduced very well. Near the QPC the geometry determines mostly the arrival probability, while with increasing distance the weight factor comes more and more into play, leading finally to an exponential decaying detection probability. The

## 8 *Photo induced ballistic electron transport*

effects of a large depletion length scale mainly the arrival probability and diminish the area where photo induced current can occur, due to the smaller size of the constraint at the QPC.

For the same structure, the results differ significantly if electrons can scatter at the curbs. As expected, the overall shape of the current map shows a softer transition between isolating and conducting regions, owing to the increased number of possible trajectories for the electrons. A saturation of the arrival probability as a function of distance was found and we relate this effect to the geometry that prevents electrons from leaving the system.

By comparing the experimental data with our numerical simulation, we found that our model covers most of the physics. The observed saturation deep inside the structure is reproduced. However, close to the QPC and the edges, our description fails.

Switching to the “channel”-like geometry, the main observations outlined above hold true as well. Comparing theory and experiment, we found again that our numerical study is in the same order of magnitude. But the exponential decay predicted by the simulation is not observable in the measurements, at least it is much smaller than our theoretical results for the current.

Therefore, we can conclude that a classical treatment of the optically induced electrons is justified and captures the main physics at work. For starting points near the curbs or the QPC however, our model is not elaborated enough.



## 9 Summary and outlook

In this thesis we considered the electron transport in nanoscale systems driven by an external energy source. We introduced a tight-binding Hamiltonian containing an interaction term that describes a very strong Coulomb repulsion between electrons in the system. Since we dealt with time-dependent situations, we employed a Floquet theory to take into account the time periodicity induced by different external oscillating fields. For the two-level system, we even provided an analytical solution for the eigenenergies with arbitrary phase shift between the levels for a cosine-shaped driving. To describe time-dependent driven transport, we derived a master equation by tracing out the influence of the surrounding leads in order to obtain the reduced density operator of the system.

We generalised the common master equation for the reduced density operator to perform an analysis of the noise characteristics. The concept of Full Counting Statistics in electron transport gained much attention in recent years [14, 47], and has proven its value as a powerful theoretical technique. By combining its advantages with the master equation approach, we found a hierarchy in the moments of the electron number in one lead that allowed us to calculate the first two cumulants. The first cumulant could be identified as the current passing through the system, while the noise of this transmission process is reflected by the second cumulant. Moreover, in combination with our Floquet approach, the formalism is not limited to static situations, which we proved by calculating the current and noise characteristics for the non-adiabatic electron pump.

Since we limited our study to the first and second cumulant, one naturally might ask if the computation of higher order cumulants is possible within this framework. Nevertheless, the importance and possible insight from higher order cumulants is currently discussed controversially [91].

We studied the influence of a static energy disorder on the maximal possible current for different realisations. The probability distribution of the currents in an open transport channel demonstrates that with increasing system length the effect of rather tiny fluctuations increases drastically. We concluded that the reason for this behaviour lies in the increasing probability to find one level in the system misaligned and so inhibiting effectively transport. Further, we explored the possibility of non-adiabatically pumping electrons in an initially symmetric system if random fluctuations break this symmetry. We found that fluctuations may alter the distribution of the current, but already rather small bias voltages suppress pumping. Our analysis revealed that for longer systems, that is working with a large number of levels, even very small fluctuations might lead to an effectively isolating behaviour. Since this energy disorder is inevitable in the real setups, e.g.,

in a possible quantum computer that reads out the qubit by measuring a current, one should take care to (i) minimise the fluctuations or (ii) reduce the number of incorporated levels, such that the fluctuations cannot inhibit transport. Otherwise, the reproducibility of the results might be strongly decreased.

Motivated by recent and upcoming experiments [20–22], we used our extended Floquet model to properly describe systems driven by propagating waves that induce a phase lag between neighbouring sites. Physical realisations might be quantum dots driven by surface acoustic waves (SAW) or by properly adjusted gate electrodes. For a qualitative analysis of SAW driven quantum dot systems, we adopted our model to the static situation and extracted the numerical values. The study of the same system in a driven configuration was hindered by the very small resulting driving frequency and the consequent huge numerical effort. Nevertheless, it may be worth the price to investigate further this systems, since we have seen that in the theoretical model the sign of the current depends sensitively on the phase difference between the sites. The direct relation between phase lag and spacing of the dots as well as the well-defined wavelength of the SAW, may work as a “ruler” to measure the distance between the quantum dots. Furthermore, there are current attempts to emulate a propagating wave in a fully controllable triple quantum dot [78]. Then, the study of the current for arbitrary phase lags becomes possible; opening the way to an experimental test for our model. It will be exciting to see if our theoretical predictions, like current suppression at certain parameters, amplitude-independent current, and current reversals, can be found in the experiment.

Recent measurements of the photoconductive gain and more detailed studies on photo induced ballistic transport indicated an influence of geometrical constraints on the electron path. Within this thesis we numerically evaluated the current for latter in two distinct geometries. Unlike in the other systems discussed in this thesis, we simulated the electrons as free non-interacting particles. The comparison of our simplified model for the charge carriers with the measured current reproduced well the experimental results in both geometries. Moreover, the absolute values agreed well with the experiment, taking our reduced model into account. Our results proved that a description of the electrons as free moving particles in the two dimensional electron gas is justified and already suitable to understand the experimental results. The deviations we observed near the edges might be reduced by improving the model, for example by taking charge accumulation due to holes at the boundaries into account or by employing a more sophisticated model for the scattering with the lattice.

# A Floquet theory

The quantum mechanical treatment of a time-dependent system is in general a formidable task. However, the restriction to a time-periodic system bears some great advantages in the mathematical effort. Similar to the well-known Bloch-Theorem in solid state physics, which relies on the spatial periodicity of the lattice, the Floquet-Theorem allows computation of time-periodic problems. Floquet's work on the solution of differential equations with time-periodic coefficients [92] has been extended by several groups to describe driven quantum systems [93–95]. We review briefly the most important points of a Floquet description of transport through quantum systems and focus on the physical mechanisms underlying that approach.

## A.1 Overview of general properties

Since we deal with time-periodic fields and neglect transient effects, we expect the solutions of the time-dependent Schrödinger equation

$$\left(H(t) - i\hbar \frac{\partial}{\partial t}\right) |\psi(t)\rangle = |0\rangle \quad (\text{A.1})$$

also to be time-dependent. For the given Hamiltonian, which is  $\mathcal{T}$ -periodic

$$H(t) = H(t + \mathcal{T}), \quad \mathcal{T} = 2\pi/\Omega \quad (\text{A.2})$$

a symmetry operator  $S$  that shifts the time argument by one period  $t \rightarrow t + \mathcal{T}$  commutes with the operator  $H(t) - i\hbar \frac{\partial}{\partial t}$ . Thus, the solutions  $|\psi\rangle$  of the Schrödinger equation are, apart from a meaningless phase factor, also eigenfunctions of the symmetry operator  $S$ . Since it keeps the norm of any state vector, we can assume the eigenvalue equation of  $S$  to be of the form

$$S(t)|\psi(t)\rangle = |\psi(t + \mathcal{T})\rangle = e^{i\Phi} |\psi(t)\rangle. \quad (\text{A.3})$$

This is equivalent to the Bloch theorem, where electrons move in a periodic potential created by the lattice atoms. Thus, we use an ansatz composed of a plain wave and a periodic part,

$$|\psi(t)\rangle = e^{-i\epsilon t/\hbar} |\varphi(t)\rangle, \quad (\text{A.4})$$

with  $\epsilon = \hbar\Phi/\mathcal{T}$ . Effectively, the split in two factors corresponds to a time scale separation. The evolution of a state within one driving period  $\mathcal{T}$  is governed by

## A Floquet theory

$|\varphi_\alpha(t)\rangle$  while the long time behaviour is dominated by the phase factor. Then, the following relation for our so-called Floquet states must hold true;

$$|\varphi(t)\rangle = |\varphi(t + \mathcal{T})\rangle. \quad (\text{A.5})$$

These Floquet states inherit the time-dependence from the Hamiltonian. It can be shown that the  $\{|\varphi_\alpha(t)\rangle\}$  form a complete basis and thus it is possible to express all solutions of the time-dependent Schrödinger equation in terms of the Floquet states  $|\varphi_\alpha(t)\rangle$

$$|\psi_\alpha(t)\rangle = e^{-i\epsilon_\alpha t/\hbar} |\varphi_\alpha(t)\rangle, \quad (\text{A.6})$$

$$|\varphi_\alpha(t)\rangle = |\varphi_\alpha(t + \mathcal{T})\rangle. \quad (\text{A.7})$$

The unit of the  $\epsilon_\alpha$  is energy and so they are called quasi-energy, in accordance with the quasi-momentum in a periodic lattice. Note that in the static situation, the quasi-energies match the eigenenergies of the system. Generically, a single Floquet state  $|\varphi_\alpha(t)\rangle$  is not a solution of the Schrödinger equation and thus, must be constructed from the complete set of Floquet states via

$$|\psi(t)\rangle = \sum_{\alpha}^N u_{\alpha} e^{-i\epsilon_{\alpha} t/\hbar} |\varphi_{\alpha}(t)\rangle, \quad (\text{A.8})$$

with  $u_{\alpha}$  as coefficients to be determined. Now it is possible to obtain an eigenvalue equation with a hermitian Hamiltonian that has to be solved for the computation of both the quasi energies  $\epsilon_{\alpha}$  and the corresponding Floquet state  $|\varphi_{\alpha}\rangle$ . Inserting eq. (A.5) into the original Schrödinger equation results in a Schrödinger-like structure for the Floquet states,

$$\mathcal{H}(t)|\varphi\rangle = \epsilon_{\alpha}|\varphi\rangle, \quad (\text{A.9})$$

with the new Floquet Hamiltonian  $\mathcal{H}(t) = H(t) - i\hbar \frac{\partial}{\partial t}$ , which obviously is again hermitian.

Due to their time-periodicity, the Floquet states can be decomposed into a Fourier series,

$$|\varphi_{\alpha}\rangle = \sum_k e^{-i\Omega t} |\varphi_{\alpha,k}\rangle, \quad (\text{A.10})$$

where the index  $k$  very often is called side band index. This quantity is akin to the band index in solid state physics, where it denotes the energy band, in which the state of electron is located. The fact that Bloch electrons, i.e., electrons that move in a periodic potential give rise to the band structure is reflected in the concept of Brillouin zones. Physically, solutions that differ by an integer of  $\hbar\Omega$  describe the same situation and are therefore physically equivalent. Note that this only holds true, if the number of states is infinite. Applying this to our problem of the time-periodic Floquet states, we obtain

## A.2 Analytical solution for a two-level system

$$\epsilon_\alpha \rightarrow \epsilon_{\alpha,k}, \quad |\varphi_\alpha(t)\rangle \rightarrow e^{ik\Omega t} |\varphi_\alpha(t)\rangle, \quad (\text{A.11})$$

with the integer sideband index  $k$ . For the numerical evaluation of Floquet states, it is therefore sufficient to compute only the states lying in the first Brillouin zone, e.g.,

$$-\hbar\Omega/2 \leq \epsilon_\alpha \leq \hbar\Omega/2. \quad (\text{A.12})$$

The great advantage is the reduced number of states to compute, it is now equal to the number of states in the time-independent problem, but of course one has the side band index  $k$  as an additional parameter. It must be chosen such that the numerical solution surely converges. Thus, calculations can still be rather tedious, although being simplified by the Floquet theorem.

## A.2 Analytical solution for a two-level system

A simple example that can be solved analytically is the case of a two level system with an arbitrary phase shift between the two harmonically oscillating levels and a weak interdot coupling  $\Delta$  such that it can be treated within a perturbational approach. In this case, it is not necessary to go the long way around and use the Fourier decomposition. Then, the unperturbed Hamiltonian reads in onsite-energy representation

$$H_{\text{unperturbed}} = \begin{pmatrix} A \cos(\Omega t + \Theta/2) & 0 \\ 0 & A \cos(\Omega t - \Theta/2) \end{pmatrix}, \quad (\text{A.13})$$

a more convenient representation of  $H_{\text{unperturbed}}$  with Pauli spin matrices reads

$$\begin{aligned} H_{\text{unperturbed}} &= A \cos(\Theta/2) \cos(\Omega t) \mathbb{1} - A \sin(\Theta/2) \sin(\Omega t) \sigma_z \\ &= \mathcal{A} \cos(\Omega t) + \mathcal{B} \sin(\Omega t), \end{aligned} \quad (\text{A.14})$$

where we used for the sake of readability the definitions  $\mathcal{A} = A \cos(\Theta/2) \mathbb{1}$ . and  $\mathcal{B} = -A \sin(\Theta/2) \sigma_z$ . The operators  $\mathcal{A}$  and  $\mathcal{B}$  share a common set of eigenvalues and eigenstates that read  $\lambda_{1,2} = 1, -1$  and the corresponding eigenstates of the unperturbed system are  $(1, 0), (0, 1)$ . A formal solution of the Schrödinger equation can be written in terms of a propagator  $U(t, t')$ , in our case

$$U(t, 0) = e^{-i(\mathcal{A}/\Omega) \sin(\Omega t) + i(\mathcal{B}/\Omega) \cos(\Omega t) - i\mathcal{B}/\Omega}. \quad (\text{A.15})$$

By construction, it fulfils  $U(0, 0) = U(\mathcal{T}, 0) = 1$ , which reflects the time periodicity of the system with the driving period  $\mathcal{T}$ . Knowing the propagator, one can write the Floquet states at arbitrary time

$$|\varphi_\alpha(t)\rangle = U(t, 0) |\varphi_\alpha(0)\rangle = e^{-i(\mathcal{A}/\Omega) \sin(\Omega t) + i(\mathcal{B}/\Omega) \cos(\Omega t) - i\mathcal{B}/\Omega} |\varphi_\alpha(0)\rangle. \quad (\text{A.16})$$

## A Floquet theory

This states describe fully the dynamics of the system within a driving period in the unperturbed system. In the situation of weak interdot coupling  $\Delta$  the perturbation Hamiltonian

$$H_{\text{perturbation}} = \Delta \sigma_x. \quad (\text{A.17})$$

To obtain the eigenenergies of the perturbed system in first order, we need to evaluate terms of the kind  $\frac{1}{T} \int_0^T \langle \varphi_{1,2} | H_{\text{perturbation}} | \varphi_{1,2} \rangle$ . The integration over one driving period is an averaging such that we obtain the quasi energies in the Floquet basis. The fact that  $H_{\text{perturbation}} \propto \sigma_x$  leads to the observation  $\langle \varphi_1 | \sigma_x | \varphi_1 \rangle = \langle \varphi_2 | \sigma_x | \varphi_2 \rangle = 0$  and the off-diagonal elements read then

$$\begin{aligned} \langle \varphi_1 | H_{\text{perturbation}} | \varphi_2 \rangle &= \Delta e^{-2ib_1/\Omega} \int_0^T dt e^{-2i/\Omega b_1 \cos(\Omega t)} = \Delta e^{-2ib_1/\Omega} J_0(-2b_1/\Omega), \\ \langle \varphi_2 | H_{\text{perturbation}} | \varphi_1 \rangle &= \Delta e^{-2ib_2/\Omega} \int_0^T dt e^{-2i/\Omega b_2 \cos(\Omega t)} = \Delta e^{-2ib_2/\Omega} J_0(-2b_2/\Omega), \end{aligned} \quad (\text{A.18})$$

where  $b_{1,2}$  denotes the respective eigenvalues of  $\mathcal{B}$ . Now, we can write  $H_{\text{perturbation}}$  in the basis of the subspace as

$$H'_{\text{perturbation}} = \Delta J_0(2A \sin(\Theta/2)/\Omega) \begin{pmatrix} 0 & e^{-2i \sin(\Theta/2)/\Omega} \\ e^{2i \sin(\Theta/2)/\Omega} & 0 \end{pmatrix}, \quad (\text{A.19})$$

the corresponding eigenvalues are the quasienergies of the system in first order perturbation theory and so

$$\epsilon_{1,2} = \pm \Delta J_0(2A \sin(\Theta/2)/\Omega), \quad (\text{A.20})$$

where  $J_0$  denotes the Bessel-function of zeroth order.

Using eq. (A.20), a computation of the quasienergies in a degenerate two level system for a varying phase shift  $\Theta$  is shown in fig. A.1. The Bessel function dominates the quasienergy splitting and leads to the non-monotonic behaviour with the dip at  $\Theta \approx 0.4 \pi$  where  $J_0$  has a zero. Interestingly, the splitting remains constant over a rather large range centred around  $\Theta = \pi$ .

A variation of the ratio  $A/\Omega$  for a fixed phase shift  $\Theta$  is shown in fig. A.2. Here, the zeroth order Bessel function  $J_0$  is simply scaled on the  $x$ -axis, because its argument is now a linear function of the variable  $A$ .

## A.3 Floquet theory for second quantisation

Since we use a model written in the second quantisation with fermionic creation and annihilation operators, one might ask, what is the effect of a, e.g., creation operator  $c_n^\dagger$  on an arbitrary Floquet state  $\varphi_\alpha$ ? In this section, we want to rewrite the creation and annihilation operators such that they act on the Floquet states.

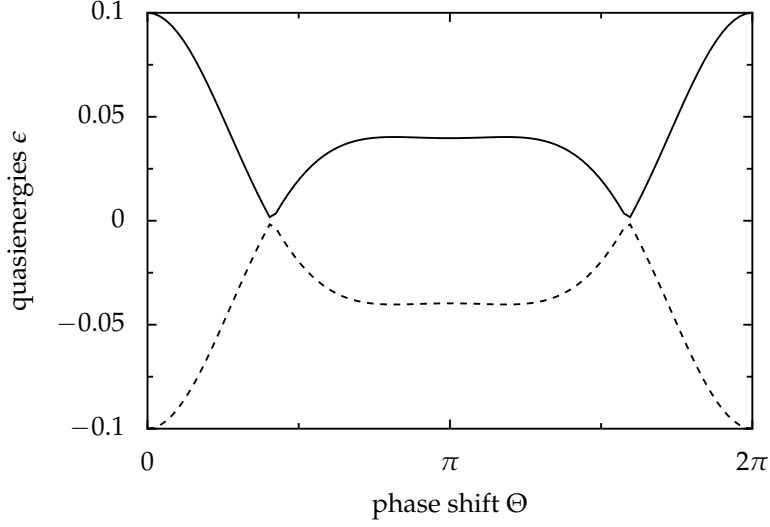


Figure A.1: Quasienergies  $\epsilon$  of the degenerate two levels system for hopping  $\Delta = 0.1$ , driving field with amplitude  $A = 4\Delta$  and frequency  $\Omega = 2\Delta/\hbar$  and varying phase shift  $\Theta$ .

The goal is to express all our computations in terms of the Floquet basis, so we can take advantage of their features, especially the time-periodicity. A proper way to perform the transformation is shown in ref. [96], then the transformation reads

$$c_\alpha(t) = \sum_n \langle \varphi_\alpha(t) | n \rangle c_n. \quad (\text{A.21})$$

Using that the Floquet states are complete at equal times [97] and mutually orthogonal one can write the back transformation as

$$c_n = \sum_\alpha \langle n | \varphi_\alpha(t) \rangle c_\alpha(t). \quad (\text{A.22})$$

Most interesting, the right-hand side of Eq. (A.22) is independent of the time argument  $t$ , since both time dependencies cancel after the summation. Yet, we need another small step towards our goal of rewriting all expressions in the Floquet basis. It will turn out later in the derivation of the master equation that we need the operators in the interaction picture. After the transformation, the Floquet annihilation operator (A.21) has the interaction picture representation

$$\begin{aligned} \tilde{c}_\alpha(t, t') &= U_0^\dagger(t, t') c_\alpha(t) U_0(t, t') \\ &= e^{-i(\epsilon_\alpha + U\mathcal{N}_{\text{wire}})(t-t')/\hbar} c_\alpha(t'), \end{aligned} \quad (\text{A.23})$$

where the time difference  $t - t'$  enters solely via a phase factor. Relation (A.23) can easily be shown by computing the time derivative with respect to  $t$ , which by use

## A Floquet theory

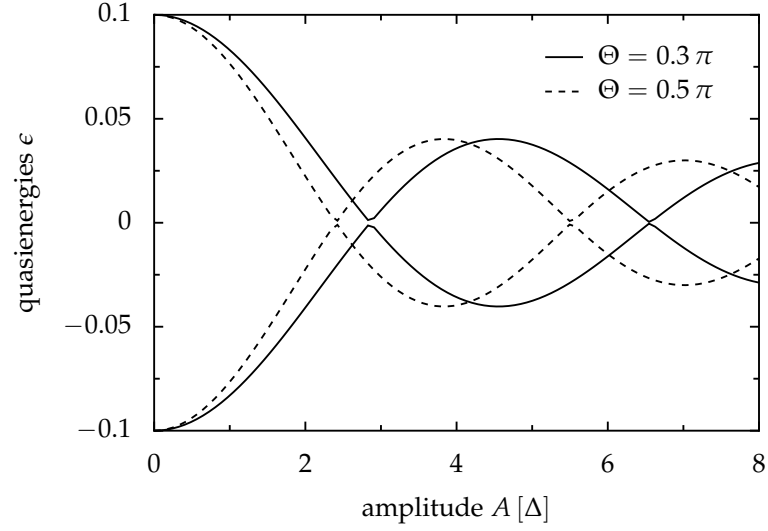


Figure A.2: Quasienergies  $\epsilon$  of the degenerate two levels system for two different phase shifts  $\Theta$ , hopping  $\Delta = 0.1$ , driving field with frequency  $\Omega = 2\Delta/\hbar$  and varying amplitudes  $A$ .

of the Floquet equation (A.9) becomes

$$\frac{d}{dt}\tilde{c}_\alpha(t, t') = -\frac{i}{\hbar}(\epsilon_\alpha + U\mathcal{N}_{\text{wire}})\tilde{c}_\alpha(t, t'). \quad (\text{A.24})$$

Together with the initial condition  $\tilde{c}_\alpha(t', t') = c_\alpha(t')$  follows relation (A.23). Note that the time evolution induced by  $\mathcal{H}_{\text{wire}}(t)$  conserves the number of electrons on the wire.



## B Extracting model parameters from experimental data

In this appendix we test the applicability of our tight-binding model to the system used in the experiments and obtain the relevant parameters for our theoretical approach from the measurements [77].

### B.1 Experimental realisation

All the measurements are performed on a two dimensional electron gas (2DEG) of a GaAs/AlGaAs heterostructure [98]. By standard techniques, one obtains the structure shown in fig. B.1(a), where the red (dark) areas indicate regions containing the 2DEG. The structure is  $8\ \mu\text{m}$  long and in total about  $10\ \mu\text{m}$  wide. The inner structure is sawtooth shaped with four teeth and asymmetric with respect to the vertical centre line. For a detailed discussion of the manufacturing techniques and the precise specifications of the sample see ref. [77]. By applying a sufficiently large voltage to the right in-plane-gates one ensures that the 2DEG is repelled from the region [99, 100] and conduction solely occurs in the left channel of the system. The resulting distribution of the 2DEG is shown in fig. B.1(b), while figure B.1(c) displays the wiring scheme of the sample. A negative voltage applied to the left channel enables a control of the channel size. Increasing the voltage, the channels gets narrower up to the situation, where three potential barriers arise at the teeth of the structure. This marks the transition from a 1D conduction [31, 86] to a 0D conduction [86, 101–104] serially along the hopefully emerged row of quantum dots (QD), and finally the isolating situation is shown in fig. B.2. The characteristic voltage for which the isolation sets in is called pinch-off. For less negative gate voltages a conduction plateau forms which is characteristic for 1D conduction. The non-monotonic and erratic behaviour for more negative gate voltages points at a very complicated electronic structure near the completely isolating pinch-off. All the measurements shown in fig. B.2 were performed at Helium temperature of  $T = 1.3\ \text{K}$  and a source-drain bias voltage of  $V_{\text{SD}} = 0.1\ \text{mV}$ .

### Static setup

We will use the case of static conduction to analyse if our tight binding model is appropriate for the description of transport and tune the parameters consequently.

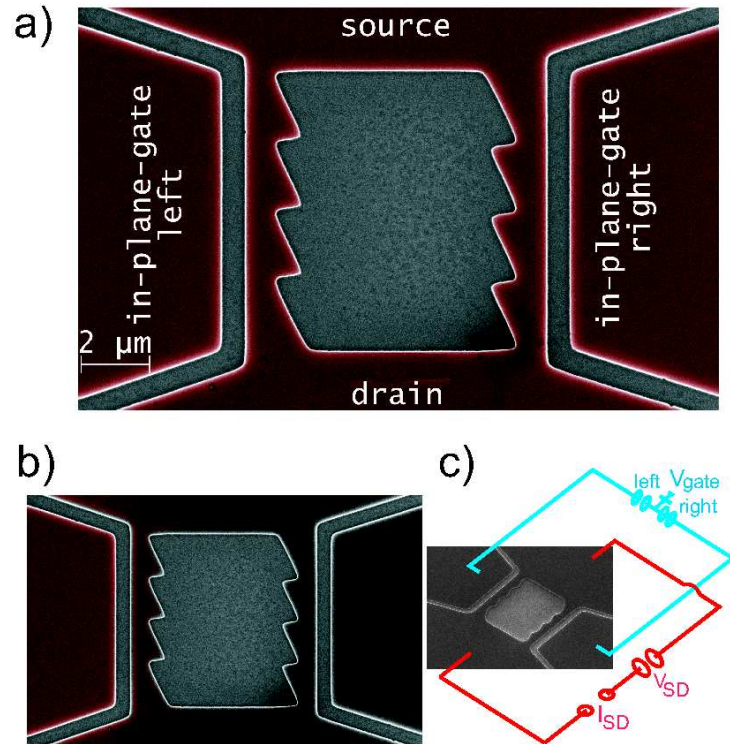


Figure B.1: (a) Scanning electron micrograph of the sample. Red (darker) areas are highlighting 2DEG, black (brighter) areas are wet-etched and non-conducting. The annealed ohmic contacts (not shown) are labelled. The depletion of the left channel (under investigation) is controlled by the left in-plane gate. The channel can be made narrower by applying a more negative voltage to the gate until all electrons are forced out of the channel. In our experiment the right channel is completely depleted by applying a sufficiently large voltage ( $-4.5$  V) to the right gate as shown in panel (b). (c) Wiring scheme of the sample.

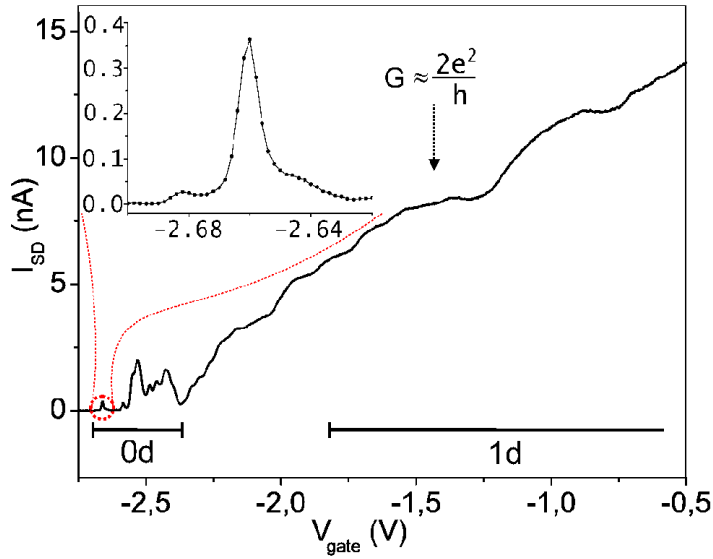


Figure B.2: Measured current through the left channel with decreasing voltage on the left in-plane gate at 1.3K. The applied source-drain-voltage is  $V_{SD} = 0.1$  mV. The system is evolving from the 1d regime, characterised by current plateaus, the into QD-regime with characteristic Coulomb oscillations. Inset: blow-up of the very first oscillation ( $U_{gate} = -2.66$  V) next to the pinch-off.

Figure B.3(a) shows the differential conductance  $dI/dV_{SD}$  that demonstrates some significant distinctions from “regular” Coulomb diamonds. Most obvious, the structure of the diamond is sloped to the left, which indicates an asymmetric coupling to the leads present in most experiments. Further, subtle structures in the diamond are visible. The most striking one is a small area of high conductivity (marked with \* in figure B.4), where the conduction edges nearly touch. Also, stripes of conductivity (marked with +) parallel to the main areas are present. Note that these regions are nearly symmetric with respect to the source-drain voltage, but strongly asymmetric with respect to the gate voltage. Their presence is limited to low gate voltages, while for larger gate voltages a sharp crossover from transport to the Coulomb blockade regime occurs. Last, there are areas of large conductivity (marked with #), again symmetric in the bias voltage and asymmetric with respect to the gate voltage applied.

Although structure B.1(b) suggests three QD serially connected, we will employ a two level system to explain the observed peculiarities. Since a precise determination of the number of dots emerging is not possible, we restrict the theoretical model to the most simple case explaining all features outlined above. Figure B.3 demonstrates that the two level system is already appropriate to describe and un-

derstand the physics at work.

## B.2 Comparison with experimental data

At the beginning, we discuss the numerical findings of our two dot model, see fig. B.5. This analysis will highlight the strong Coulomb interaction as a decisive part in the understanding of the theoretical as well as the experimental data.

For the case of very large negative gate voltages  $V_{\text{gate}}$ , the resulting eigenenergies lie well above the Fermi energies of the two leads. Since effective transport only occurs, if at least one eigenenergy lies inside the voltage window, the corresponding current is very small, but not exactly zero, since cotunneling processes allow for a very limited transmission from one lead to the other. Increasing  $V_{\text{gate}}$ , the lower dot level enters the voltage window, see figure B.6(a), and resonant transport occurs. This is reflected by a peak in the differential conductance. Even larger gate voltages force both eigenenergies inside the voltage window, thus leading to a maximal transmission. If the electrons are not effected by each other, i.e., the Coulomb interaction  $U = 0$ , the current doubles, since the channels are completely independent. If a Coulomb interaction is present, this is not the case anymore, and although the current still increases with a second possible path, it is not doubled due to possible jamming inside the system.

The results for both interaction strengths differ dramatically, if  $V_{\text{gate}}$  is raised even more, see figure B.6(b). Then, one of the eigenenergies is below both Fermi energies of the leads, while the other still remains inside the voltage window. Since for noninteracting electrons an electrons hole symmetry is present, the transmission properties are the same as before, where one level was situated above the voltage window. If a finite Coulomb interaction is now present the situation changes dramatically. An incoming electron must pay an extra energy to overcome the repulsive force of the electron in the always occupied lower eigenstate. So, if the Coulomb interaction is the dominate energy scale in the problem, the repulsion can prohibit effectively a second electron from entering the system. Since in a stationary condition, the lower electron cannot escape from the system neither to the right nor to the left — the corresponding states in the leads are occupied — and the conduction is suppressed. This effect can be seen as an even qualitative difference in the Coulomb diamond structure of figure B.3: As outlined above, the non-interacting case  $U = 0$  corresponds to an electron-hole symmetry, leading to a Coulomb diamond, see figure B.3(c), invariant under the change of signs for both the source-drain voltage and the gate voltage. The presence of a very strong interaction, see figure B.3(b), cancels the symmetry concerning the sign of  $V_{\text{gate}}$ . Moreover, the experimental data lack the second spot of high conductivity at  $V_{\text{SD}} \approx 0$  present in our theoretical results for no interaction. This fact clearly points at a strong Coulomb repulsion between the electrons inside the system.

For both interaction strengths,  $U = 0$  and  $U = \infty$ , the Coulomb diamond share common features. Whenever the energy levels enter the voltage window from

## B.2 Comparison with experimental data

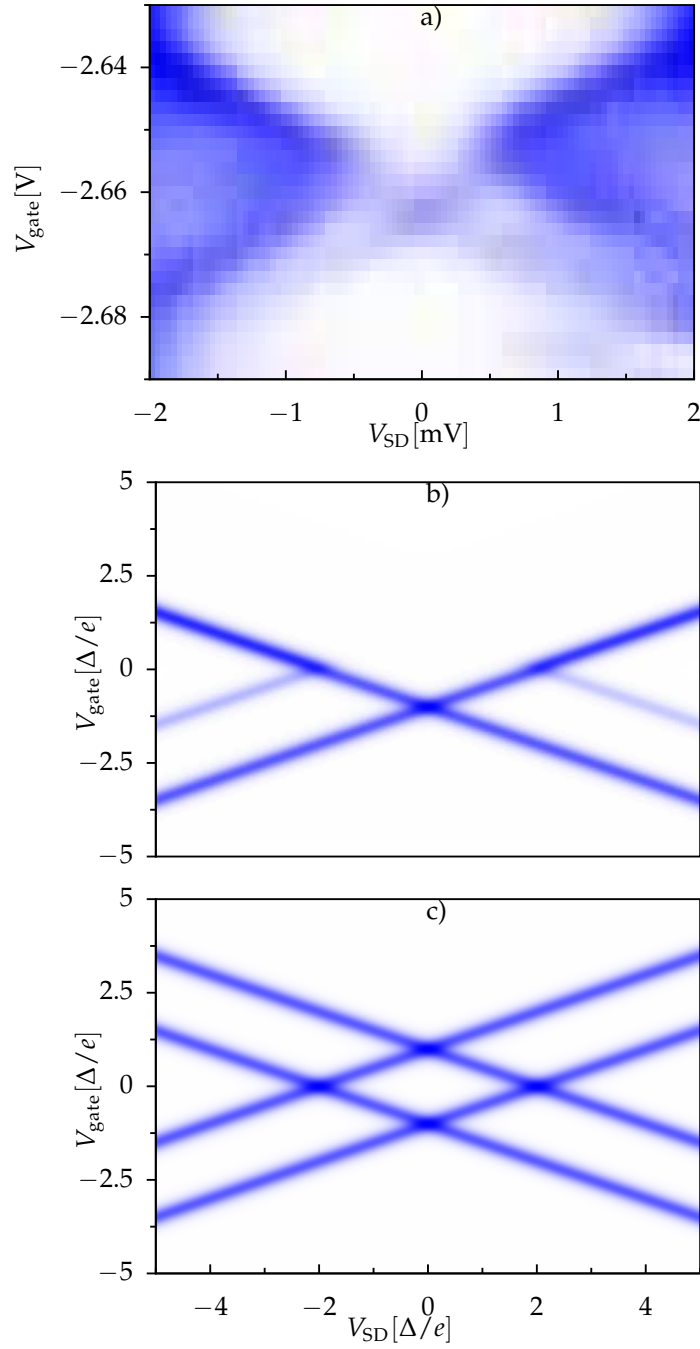


Figure B.3: False-colour-plot of the differential conductance  $dI/dV_{SD}$  as a function of source-drain bias and gate voltage. Blue corresponds to low conductance and red to high conductance. The experimental data (a) described in section B.1 are compared to theoretical results for a double quantum dot with interacting (b) and non-interacting (c) electrons. The theoretical calculations are for dot-lead couplings  $\Gamma_L = 0.2 \Delta$ ,  $\Gamma_R = 0.25 \Delta$  and temperature  $k_B T = 0.1 \Delta$ .

## B Extracting model parameters from experimental data

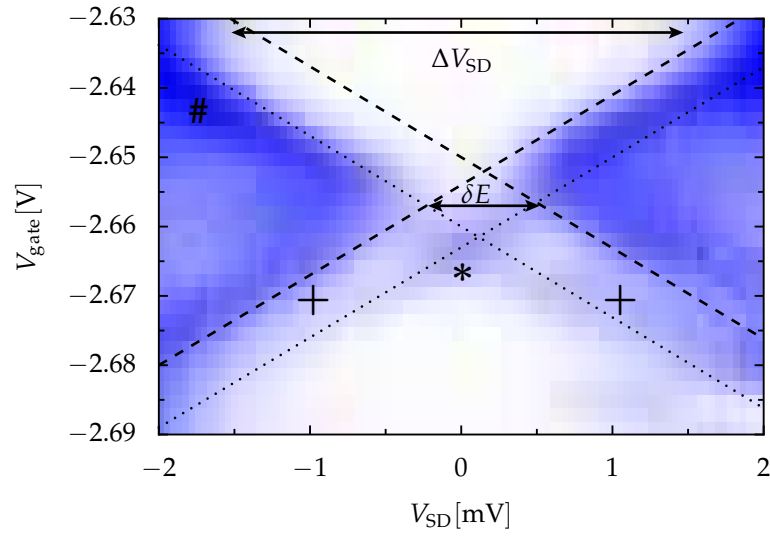


Figure B.4: Sketch of the system characteristics superimposed to the experimental data. From the slope of the dashed lines one can estimate the capacities of the dot, the dotted lines highlight the stripes of elevated conductivity. The symbols \*, + and # mark parameter regions mentioned in the text. The total capacity of the system can be estimated from the value of  $\Delta V_{SD}$  [105].

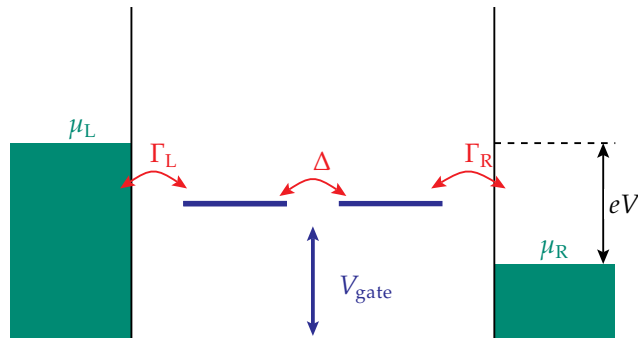


Figure B.5: Tight-binding model for a double quantum dot coupled to two leads. An external bias voltage  $V_{SD} = (\mu_R - \mu_L)/e$  is applied to the mesoscopic system.

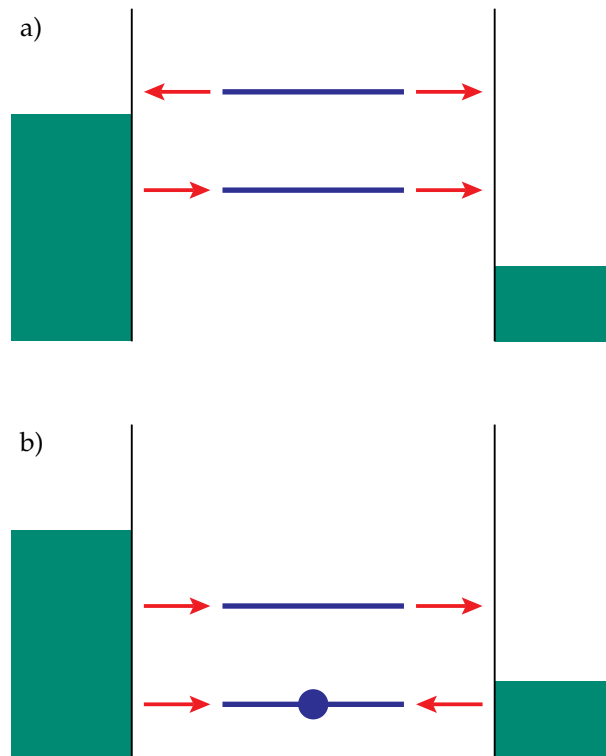


Figure B.6: Sketch of the transport through eigenenergy levels for different gate voltages. The arrows indicate the possible tunnel events for electrons into and out of the system. In panel (a),  $V_{\text{gate}}$  is so large that only one level lies within the voltage window, while the other one lies well above and is never occupied. Consequently, transport is interaction independent. If one level lies below both chemical potentials (b), it will be occupied in the steady state and, thus, strong Coulomb repulsion inhibits the electron transport.

## B Extracting model parameters from experimental data

above, an increase of the current in two distinct steps can be observed. The separation of the steps is fully determined by the splitting  $\delta E$  of the two eigenenergies and corresponds to a voltage  $\delta E/e$ . This permits us to evaluate the excitation energy of an orbital degree of freedom measuring the (differential) conductance. Figure B.4 depicts again the experimental results of figure B.3(a), but as an guide to the eye, the idealised structure of the diamond is marked by dashed and dotted lines.

Comparing the experimental Coulomb diamond in fig. B.3(a) with the theoretical calculation in figure B.3(b), we obtain the tunnel coupling  $\Delta = 0.33$  meV. The asymmetric coupling constants to the right (left) lead read  $\Gamma_R = 0.25 \Delta$  ( $\Gamma_L = 0.2 \Delta$ ). Note that this values for the tunnel rates comprehend a rather high uncertainty, since they influence in the theoretical model only the steepness of the current steps. So, they are free fit parameters, chosen such that both, experimental and numerical, Coulomb diamonds look the same. With these numbers at hand, we can compute the current for plateaus at the left side (0.9 nA) and the right side (1.0 nA) respectively. The theoretical results show a good agreement with the measured values at the edges of the Coulomb diamonds (2 nA – 3 nA).

The good agreement of our model with strong repulsion  $U = \infty$  suggests that in the experiment the localised states strongly repel each other. But this poses the question, where in the sample the localised states form. From the geometry shown in figure B.1, one would expect that four barriers form at the tips of the sawtooth fingers intersecting the wire into three parts. Since features of a one-dimensional system were measured, see figure B.2, one of the etched constrictions must govern the transport in the open channel regime, the formation of four equal barriers seems rather improbable. By construction of the setup, we cannot determine which of the constrictions is the dominant one and we also must think of an unintentionally quantum dot emerged from a inevitable charged impurity. This impurities present in every heterostructure freeze during the cooling process and their charge can influence the potential shape significantly [106].

With this results, it is not feasible to exclude one of the possibilities named above. However, from the good agreement of the numerical results for a strong inter dot coupling  $\Delta$  and the strong Coulomb interaction inside the system we can conclude that the dots must be in near vicinity.



# Bibliography

- [1] G. E. Moore, *Cramming More Components Onto Integrated Circuits*, *Electronics* **38**, 114 (1965).
- [2] L. P. Kouwenhoven, C. M. Marcus, P. L. McEuen, S. Tarucha, R. M. Westervelt, and N. S. Wingreen, *Electron Transport in Quantum Dots*, in *Electron Transport in Quantum Dots, Proc. Nato ASI "Mesoscopic Electron Transport"*, edited by L. P. Kouwenhoven, G. Schön, and L. L. Sohn (Kluwer, Dordrecht, 1997).
- [3] W. G. van der Wiel, S. De Franceschi, J. M. Elzerman, T. Fujisawa, S. Tarucha, and L. P. Kouwenhoven, *Electron transport through double quantum dots*, *Rev. Mod. Phys.* **75**, 1 (2003).
- [4] Y. Alhassid, *The statistical theory of quantum dots*, *Rev. Mod. Phys.* **72**, 895 (2000).
- [5] S. Reimann and M. Manninen, *Electronic structure of quantum dots*, *Rev. Mod. Phys.* **74**, 1283 (2002).
- [6] R. Hanson, L. P. Kouwenhoven, J. R. Petta, S. Tarucha, and L. M. K. Vandersypen, *Spins in few-electron quantum dots*, *Rev. Mod. Phys.* **79**, 1217 (2007).
- [7] V. S. Khrapai, S. Ludwig, J. P. Kotthaus, H. P. Tranitz, and W. Wegscheider, *Double-Dot Quantum Ratchet Driven by an Independently Biased Quantum Point Contact*, *Phys. Rev. Lett.* **97**, 176803 (2006).
- [8] D. Taubert, M. Pioro-Ladriere, D. Schroeer, D. Harbusch, A. S. Sachrajda, and S. Ludwig, *Telegraph noise in coupled quantum dot circuits induced by a quantum point contact*, *Phys. Rev. Lett.* **100**, 176805 (2008).
- [9] W. Schottky, *Über spontane Stromschwankungen in verschiedenen Elektrizitätsleitern*, *Ann. Phys. (Leipzig)* **362**, 541 (1918).
- [10] M. Strass, P. Hänggi, and S. Kohler, *Nonadiabatic Electron Pumping: Maximal Current with Minimal Noise*, *Phys. Rev. Lett.* **95**, 130601 (2005).
- [11] Y. V. Nazarov and J. J. R. Struben, *Universal excess noise in resonant tunneling via strongly localized states*, *Phys. Rev. B* **53**, 15466 (1996).
- [12] B. Elattari and S. A. Gurvitz, *Shot noise in coupled dots and the "fractional charges"*, *Phys. Lett. A* **292**, 289 (2002).

## Bibliography

- [13] R. J. Glauber, *Quantum Theory Of Optical Coherence*, Physical Review **130**, 2529 (1963).
- [14] G. B. Lesovik and L. S. Levitov, *Noise in an ac biased junction: Nonstationary Aharonov-Bohm effect*, Phys. Rev. Lett. **72**, 538 (1994).
- [15] C. Emary, D. Marcos, R. Aguado, and T. Brandes, *Frequency-dependent counting statistics in interacting nanoscale conductors*, Phys. Rev. B **76**, 161404 (2007).
- [16] T. Brandes, *Waiting times and noise in single particle transport*, Ann. Phys. (Leipzig) **17**, 477 (2008).
- [17] D. A. Bagrets and Y. V. Nazarov, *Full counting statistics of charge transfer in Coulomb blockade systems*, Phys. Rev. B **67**, 085316 (2003).
- [18] D. A. Bagrets, Y. Utsumi, D. S. Golubev, and G. Schoen, *Full counting statistics of interacting electrons*, Fortschritte der Physik-Progress of Physics **54**, 917 (2006).
- [19] C. Kreuter, S. Bächle, E. Scheer, and A. Erbe, *Electrical characterization of alkane monolayers using micro-transfer printing: tunneling and molecular transport*, New J. Phys. **10**, 075001 (2008).
- [20] K.-D. Hof, C. Rössler, W. Wegscheider, S. Ludwig, and A. W. Holleitner, *Optically induced charge transport through submicron channels*, Physica E **40**, 1739 (2008).
- [21] K.-D. Hof, C. Rössler, S. Manus, J. P. Kotthaus, A. W. Holleitner, D. Schuh, and W. Wegscheider, *Dynamic photoconductive gain effect in shallow-etched AlGaAs/GaAs quantum wires*, Phys. Rev. B **78**, 115325 (2008).
- [22] C. Rössler *et al.*, *Optically induced transport properties of freely suspended semiconductor submicron channels*, Appl. Phys. Lett. **93**, 071107 (2008).
- [23] K.-D. Hof, *private communication*.
- [24] S. Camalet, S. Kohler, and P. Hänggi, *Shot-noise control in ac-driven nanoscale conductors*, Phys. Rev. B **70**, 155326 (2004).
- [25] U. Fano, *Ionization Yield of Radiations. II. The Fluctuations of the Number of Ions*, Phys. Rev. **72**, 26 (1947).
- [26] Ya. M. Blanter and M. Büttiker, *Shot noise in mesoscopic conductors*, Phys. Rep. **336**, 1 (2000).
- [27] H. Grabert and G.-L. Ingold, *Identification of Coulomb blockade and macroscopic quantum tunneling by noise*, Europhys. Lett. **58**, 429 (2002).
- [28] H. Risken, *The Fokker-Planck Equation*, Vol. 18 of *Springer Series in Synergetics*, 2nd ed. (Springer, Berlin, 1989).

- [29] B. Reulet, J. Senzier, and D. E. Prober, *Environmental Effects in the Third Moment of Voltage Fluctuations in a Tunnel Junction*, Phys. Rev. Lett. **91**, 196601 (2003).
- [30] J. Ankerhold and H. Grabert, *How to detect the fourth-order cumulant of electrical noise*, Phys. Rev. Lett. **95**, 186601 (2005).
- [31] R. Landauer, *Spatial Variation of Currents and Fields Due to Localized Scatterers in Metallic Conduction*, IBM J. Res. Dev. **1**, 223 (1957).
- [32] Y. Imry and R. Landauer, *Conductance viewed as transmission*, Rev. Mod. Phys. **71**, S306 (1999).
- [33] S. Datta, *Electronic Transport in Mesoscopic Systems* (Cambridge University Press, Cambridge, 1995).
- [34] Y.-C. Chen and M. Di Ventra, *Shot noise in nanoscale conductors from first principles*, Phys. Rev. B **67**, 153304 (2003).
- [35] M. Wagner, *Photon-assisted transmission through an oscillating quantum well: A transfer-matrix approach to coherent destruction of tunneling*, Phys. Rev. A **51**, 798 (1995).
- [36] W. Li and L. E. Reichl, *Floquet scattering through a time-periodic potential*, Phys. Rev. B **60**, 15732 (1999).
- [37] M. Henseler, T. Dittrich, and K. Richter, *Signatures of chaos and tunneling in AC-driven quantum scattering*, Europhys. Lett. **49**, 289 (2000).
- [38] S. A. Gurvitz and Ya. S. Prager, *Microscopic derivation of rate equations for quantum transport*, Phys. Rev. B **53**, 15932 (1996).
- [39] T. H. Stoof and Yu. V. Nazarov, *Time-dependent resonant tunneling via two discrete states*, Phys. Rev. B **53**, 1050 (1996).
- [40] P. Brune, C. Bruder, and H. Schoeller, *Photon-assisted transport through ultrasmall quantum dots: Influence of intradot transitions*, Phys. Rev. B **56**, 4730 (1997).
- [41] E. G. Petrov and P. Hänggi, *Nonlinear Electron Current through a Short Molecular Wire*, Phys. Rev. Lett. **86**, 2862 (2001).
- [42] E. G. Petrov, V. May, and P. Hänggi, *Controlling electron transfer processes through short molecular wires*, Chem. Phys. **281**, 211 (2002).
- [43] J. Lehmann, G.-L. Ingold, and P. Hänggi, *Incoherent charge transport through molecular wires: interplay of Coulomb interaction and wire population*, Chem. Phys. **281**, 199 (2002).

## Bibliography

- [44] J. Lehmann, S. Kohler, V. May, and P. Hänggi, *Vibational effects in laser-driven molecular wires*, J. Chem. Phys. **121**, 2278 (2004).
- [45] S. Kohler, J. Lehmann, and P. Hänggi, *Driven transport on the nanoscale*, Phys. Rep. **406**, 379 (2005).
- [46] G. Kießlich, A. Wacker, and E. Schöll, *Shot noise of coupled semiconductor quantum dots*, Phys. Rev. B **68**, 125320 (2003).
- [47] T. Novotný, A. Donarini, C. Flindt, and A.-P. Jauho, *Shot Noise of a Quantum Shuttle*, Phys. Rev. Lett. **92**, 248302 (2004).
- [48] C. Flindt, T. Novotný, and A.-P. Jauho, *Current noise in a vibrating quantum dot array*, Phys. Rev. B **70**, 205334 (2004).
- [49] W. Belzig, *Full counting statistics of super-Poissonian shot noise in multilevel quantum dots*, Phys. Rev. B **71**, 161301(R) (2005).
- [50] J. Koch, M. E. Raikh, and F. von Oppen, *Full counting statistics of strongly non-ohmic transport through single molecules*, Phys. Rev. Lett. **95**, 056801 (2005).
- [51] J. Aghassi, A. Thielmann, M. H. Hettler, and G. Schön, *Shot noise in transport through two coherent strongly coupled quantum dots*, Phys. Rev. B **73**, 195323 (2006).
- [52] S. Nakajima, *On Quantum Theory of Transport Phenomena*, Prog. Theor. Phys. **20**, 948 (1958).
- [53] R. Zwanzig, *Ensemble methods in the theory of irreversibility*, J. Chem. Phys. **33**, 1338 (1960).
- [54] H. P. Breuer and F. Petruccione, *The theory of open quantum systems* (Oxford University Press, Oxford, 2002).
- [55] A. J. van Wonderen and K. Lendi, *Quantum-Theory of Dissipative Processes - The Markov Approximation revisited*, J. Stat. Phys. **80**, 273 (1995).
- [56] F. J. Kaiser and S. Kohler, *Shot noise in non-adiabatically driven nanoscale conductors*, Ann. Phys. (Leipzig) **16**, 702 (2007).
- [57] F. J. Kaiser, P. Hänggi, and S. Kohler, *Coulomb repulsion effects in driven electron transport*, Eur. Phys. J. B **54**, 201 (2006).
- [58] T. Novotný, *Investigation of apparent violation of the second law of thermodynamics in quantum transport studies*, Europhys. Lett. **59**, 648 (2002).
- [59] L. P. Kouwenhoven, A. T. Johnson, N. C. van der Vaart, C. J. P. M. Harmans, and C. T. Foxon, *Quantized current in a quantum-dot turnstile using oscillating tunnel barriers*, Phys. Rev. Lett. **67**, 1626 (1991).

- [60] H. Pothier, P. Lafarge, C. Urbina, D. Esteve, and M. H. Devoret, *Single-electron pump based on charging effects*, *Europhys. Lett.* **17**, 249 (1992).
- [61] C. A. Stafford and N. S. Wingreen, *Resonant Photon-Assisted Tunneling through a Double Quantum Dot: An Electron Pump from Spatial Rabi Oscillations*, *Phys. Rev. Lett.* **76**, 1916 (1996).
- [62] M. Switkes, C. M. Marcus, K. Campman, and A. C. Gossard, *An Adiabatic Quantum Electron Pump*, *Science* **283**, 1905 (1999).
- [63] M. Wagner and F. Sols, *Subsea Electron Transport: Pumping Deep within the Fermi Sea*, *Phys. Rev. Lett.* **83**, 4377 (1999).
- [64] B. L. Hazelzet, M. R. Wegewijs, T. H. Stoof, and Yu. V. Nazarov, *Coherent and incoherent pumping of electrons in double quantum dots*, *Phys. Rev. B* **63**, 165313 (2001).
- [65] J. Lehmann, S. Kohler, P. Hänggi, and A. Nitzan, *Molecular Wires Acting as Coherent Quantum Ratchets*, *Phys. Rev. Lett.* **88**, 228305 (2002).
- [66] L. Arrachea, *dc response of a dissipative driven mesoscopic ring*, *Phys. Rev. B* **70**, 155407 (2004).
- [67] P. W. Brouwer, *Scattering approach to parametric pumping*, *Phys. Rev. B* **58**, R10135 (1998).
- [68] M. Strass, S. Kohler, J. Lehmann, and P. Hänggi, *Transport through a driven three-site system*, *Mol. Cryst. Liq. Cryst.* **426**, 59 (2005).
- [69] F. J. Kaiser, M. Strass, S. Kohler, and P. Hänggi, *Coherent charge transport through molecular wires: influence of strong Coulomb repulsion*, *Chem. Phys.* **322**, 193 (2006).
- [70] P. W. Anderson, *Absence of Diffusion in Certain Random Lattices*, *Phys. Rev.* **109**, 1492 (1958).
- [71] S. Zimmermann, A. Wixforth, J. P. Kotthaus, W. Wegscheider, and M. Bichler, *A semiconductor-based photonic memory cell*, *Science* **283**, 1292 (1999).
- [72] T. A. Franke and A. Wixforth, *Microfluidics for Miniaturized Laboratories on a Chip*, *ChemPhysChem* **9**, 2140 (2008).
- [73] B. Kästner, V. Kashcheyevs, G. Hein, K. Pierz, U. Siegner, and H. W. Schumacher, *Robust single-parameter quantized charge pumping*, *Appl. Phys. Lett.* **92**, 192106 (2008).
- [74] J. Ebbecke, S. Maisch, A. Wixforth, R. Calarco, R. Meijers, M. Marso, and H. Lueth, *Acoustic charge transport in GaN nanowires*, *Nanotechnology* **19**, 275708 (2008).

## Bibliography

- [75] M. R. Buitelaar *et al.*, *Adiabatic charge pumping in carbon nanotube quantum dots*, Phys. Rev. Lett. **101**, 126803 (2008).
- [76] B. Kästner *et al.*, *Single-parameter nonadiabatic quantized charge pumping*, Phys. Rev. B **77**, 153301 (2008).
- [77] F. J. Kaiser, S. Kohler, P. Hänggi, M. Malecha, J. Ebbecke, A. Wixforth, A. D. Wieck, and D. Reuter, *Theoretical and experimental investigations of coulomb blockade in coupled quantum dot systems*, J. Phys.: Condens. Matter **20**, 374108 (2008).
- [78] S. Ludwig, *private communication*.
- [79] F. Grossmann, T. Dittrich, P. Jung, and P. Hänggi, *Coherent Destruction of Tunneling*, Phys. Rev. Lett. **67**, 516 (1991).
- [80] J. Ebbecke, *private communication*.
- [81] Q. Hu, *Photon-Assisted Quantum Transport In Quantum Point Contacts*, Appl. Phys. Lett. **62**, 837 (1993).
- [82] G. Platero and R. Aguado, *Photon-assisted transport in semiconductor nanostructures*, Phys. Rep. **395**, 1 (2004).
- [83] H. Kosaka, D. Rao, H. Robinson, P. Bandaru, T. Sakamoto, and E. Yablonovitch, *Photoconductance quantization in a single-photon detector*, Phys. Rev. B **65**, 201307 (2002).
- [84] R. Wyss, C. C. Eugster, J. A. del Alamo, and Q. Hu, *Far-Infrared Photon-Induced Current in a Quantum Point-Contact*, Appl. Phys. Lett. **63**, 1522 (1993).
- [85] B. J. van Wees, H. van Houten, C. W. J. Beenakker, J. G. Williamson, L. P. Kouwenhoven, D. van der Marel, and C. T. Foxon, *Quantized conductance of point contacts in a two-dimensional electron gas*, Phys. Rev. Lett. **60**, 848 (1988).
- [86] C. Beenakker and H. van Houten, *Quantum transport in semiconductor nanostructures*, Sol. Stat. Phys. **44**, 1 (1991).
- [87] H. Linke, L. Christensson, P. Omling, and P. E. Lindelof, *Stability of classical electron orbits in triangular electron billiards*, Phys. Rev. B **56**, 1440 (1997).
- [88] L. Christensson, H. Linke, P. Omling, P. E. Lindelof, I. V. Zozoulenko, and K.-F. Berggren, *Classical and quantum dynamics of electrons in open equilateral triangular billiards*, Phys. Rev. B **57**, 12306 (1998).
- [89] R. A. Jalabert, H. U. Baranger, and A. D. Stone, *Conductance fluctuations in the ballistic regime: A probe of quantum chaos?*, Phys. Rev. Lett. **65**, 2442 (1990).

- [90] C. M. Marcus, A. J. Rimberg, R. M. Westervelt, P. F. Hopkins, and A. C. Gosard, *Conductance fluctuations and chaotic scattering in ballistic microstructures*, Phys. Rev. Lett. **69**, 506 (1992).
- [91] C. Flindt, C. Fricke, F. Hohls, T. Novotný, K. Netočný, T. Brandes, and R. J. Haug, *Universal oscillations in counting statistics*, arXiv:0901:0832.
- [92] G. Floquet, *Sur les équations différentielles linéaires à coefficients périodiques*, Ann. de l'Ecole Norm. Sup. **12**, 47 (1883).
- [93] S. Kohler, M. Strass, P. Hänggi, M. Rey, and F. Sols, *Current and noise suppression in ac-driven coherent transport*, in *18th International Conference on Noise and Fluctuations* (AIP, New York, 2005), Vol. 780, p. 45, invited contribution.
- [94] J. H. Shirley, *Solution of the Schrödinger Equation with a Hamiltonian Periodic in Time*, Phys. Rev. **138**, B979 (1965).
- [95] A. Wacker, *Semiconductor superlattices: a model system for nonlinear transport*, Phys. Rep. **357**, 1 (2002).
- [96] J. Lehmann, S. Kohler, P. Hänggi, and A. Nitzan, *Rectification of laser-induced electronic transport through molecules*, J. Chem. Phys. **118**, 3283 (2003).
- [97] M. Grifoni and P. Hänggi, *Driven Quantum Tunneling*, Phys. Rep. **304**, 229 (1998).
- [98] J. Davies, *The physics of low-dimensional semiconductors: an introduction*, 3rd ed. (Cambridge University Press, Cambridge, 1998).
- [99] A. Fowler, A. Hartstein, and R. Webb, *Conductance in Restricted-Dimensionality Accumulation Layers*, Phys. Rev. Lett. **48**, 196 (1982).
- [100] M. Pepper, *Magnetic localization in silicon inversion layers*, Philos. Mag **37B**, 83 (1978).
- [101] H. van Houten, C. Beenakker, and A. Staring, in *Single-Electron Tunneling and Mesoscopic Devices*, Vol. 31 of *Springer Series in Electronics and Photonics*, edited by H. Koch and H. Lübbig (Springer, Berlin, 1992), pp. 159–170.
- [102] C. Livermore, C. H. Crouch, R. M. Westervelt, K. L. Campman, and A. C. Gossard, *The Coulomb Blockade in Coupled Quantum Dots*, Science **274**, 1332 (1996).
- [103] M. Ciorga, A. S. Sachrajda, P. Hawrylak, C. Gould, P. Zawadzki, S. Jullian, Y. Feng, and Z. Wasilewski, *Addition spectrum of a lateral dot from Coulomb and spin-blockade spectroscopy*, Phys. Rev. B **61**, R16315 (2000).
- [104] L. P. Kouwenhoven, *Coupled Quantum Dots as Artificial Molecules*, Science **268**, 1440 (1995).

## Bibliography

- [105] J. Weis, in *Fundamentals of Nanoelectronics – Lecture Manuscripts of the 34th Spring School of the Department of Solid State Research*, Vol. 14 of *Matter and Materials*, edited by S. Blügel, M. Luysberg, K. Urban, and R. Waser (Forschungszentrum Jülich GmbH, Jülich, 2003), Chap. D6, pp. D6.1–D6.33.
- [106] J. Nicholls, J. Frost, D. Ritchie, M. Grimshaw, and G. Jones, *Charging effects and the excitation of quantum dot formed by an impurity potential*, *Phys. Rev. B* **48**, 8866 (1993).



# Acknowledgement

First, I would like to thank *Prof. Peter Hänggi* for giving me the opportunity to join his group and work on such a highly interesting field like quantum transport. His dedicated and elucidating manner of doing physics, the inspiring discussion and his constant support have always been stimulating and encouraging for me.

I am deeply obliged to *Sigmund Kohler* for supervising this thesis. The chance to work nearly independent and at the same time having guidance whenever needed was a great experience. I greatly enjoyed his clear way of explaining physics and the uncomplicated collaboration during my thesis.

Many thanks to *Prof. Alexander Holleitner* for being an excellent co-advisor of this thesis.

I would also like to thank *Prof. Ulrich Eckern* for acting as a referee of my thesis and *Prof. Achim Wixforth* for being head of my doctoral commission.

My special thanks go to our experimental partners in Augsburg, *Prof. Achim Wixforth*, *Jens Ebbecke*, and *Marcin Malecha*, for the insights into their experiments, the fruitful discussions and our great common paper.

My special thanks go also to our experimental partners in Munich, *Prof. Alexander Holleitner* and *Klaus-Dieter Hof*, for the invitation to backup their great results on photo induced ballistic transport with a theoretical model.

*Sigmund Kohler*, *Michael Strass* and *Jörg Lehmann* provided the numerical code for the computation of the non-interacting case and the Floquet routines.

I am indebted to *Prof. Gert-Ludwig Ingold*, *Stefan Schenk*, *Ralf Utermann* and *Roland Doll* for their help on software as well as hardware issues.

Moreover, I also have to thank *Stefan Schenk* for great and comprehensive discussions about physics which gave always new insights and *Christoph Kreisbeck* for his help during the derivation of the Full Counting Statistics for the master equation.

The members of the groups *Theoretische Physik I* and *Theoretische Physik II*—present and former ones—provided a stimulating, encouraging and pleasant atmosphere.

For the careful proof-reading of my thesis and stimulating comments I owe thanks to *Eva Regnier*, *Michael Merkl*, *Georg Reuther*, and many more; their help made the manuscript much more readable.

*The Elitenetwork of Bavaria* via the *International Doctorate Program "NanoBioTechnology"* is gratefully acknowledged for supporting my thesis with a scholarship. Furthermore, I acknowledge funding by the *Deutsche Forschungsgemeinschaft* via the Priority Program SPP1243, by the *Nanosystems Initiative Munich (NIM)*, and by the *Spain-Germany Programme of Acciones Integradas (DAAD and MEC)*.

Zuletzt möchte ich ganz besonders meinen Eltern danken, ohne die ich es sicher nicht geschafft hätte, mein Studium und die Promotion mit Erfolg abzuschliessen.

## *Bibliography*

# Lebenslauf

## Zur Person

Franz Kaiser

\* 2. Oktober 1980 in München

## Ausbildung

Seit 04/2006

**Wissenschaftlicher Angestellter**  
Universität Augsburg

10/2000 – 12/2005

**Studium der Physik**  
Universität Augsburg

09/2002 – 08/2003

**Auslandsstudium**  
Università degli Studi dell'Insubria, Como, Italien

10/1991 – 06/2000

**Gisela-Gymnasium München**  
Abschluss mit Abitur